EVALUATION OF VARIOUS TRACER CANDIDATES FOR MOLECULAR IMAGING OF OSTEOMYELITIS AND A JUVENILE PORCINE MODEL OF HEMATOGENEOUS *STAPHYLOCOCCUS AUREUS* OSTEOMYELITIS

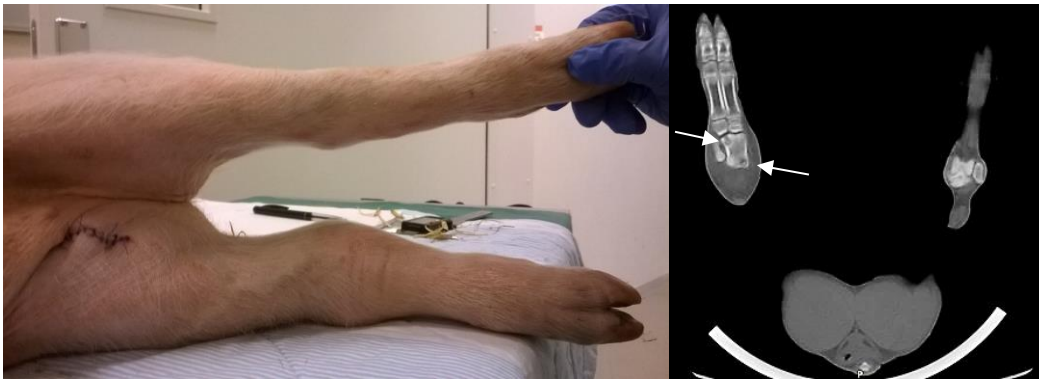

By Pia Afzelius, chief doctor, M.D., Ph.D.

Specialist in internal medicine

Specialist in clinical physiology and molecular imaging

PUBLICATIONS INCLUDED in the DOCTORAL THESIS.

The thesis is based on the following peer-reviewed publications, referred to in the text by the associated Roman numerals.

I. Nielsen OL, **Afzelius P**, Bender D, Schønheyder HC, Leifsson PS, Nielsen KM, Larsen JO, Jensen SB, Alstrup AK. Comparison of autologous ^{111}In-leukocytes, ^{18}F-FDG, ^{11}C-methionine, ^{11}C-PK11195, and ^{68}Ga-citrate for diagnostic nuclear imaging in a juvenile porcine haematogenous *Staphylococcus aureus* osteomyelitis model. Am J Nucl Med Mol Imaging 2015; 5: 169-82.

II. Afzelius P, Nielsen OL, Alstrup AKO, Bender D, Leifsson PS, Jensen SB, Schønheyder HC. Biodistribution of the radionuclides ^{18}F-FDG, ^{11}C-methionine, ^{11}C-PK11195, and ^{68}Ga-citrate in domestic juvenile female pigs and morphological and molecular imaging of the tracers in hematogenously disseminated *Staphylococcus aureus* lesions. Am J Nucl Med Mol Imaging 2016; 6(1): 42-58.

III. Afzelius P, Alstrup AKO, Schønheyder HC, Borghammer P, Jensen SB, Bender D, Nielsen OL. Utility of ^{11}C-methionine and ^{11}C-donepezil for imaging Staphylococcus aureus-induced osteomyelitis in a juvenile porcine model: comparison to autologous ^{111}In-labelled leukocytes, ^{99m}Tc-DPD, and ^{18}F-FDG. Am J Nucl Med Mol Imaging 2016; 6(6): 286-300.

IV. Afzelius P, Nielsen OL, Jensen SB, Alstrup AKO. Post Mortem Leukocyte Scintigraphy in Juvenile Pigs with Experimentally Induced Osteomyelitis. Contrast Media Mol Imaging 2017; 11: 1-6.

V. Afzelius P, Nielsen OL, Schønheyder HC, Alstrup AKO, Hansen SB. An untapped potential for imaging peripheral osteomyelitis in paediatrics using [18F]FDG PET/CT is the inference from a juvenile porcine model. EJNMMI Res. 2019; 9(1): 29-37.

VI. Afzelius P, Heegaard PMH, Jensen SB, Alstrup AKO, Schønheyder HC, Eek A, Boerman O, Nielsen OL. [^{99m}Tc]-labelled interleukin-8 as a diagnostic tool compared to [^{18}F]FDG and CT in an experimental porcine osteomyelitis model. Am J Nucl Med Mol Imaging 2020; 10(1): 32-46.

VII. Afzelius P, Alstrup AKO, Nielsen OL, Nielsen KM, Jensen SB. Attempts to Target *Staphylococcus aureus* Induced Osteomyelitis Bone Lesions in a Juvenile Pig Model by Using Radiotracers. Molecules 2020; 25(18): 4329-43.

VIII. Alstrup AKO, Jensen SB, Nielsen OL, Jødal L, **Afzelius P.** Preclinical Testing of Radiopharmaceuticals for the Detection and Characterization of Osteomyelitis: Experiences from a Porcine Model. Molecules. 2021; 26(14): 4221-32.

IX. Afzelius P, Morsing MK, Nielsen OL, Alstrup AKO, Jensen SB, Jødal L. Lymph Nodes Draining Infections Investigated by PET and Immunohistochemistry in a Juvenile Porcine Model. Molecules 2022; 27(9): 2792-3006.

X. Alstrup AKO, Lillethorup TH, Landauer AM, **Afzelius P**. PET imaging sessions do not cause detectable organ pathology in Göttingen minipigs. Scand J Lab Animal Sci 2022. *Submitted.* Published Scand J Lab Animal Sci. 2024; 50(2); 6-12.

PREFACE AND ACKNOWLEDGMENTS

This thesis would not have been possible without the support and engagement of the members of the osteomyelitis group and the financial and mental support of Henrik Christian Berthelsen, Chief Doctor, Ph.D., Head of the Department of Clinical Physiology and Nuclear Medicine, Aalborg University Hospital, Lars Jelstrup Petersen, Chief Doctor, Professor, Dr. MSc., Department of Clinical Physiology and Nuclear Medicine, Aalborg University Hospital, and Henrik Carl Schønheyder, Chief Doctor, Professor, Dr. MSc., Department of Clinical Microbiology, Aalborg University Hospital, Aalborg, and Department of Clinical Medicine, Aalborg University, Aalborg. To these individuals, I am genuinely grateful.

There are so many people to whom I owe thanks, but here I would like to thank the members of the osteomyelitis group specifically. Working with you has been truly inspiring, challenging, conducive to learning, and fun:

Ole Lerberg Nielsen, Veterinarian, Associate Professor, Ph.D., Department of Veterinary and Animal Sciences, Faculty of Health and Medical Sciences, University of Copenhagen, 2000 Copenhagen F, Denmark;

Aage Kristian Olsen Alstrup, Veterinarian, Ph.D., Dr. Vet. Sci., Associate Professor, Department of Nuclear Medicine & PET, Aarhus University Hospital, Aarhus, Denmark, Department of Clinical Medicine, Aarhus University, Denmark;

Lars Jødal, Hospital Physicist, Ph.D., Department of Nuclear Medicine, Aalborg University Hospital, Denmark;

Svend Borup Jensen, Radiochemists, Ph.D., Associate Professor, Department of Nuclear Medicine, Aalborg University Hospital, Aalborg, Denmark, Department of Chemistry and Biosciences, Aalborg University, Aalborg, Denmark;

Henrik Carl Schønheyder, Chief Doctor, Professor, Dr. MSc., Department of Clinical Microbiology, Aalborg University Hospital, Aalborg, Department of Clinical Medicine, Aalborg University, Aalborg;

Søren Baarsgaard Hansen, Hospital Physicist, Ph.D., Department of Nuclear Medicine & PET, Aarhus University Hospital, Aarhus, Denmark.

I would also like to thank Dennis Brok, Betina Gjedsted Andersen, Elisabeth Wairimu Petersen, Malene Hylle, Hanne Thaagaard Larsen, Sanne Kjær Pilgaard, Rikke Skall, Janne Frederiksen, Lotte S. Meyer, Ole Sørensen, Jens Jespersgaard Sørensen, Torben Madsen, Lena Mortensen, Benedict Kjærgaard, Helle Danielsen, Mie Ringgaard Dollerup, Dorte Smith, Rikke Bertelsen, Karin M Nielsen, Dirk Bender, Peter MH Heegaard, Páll S. Leifsson, and the staff at Påskehøjgård, Aarhus for technical support.

Thanks also to Louise Kruse Jensen, Veterinarian, Associate Professor, Ph.D., Dr. Vet. Sci., Department of Veterinary and Animal Science, University of Copenhagen; John Mathews, Professor, Epidemiologist, Melbourne School of Population and Global Health, Australia; and The British

Medical Journal for sharing and allowing the presentation of your excellent and informative figures (Figures 2 and 6).

Finally, thanks to my family, especially my sons Esben, Kristian, and Johan, without whom none of this would have been meaningful. I apologize for what you have missed, as most of my scientific work and the work on this thesis has taken place in my spare time since I left Aalborg. I would also like to thank my friends for the support and encouragement they provided throughout the preparation of this thesis.

This work was supported by grant no. 0602-01911B (11-107077) from the Danish Council for Independent Research, Technology, and Production Sciences and approved by the Danish Animal Experimentation Board and by the Danish Occupational Health Surveillance.

ABBREVIATIONS

Bq: Becquerel
C: carbon
Ci: Curie
CT: computer tomografi/computed tomography
DDP: dicarboxypropane diphosphonate
DOTA: 1,4,7,10-tetraazacyclododecane-1,4,7,10-tetraacetic acid
FDG: fluoro-2-deoxy-D-glucose
F: fluor
Ga: gallium
Gy: Gray
HDP: hydroxy diphosphonate
H: hydrogen
IHC: immunohistochemistry
In: indium
IL: interleukin
MDP: methylene diphosphonate
MIP: maximum intensity projection
MRI: magnetisk resonans skanning/magnetic resonance imaging
Na: sodium
NOTA: 1,4,7-triazacyclononane-triacetic acid
OM: osteomyelitis
O: oxygen
PBR: peripheral benzodiazepine receptor
PET: positronemissionstomografi/positron emission tomography
PK11195: 1-[2-chlorophenyl]-*N*-[1-methyl-propyl]-3-iso-quinoline carboxamide
RANKL: Receptor activator of core-factor kappa-B ligand
S. aureus: *Staphylococcus aureus*
Siglec-9: sialic acid-binding immunoglobulin-like lectin 9
SPECT: single photon emission tomography
Sv: Sievert
Sulfur: S
SUVmax: the maximum standardized uptake value
Tc: technetium
TCM: tissue compartment model
TSPO: translocator protein
UBI: ubiquicidin
US: ultrasound
VAP-1: vascular adhesion protein 1
VOI: volumes of interest
WBC: white blood cell

TABLE OF CONTENTS

RESUMÉ PÅ DANSK (DANISH SUMMARY)

Osteomyelitis (OM) er en infektion i knoglemarven og i de tilstødende knoglestrukturer, ofte forårsaget af den gram-positive bakterie *Staphylococcus aureus* (*S. aureus*). OM resulterer i tiltagende knogledestruktion og -tab og strækker sig ofte ind i omgivende bindevæv. Derfor er tidlig påvisning og lokalisering af OM afgørende for et rettidigt og passende valg af antibiotikabehandling for at forhindre knoglenekrose.

Skelnen mellem aktive bakterielle infektioner og sterile inflammationer er imidlertid vanskelig med de tilgængelige billeddannende modaliteter. Modaliteterne visualiserer enten morfologiske forandringer (konventionelle røntgenbilleder, computer tomografi (CT) og magnetic resonans imaging), *de novo* syntese ([^{67}Ga]Ga-citrat positron emissions tomografi (PET)), rekruttering af immunceller (^{99m}Tc/^{111}In-mærket leukocyt-helkropsskintigrafi) eller øget glukosemetabolisme i inflammatoriske celler (2-[^{18}F]fluoro-2-deoxy-D-glucose (2-[^{18}F]FDG) PET). Konventionel radiologisk billeddannelse kan ofte bekræfte og vise omfanget af OM og dermed inddrages i planlægning af behandlingen eller udelukke diagnosen, men den er imidlertid ikke altid tilstrækkelig og suppleres derfor ofte med nuklearmedicinsk billeddiagnostik. De aktuelt hyppigst anvendte sporstoffer har høj sensitivitet, men ikke så høj specificitet.
Derfor undersøgte og udviklede vi forskellige nye sporstoffer med potentiale for påvisning af OM ud fra andre strategier, rettet mod infektionen *per se* (mærkede den af bakterier producerede biofilm *in vivo* under pågående OM, mærkede antimikrobielle peptider og specifikke enzymligander), idet vi håbede at kunne skelne mellem infektion og inflammation (**artikel I-III; artikel V-VII;** Jødal *et al*., 2014, 2016, 2017a, 2017b, 2018, 2019 og 2021).

Vor protokol blev udfærdiget i årene 2010-2012, selve etableringen af OM læsioner og skanningsarbejdet gik i gang i 2013 og blev afsluttet i 2017. De forskellige nye sporstoffer til påvisning af OM blev sammenlignet med de mere traditionelt anvendte sporstoffer (Jødal *et al.*, 2021). Hertil var det vigtigt med en god dyremodel. Vi evaluerede derfor også en juvenil grisemodel til hæmatogen *S. aureus* OM og fokuserede på OM hos børn (Alstrup *et al.*, 2016, 2020b; **artikel I-III; artikel V-VIII; artikel X**).

Vi fandt, at flere af sporstofferne var valide kandidater til molekylær billeddannelse af OM pga. af lav ioniserende stråling med acceptabel sensitivitet.

2-[^{18}F]FDG PET/CT spiller en stigende rolle i diagnostik og vurdering af behandlingsrespons ved sygdomme af både infektiøs og inflammatorisk oprindelse. PET kan ofte bidrage med betydningsfuld information på molekylært plan og følgelig vise sygdomsaktiviteten ved dens tidligste manifestationer. 2-[^{18}F]FDG PET/CT har vist sig at være en robust og præcis modalitet til diagnostik og kvantificering af sygdomsbyrden, især hvad angår den kliniske diagnose og behandlingsmonitorering. 2-[^{18}F]FDG PET er rekommanderet til påvisning af infektioner i vertebrae og spondylodiscitis men ikke til påvisning af OM i perifere knogler. Her er leukocytskintigrafi rekommanderet.

Vi fandt imidlertid, at både 2-[^{18}F]FDG og CT lokaliserede alle og endda meget små (0,01 cm^3) OM-læsioner i perifere knogler (**artikel I-VII**). Det var muligt at reducere den injicerede aktivitet 2-[^{18}F]FDG betydeligt uden at gå på kompromis med billedkvaliteten (**artikel V**). Resultatet indikerer, at 2-[^{18}F]FDG PET/CT kan anvendes ved perifer OM hos børn.

Vi fandt to lovende sporstoffer; det radioaktivt mærkede proinflammatoriske kemotaktiske kemokin [^{99m}Tc]Tc-IL-8 (**artikel VI**) og den naturligt forekommende essentielle aminosyre methionin mærket med den positron-emitterende isotop ^{11}C, L-[*S*-methyl-^{11}C]methionin (**artikel I-III; artikel IX**). [^{99m}Tc]Tc-IL-8 detekterede 70% af OM-læsionerne (**artikel VI**) svarende til de 79%, vi fandt for [^{111}In]-mærket autologe leukocytter (**artikel III; artikel IV**). [^{99m}Tc]Tc-IL-8 var endnu bedre, når tiden fra injektion til skanningen blev udskudt (92%) 139-150 min versus 239-

341 min. Den hurtige og nemme forberedelse, den tidlige og gode billedkvalitet samt den lavere strålingsbelastning tyder på, at [^{99m}Tc]Tc-IL-8 kan være et godt billeddannende alternativ til skintigrafi af akut OM hos børn.

Også L-[*S*-methyl-^{11}C]methionin påviste OM på samme niveau som [^{111}In]-mærkede autologe leukocytter; ca. 79% (**artikel I-IV**). Sporstoffet klarede sig endnu bedre ved påvisning af lymfeknuder, der drænerede *S. aureus*-inficerede foci: Sammenlignet med kontrol lymfeknuder akkumulerede inficerede lymfeknuder mere 2-[^{18}F]FDG (50%) og L-[*S*-methyl-^{11}C]methionin (100%) (**artikel III**). I et senere studium (**artikel IX**) viste det sig imidlertid, at det kun var lymfeknuder i knæhasen, der akkumulerede L-[*S*-methyl-^{11}C]methionin.

Den ideelle billedmodalitet eksisterer næppe, og afhængigt af sygdommen kan sensitiviteten og specificiteten af forskellige diagnostiske teknikker variere i forhold til patofysiologien, hvorfor de billeddannende teknikker og sporstoffer vil udvise forskellig diagnostisk nøjagtighed. Diagnosen af infektiøse processer er således ofte afhængig af at kunne detektere anatomiske og strukturelle ændringer i de berørte væv, der igen afhænger af infektionens art. De forskellige billeddannelsesteknikker kan imidlertid integrere den diagnostiske information ved at kombinere anatomiske og funktionelle data for at beskrive og karakterisere stedet og omfanget af den undersøgte sygdomsaktivitet.

Det lykkedes os at raffinere en juvenil porcin model til afprøvning af radioaktive sporstoffer. Vore resultater og anvendeligheden af radionukleotiderne til molekylær billeddannelse bør stimulere en indsats for yderligere at udforske deres rolle i håndteringen af infektions- og inflammatoriske sygdomme hos mennesker.

ENGLISH SUMMARY

Osteomyelitis (OM) is an infection of the bone marrow and adjacent bone structures, often caused by the gram-positive bacterium Staphylococcus aureus (S. aureus). OM results in progressive bone destruction and loss and often extends into surrounding soft tissues. Early identification and localization of OM are critical for timely and appropriate treatment selection. Prompt antibiotic therapy may prevent necrosis of the affected bone.

However, distinguishing between active bacterial infection and sterile inflammation using the available imaging modalities is difficult. These modalities either make it possible to view morphological changes (conventional X-rays, computed tomography (CT), and magnetic resonance imaging) or measure *de novo* synthesis ([^{67}Ga]Ga-citrate positron emission tomography (PET)), recruitment of immune cells (^{99m}Tc/^{111}In-labeled leukocyte whole body scintigraphy) or increased glucose metabolism in inflammatory cells (2-[^{18}F]fluoro-2-deoxy-D-glucose (2-[^{18}F]FDG) PET). Conventional radiographic imaging helps confirm and reveal the extent of OM, thereby making it possible to plan treatment or exclude the diagnosis of OM. Radiography is not always sufficient and is often supplemented with nuclear medicine methods. The most commonly used radionuclide tracers provide high sensitivity but relatively low specificity.

Therefore, we examined and developed various new tracers for detecting OM based on a variety of strategies. These strategies aimed at the infection *per se* (labeling the biofilm produced by bacteria *in vivo* during ongoing OM and the use of labeled antimicrobial peptides and specific enzyme ligands), and we hoped that these methods would make it possible to distinguish between infection and inflammation (**Papers I-VII;** Jødal *et al*., 2014, 2016, 2017a, 2017b, 2018, 2019, and 2021).

We designed our protocol in 2010-12, began our work in 2013, and completed scanning in 2017. We explored and developed various new tracers for detecting OM in **Papers I-VII**, **IX**, and other publications and compared them with traditional tracers (Jødal *et al*., 2021). For this, it was essential to have a suitable animal model. We refined and evaluated a juvenile pig model for hematogenous *S. aureus* OM and focused on OM in children (**Papers I-III; Papers V-VIII; Paper X;** Alstrup *et al*., 2015, 2020b).

We found several of the tracers we explored were valid candidates for molecular imaging of OM in children due to their low ionizing radiation levels and acceptable sensitivity.

2-[^{18}F]FDG-PET/CT has an expanding role in the diagnosis and treatment monitoring of diseases of infectious or inflammatory origin. Many studies support the use of 2-[^{18}F]FDG-PET/CT in patients with systemic and regional conditions. Specifically, PET can provide vital information at the molecular level, consequently allowing disease activity detection at its earliest manifestation. 2-[^{18}F]FDG-PET/CT has proven to be a robust and accurate modality for diagnosing and quantifying disease burden, particularly in clinical diagnosis and treatment monitoring. 2-[^{18}F]FDG-PET is recommended for detecting infections in the vertebrae and spondylodiscitis but not for detecting OM in peripheral bones. In these cases, leukocyte scintigraphy is recommended.

However, we found that both the well-known glucose analog 2-[^{18}F]FDG and CT could be used to localize all and even tiny (0.01 cm^3) OM lesions in peripheral bones (**Papers I-VII**). It was possible to considerably reduce the amount of 2-[^{18}F]FDG activity injected without compromising image quality (**Paper V**). The results indicate the applicability of 2-[^{18}F]FDG-PET/CT in peripheral OM in children.

Two promising tracers were the radio-labeled proinflammatory chemotactic chemokine [^{99m}Tc]Tc-IL-8 (**Paper VI**) and the naturally occurring essential amino acid methionine labeled with the positron-emitting isotope ^{11}C, L-[*S*-methyl-^{11}C]methionine **(Papers I-III; Paper IX**). [^{99m}Tc]Tc-IL-8 performed well, detecting 70% of the OM lesions (**Paper VI**), and its performance was even better when scanning was delayed (92%) 139-150 min versus 239-341 min, corresponding to the 79%

we found for [^{111}In]-labeled autologous leukocytes (**Papers III-IV**). The quick and easy preparation, early and good image quality, and lower radiation burden suggest that [^{99m}Tc]Tc-IL-8 may be a suitable imaging alternative for scintigraphic evaluation of OM in children.

Additionally, L-[*S*-methyl-^{11}C]methionine detected lesions with an efficiency of 79 %, comparable to that of [^{111}In]-labeled autologous leukocyte (**Papers I-III**). L-[*S*-methyl-^{11}C]methionine performed even better when used to detect lymph nodes draining *S. aureus*-infected foci: compared with control nodes, infected lymph nodes accumulated more L-[*S*-methyl-^{11}C]methionine (100%) and less 2-[^{18}F]FDG (50%) (**Paper III**). However, in a later and more extensive study (Paper IX), we found that only the popliteal lymph nodes accumulated L-[*S*-methyl-^{11}C]methionine.

Various imaging techniques and tracers have diverse diagnostic accuracies. An ideal imaging modality probably does not exist, and depending on the disease, the sensitivities and specificities of individual diagnostic techniques may vary according to the pathophysiology of the particular condition. Thus, infectious disease diagnosis often relies on detecting anatomical and structural changes in the affected tissues, depending on the nature of the infection. Nevertheless, imaging techniques can be used to integrate diagnostic information by combining anatomical and functional data to describe and characterize the site and extent of disease activity.

We succeeded in refining a juvenile porcine OM model so that it can be used to test radioactive tracers. Our results and the demonstrated utility of the radionuclides in molecular imaging should stimulate efforts to explore their role in managing infectious and inflammatory diseases in humans further.

INTRODUCTION:

Studies performed in animal models have shown that healthy bone tissue is generally resistant to infection and that direct trauma or a sizeable bacterial inoculum is usually required to establish a bone infection (Lew *et al*., 1997).

Infections of peripheral bone include osteitis and osteomyelitis. Osteitis, a superficial bacterial infection of the bone and surrounding soft tissue that occurs after trauma and/or surgery, is divided into two types: acute (occurring within the first eight weeks) and chronic (occurring at >8 weeks). Osteomyelitis refers to a primary infection of the bone marrow (usually endogenous and disseminated by hematogenous spread) with subsequent involvement of the cortical bone. The strategies used to diagnose bone infections are similar to those used to diagnose osteitis and OM. The terms "osteitis" and "osteomyelitis" are used interchangeably in the literature, and no clear distinction is made between them. We used the abbreviation OM for osteomyelitis.

The Waldvogel classification system (Waldvogel *et al*., 1970) describes three types of OMs: hematogenous OM, OM that has spread from adjacent tissue after trauma or surgery, especially from the area surrounding an implanted medical device, and OM that is secondary to vascular insufficiency (often occurring in the feet of diabetics). *Staphylococcus aureus* (*S. aureus*) is the leading cause of OM and is identified in 30 to 60% of cases (Lew *et al*., 2004; Calhoun *et al*., 2009; Conterno *et al*., 2013; Kremers *et al*., 2015; Garcia *et al*., 2018; Kavanagh *et al*., 2018).

Peripheral bone infections behave differently from infections of the axial skeleton, especially in the spine. Therefore, the diagnosis of infections in peripheral bones and axial bones differs. The etiology, behavior, and diagnosis of such infections also differ between children and adults. Hematogenous OM generally involves the epiphyses of the long bones in children and the axial skeleton in older adults (Espersen *et al*., 1991), partially because, in adults, the blood supply of vertebrae is better than that of long bones. Additionally, OM in children may be more acute than in adults. This thesis (**Papers I-IX**) will focus on the hematogenous *S. aureus* OM in juveniles.

Epidemiology and Diagnosis:

Despite advances in diagnostic and treatment modalities, bone and joint infections cause significant morbidity and disease burden worldwide. Chronic hematogenous OM in children was once a condition familiar to all orthopedic surgeons, but it is now rarely seen by surgeons practicing in developed countries. However, it remains a significant cause of morbidity and disability in children living in developing countries. In children, hematogenous OM is predominant, and the causative agent is most often *S. aureus* (Arnold *et al*., 2006; Jagodzinski *et al*., 2009; Peltola *et al*., 2014).

OM leads to morbidity and sometimes mortality in childhood, especially in parts of the world with low-income populations (Nickerson *et al*., 2009; Pääkkönen *et al*., 2012). In high-income countries, the incidence of OM is 13/100,000, including 8/100,000 acute and 5/100,000 subacute OM cases, with higher incidences of up to 200/100,000 reported in developing countries (Lauschke *et al.*, 1994; Museru *et al*., 2001; Onche *et al*., 2004; Ikpeme *et al.*, 2010; Jones *et al.*, 2011; Mantero *et al.*, 2011; Yeo *et al.*, 2014). Musculoskeletal impairment due to infection affects approximately 3% of children in low-income countries (Jones *et al*., 2011). OM is more frequent in some ethnic groups than others (Street *et al.*, 2015). Infections are more frequent in boys than in girls (in France, 24 and 19 cases of OM per 100,000 person-years occur in boys and girls, respectively) and among young children (Riise *et al.*, 2008; Grammatico-Guillon *et al.*, 2013).

Acute OM often occurs in children and is frequently found in long bones. Complications such as sequestrum formation and fistulous tract formation (**Figure 1**, **Paper V**) may lead to deformities of the affected bone (Nickerson *et al*., 2009; Pääkkönen *et al*., 2012).

Figure 1. The Appearance of Osteomyelitis Lesions on CT

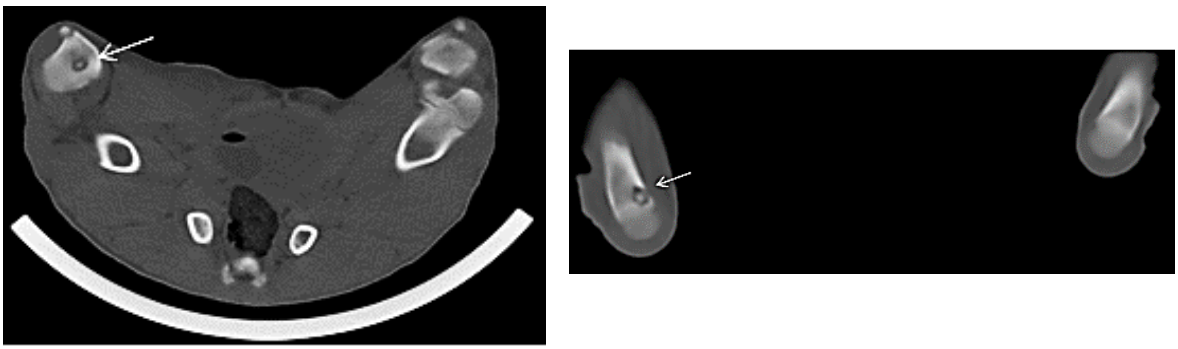

Figure 1. An OM lesion in pig 7 (**Table 3,** page 43) with sequestrum formation in the right proximal tibia indicated by an arrow (left image) and an OM lesion with both sequestrum and fistula formation in the right calcaneus bone indicated by an arrow (right image) (**Paper V**).

Early diagnosis of OM that makes the appropriate and timely therapy selection possible is required to avoid disabling complications. OM is difficult to treat with antibiotics and often requires surgical intervention to remove the infected tissue (debridement of infected necrotic bone and soft tissues), especially when antibiotic therapy has failed. Extensive reconstruction or amputation is sometimes the ultimate treatment (**Figure 2**). Effective pharmacological treatment of the various types of OMs is urgently needed to improve prognosis and quality of life and reduce costs.

Figure 2. Surgical Interventions in Osteomyelitis

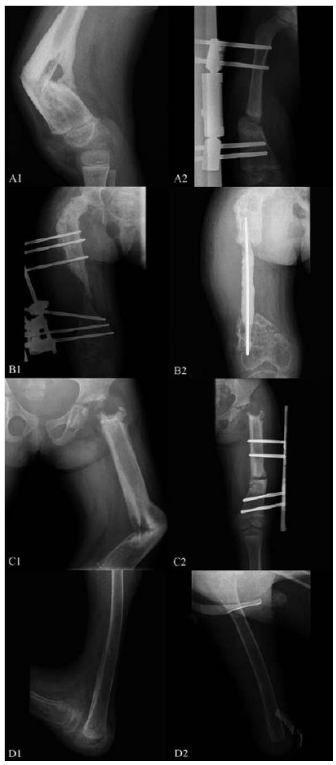

Figure 2. OM lesions in four Angolan children before and after surgical intervention. A: Case 1, OM of the right femur corrected by sequestrectomy and stabilized by an external fixator. B: Case 2, OM of the right femur leads to resection and the Pallacos spacer insertion. C: Case 3, Necrosis of the left femoral head and distal pseudoarthrosis corrected by resection of the caput femoris and distal femur realignment stabilized by an external fixator. D: Case 4, OM of the left femur and tibia treated by over-knee amputation and presented with the permission of Louise Kruse Jensen (Johansen *et al*., 2013).

Conventional Imaging Techniques

The gold standard method for diagnosis of OM, bone biopsy, with histopathological examination and culture of the causative bacteria, is invasive (**Figure 3, Paper III**). Discontinuation of the antibiotic regimen for two weeks before the collection of microbiological samples is recommended. In some cases, discontinuing the antibiotic regimen may not be possible due to the severity of the disease. Biopsies should be taken under image guidance to ensure that representative samples are obtained. Conventional X-ray and fluoroscopy easily permit visualization of bones. However, computed tomography (CT)-guided bone biopsies give higher contrast resolution and better visualization of the surrounding soft tissue, thus allowing better evaluation of the lesion's exact location and the position of the needle. Magnetic resonance imaging (MRI)-guided bone biopsy requires a special biopsy needle made of nonferromagnetic stainless steel. Noninvasive imaging is often preferred and is used when initiating empirical antimicrobial therapy. Unfortunately, all available diagnostic tools have limitations. No standard imaging method can detect OM with sufficiently high diagnostic accuracy. Clinical, laboratory, microbiological, and imaging tests are regularly performed based on personal experience, available techniques, expertise within the institute, and financial considerations.

Figure 3. Histopathology of Osteomyelitis

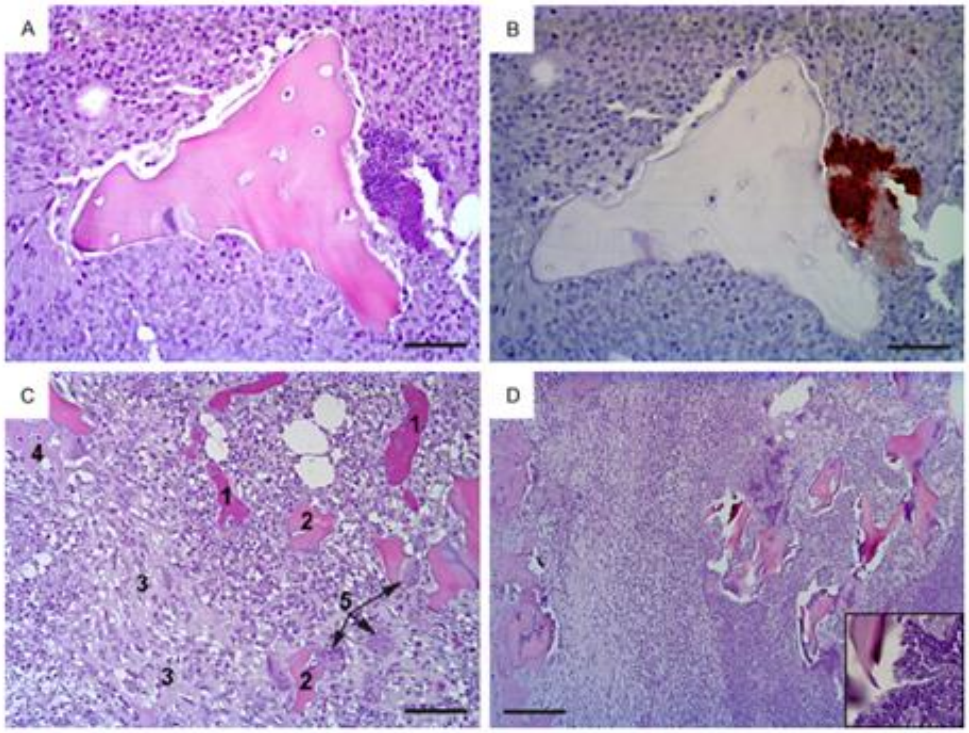

Figure 3. Histopathology of pig 6 (**Table 3** page 42) (frames A-D). Picture **A** shows the center of a bone lesion with necrotic trabecular bone surrounded by necrotic neutrophils (hematoxylin and eosin stain); on the right-hand side of the figure is a colony of bacteria (blue), that in **B** is identified as *S. aureus* (brown) by immunohistochemistry. **C** shows the periphery of the lesion, revealing blood vessels packed with erythrocytes (1), necrotic bone (2), fibroplasia (3), new bone formation (4), and osteoclasts (5) (hematoxylin and eosin stain). **D** presents a lesion that resembles subacute, suppurative, and necrotizing OM, bordering the cortex of the bone (left-hand side) (hematoxylin and eosin stain); the insert shows a close-up view of the bacteria seen in the necrotic center. Bars (**A** and **B**) = 25 μm, (**C**) = 50 μm, and (**D**) = 100 μm (**Paper III**).

In contrast, imaging is noninvasive. Noninvasive imaging is often preferred and is used when deciding whether to initiate empirical antimicrobial therapy. Techniques that yield morphological images, such as plain radiography, CT, MRI, and ultrasound (US), are often first-line imaging modalities. They help confirm or exclude the diagnosis of OM and reveal the extent of OM. Thus, they are also important in planning the treatment of OM. Radiographs are also essential for ruling out other diagnoses, including fractures and malignancies. These imaging methods are, however, not consistently successful in allowing the practitioner to identify the site of infection. For detecting bone disease, plain radiography is relatively insensitive; a lytic lesion, new periosteal bone formation covering an area at least 1 cm in diameter, and loss of at least 30-50% of the bone mineral mass are required for a lesion to be seen on a radiograph (Pineda *et al*., 2009). Thus, 40% of lesions are not detected by plain radiography (Salvo *et al*., 2009). Early findings may be subtle, and changes may not be evident until five to seven days in children and 2-3 weeks in adults (Peltola *et al*., 2014).

The sensitivity and specificity of conventional radiography for detecting acute OM range from 43 to 75% and 75 to 83%, respectively (David *et al*., 1987; Boutin *et al*., 1998). Up to 80% of patients will have a normal radiograph in the first two weeks after infection onset (Jaramillo, 2011).

Most pathological bone conditions, whether infectious, traumatic, neoplastic, or of other origins, are associated with increased vascularization and local remodeling of bone. Bone scintigraphy reveals the accompanying bone reaction as a focus of increased radioactive tracer uptake. [^{99m}Tc]technetium-diphosphonate bone scintigraphy is a sensitive (95%) technique; a 3-4% change in bone metabolism is sufficient to cause accumulation of this bone-seeking radiopharmaceutical, and bone scintigraphy, therefore, detects changes in bone days to weeks before osseous changes can be visualized by conventional radiography (Gold *et al*., 1991; Tuson *et al*., 1994; Kao *et al.*, 2003, Steer *et al*., 2004). The technique also provides an overview of the entire skeleton with relatively modest radiation exposure, but it is not specific (van den Wyngaert *et al*., 2016). Because bone scans are nonspecific, differential diagnosis of infection, tumor, and trauma is often impossible. A bone scan does not provide a definitive diagnosis but gives the location of the pathological process and helps reveal the presence of multiple OM lesions, for example, in neonates or when the diagnosis is unclear, as in cases of OM localized in the pelvis (McCarthy *et al*., 2005).

CT is the modality of choice for detecting bone sequestra, which mainly occur at later stages of OM (Gold *et al*., 1991). CT provides the highest image resolution for evaluating peripheral bone and is indicated for evaluating complex anatomic areas such as the shoulder and pelvis. CT can detect small foci of gas formation and cortical erosion and destruction areas. CT is not a routine examination in acute hematogenous OM, but it may be valuable in diagnosing chronic OM that may be mistaken for a tumor (McCarthy *et al*., 2005).

Currently, the imaging modality of choice is MRI. MRI detects early changes caused by OM within 2-5 days of disease onset. MRI can also reveal the presence of extraosseous manifestations and complications such as pyomyositis, joint effusion, and subperiosteal abscess and is valuable for planning surgery (Saavedra-Lozano *et al*., 2017). MRI has a significantly higher sensitivity (97-100%) and specificity (92%) than radiography or bone scintigraphy (Iliadis *et al.*, 2017; Saavedra-Lozano *et al*., 2017). MRI guidance is, therefore, appropriate for selected cases, such as pediatric cases (Averill *et al*., 2009; Fritz *et al*., 2012). However, MRI has limitations; these include higher cost, limited availability, long duration of scan time, and the need for sedation or anesthesia (Saavedra-Lozano *et al*., 2017).

Radioactive molecules make it possible to investigate physiological processes that occur in the body. They are routinely used in everyday clinical life to visualize a wide range of diseases using both positron emission tomography (PET) and scintigraphy with single photon emission tomography (SPECT). Since morphological imaging is not always sufficient, it is sometimes necessary to supplement it with nuclear medicine methods.

Molecular and cellular alterations occur earlier than structural changes during the pathological process. PET, which can detect changes at the pmol/l level, is highly sensitive to visualizing biological processes (James *et al*., 2012). The use of radiolabeled leukocytes, alone or combined with marrow imaging, provides high sensitivity and specificity greater than 90% for the diagnosis of skeletal infections (Kim *et al*., 2014; Govaert *et al*., 2017). There is still some concern about whether low-grade chronic diseases in which small amounts of bacteria are present within biofilms can lead to false-negative leukocyte scintigraphy results.

The well-known glucose-analog 2-[^{18}F]fluoro-2-deoxy-D-glucose (2-[^{18}F]FDG) has an expanding role in the diagnosis and treatment monitoring of diseases of infectious or inflammatory origin. Many studies support using 2-[18F]FDG-PET in evaluating systemic and regional conditions. Specifically, PET can provide vital information at a molecular level and consequently can detect disease activity at its earliest manifestation. 2-[^{18}F]FDG-PET has proven to be a robust and accurate modality for diagnosing and quantifying disease burden, particularly in clinical diagnosis and treatment monitoring. Love *et al*. reported that combined bone marrow and white blood cell (WBC) scintigraphy has significantly higher accuracy than 2-[^{18}F]FDG-PET in prosthetic infections,

independent of the interpretation criteria used for 2-[^{18}F]FDG-PET (Love *et al*., 2004). Vanquickenborne *et al*. reported similar sensitivities for WBC scintigraphy and 2-[^{18}F]FDG-PET (88%) but higher specificity for WBC scanning compared with FDG-PET (100% versus 78%) (Vanquikenborne *et al*., 2003). 2-[^{18}F]FDG-PET is recommended for evaluating spondylodiscitis and vertebral osteitis but not for OM in peripheral bones, whereas leukocyte scintigraphy is recommended (EANM guidelines).

Pathophysiology

OM is an inflammatory exudate within the bone marrow that elevates the medullary pressure; this compresses blood and lymph vessels, eventually leading to ischemia and bone necrosis. The necrotic bone may separate from the viable bone by granulation, resulting in sequestrum formation (**Figure 4**). The vital bone and periosteum form a sheath surrounding the necrosis area, referred to as an involucrum (**Figure 4**). Frequently, the periosteal bursts create a defect known as a cloaca that drains pus from the bone to the surrounding tissues, generating fistulation and abscess (**Figure 4**).

OM may appear in any bone. In children, tubular bones, such as the tibia and femur, are the most common sites of OM (**Figure 4)**.

Figure 4. Formation of Sequestrum and Fistula

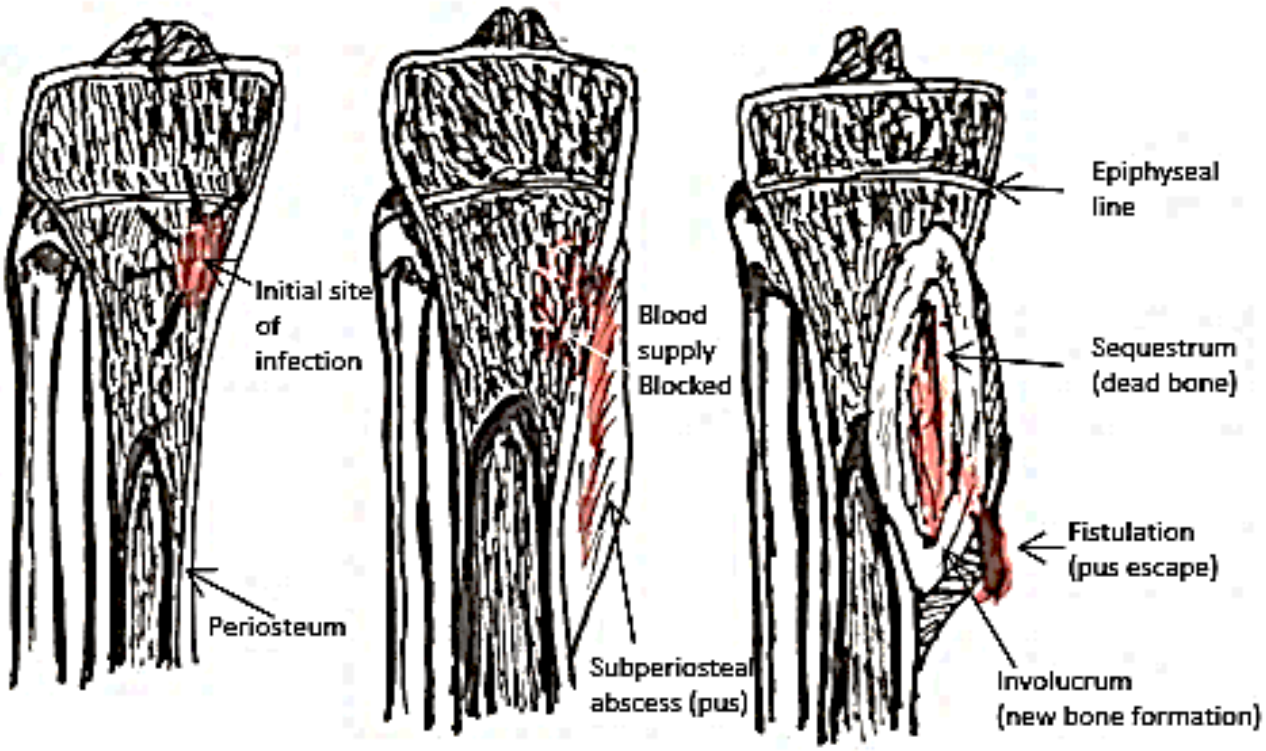

Figure 4. A sequestrum, involucrum, and fistula formation in the proximal tibial bone. (PA)

Blood Supply

The nature of the blood supply to the diaphysis, metaphysis, and epiphysis depends on age. Different patterns of blood supply explain the various appearances of infection and differences in imaging patterns of OM between children and adults (Resnick, 2002), (**Figure 5**).

Figure 5. Blood Supply of Long Bones

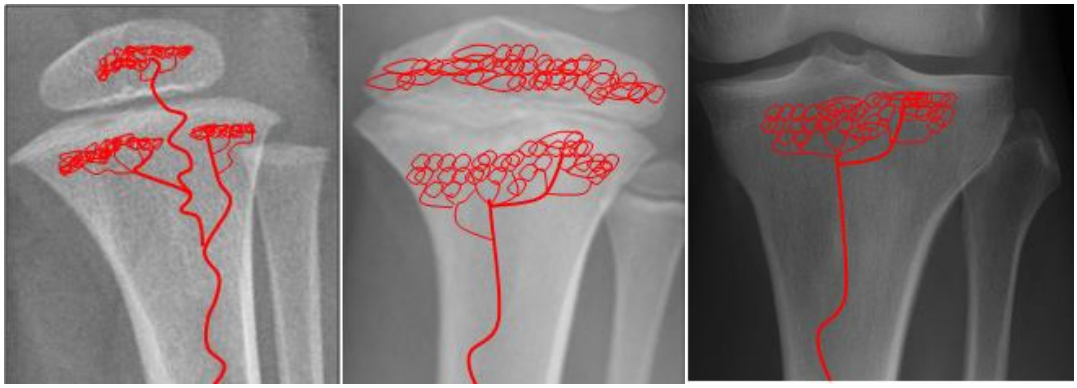

Figure 5. X-ray of the tibial bone and a schematic drawing showing vascularization of this long bone at different ages. To the left: Infant younger than 18 months. Metaphyseal and transphyseal blood vessels are present, allowing metaphyseal and epiphyseal origins of infection. Middle: Child between 18 months and 16 years. The epiphysis has unshared supplying vessels (veins and arteries), whereas the metaphysis and diaphysis share vessels. The result is a natural barrier, with the physis preventing OM from invading the epiphysis and joints. Therefore, children in this age group present with an initial and predominant metaphyseal focus of infection. Right: Adult after the closure of the growth plate; this removes the barrier between the metaphyseal and epiphyseal vessels. From age 16, restoration of the transphyseal vascularization may potentially cause the epiphyseal spread of infection (Inspired by Resnick, 2002).

Metaphyseal vessels contain slow-flowing blood, predisposing them to bacterial proliferation. Hence, the metaphysis is a common site of hematogenous OM. Traditionally, the growth plate has been considered a barrier to the epiphysial expansion of the infection in children over 18 months of age due to the particular vascularization pattern present in children (**Figure 5**). However, in infants under 18 months of age and adults, transphyseal vessels are present, providing a route for infection to spread between the metaphysis and epiphysis. The barrier has, however, recently been shown by MRI to be permeable. MRI is very sensitive for demonstrating subtle changes in the bone marrow that represent early signs of the spread of infection across the growth plate (Nguyen *et al*., 2017).

In rare conditions, the infection spreads predominantly through the circulus vasculosus articuli of Hunter, which supplies the epiphysis; this explains the rare occurrence of epiphyseal childhood OM (Rosenbaum *et al*., 1985). Bacteria can also migrate through the Haversian and Volkmann canal systems to spread throughout long bones.

SPECT Tracers:

Historically, the tumor-detecting tracer [^{67}Ga]Ga-citrate, introduced in the 1970s, was the only tracer with the potential for detecting infection until the use of ^{111}In-labeled autologous leukocytes was approved in the mid-1980s. (McAfee *et al.*, 1976a,b). However, several disadvantages

are associated with using [^{67}Ga]Ga-citrate as a tracer with a standard gamma camera. One is that suitable images are obtained only after a delay, usually 24-72 hours after injection; for this reason, the method, to some extent, does not meet the requirement for prompt diagnosis and treatment. Others are the images' low quality and the higher radiation burden incurred.

An advance was the introduction of radiolabeling of autologous leukocytes with ^{99m}Tc (Peters e*t al.*, 1986; Roddie *et al*., 1988; Datz *et al*., 1997). ^{99m}Tc-labeled leukocytes provide much better image quality for gamma camera imaging and decrease the radiation exposure to patients and technicians compared with ^{111}In-labeled leukocytes. Both of these labeling tracers for autologous leukocytes are used successfully in infection scintigraphy. However, the *in vitro* radiolabeling of autologous leukocytes is time-consuming, and reinfusion is not accomplished until three to four hours after their initial collection. Handling living cells *ex vivo* requires delicacy, and there is also the potential risk of transmission of blood-borne infections to technicians. The radiation exposure to the technician is also higher.

PET Tracers

In the late 1960s, Pacák *et al*. synthesized FDG. Later, in the 1970s, Ido *et al*. were the first to describe the synthesis of ^{18}F-labeled FDG. The compound was first administered to two human volunteers by Abass Alavi in 1976 at the University of Pennsylvania. Brain images obtained with an ordinary (*non*-PET) nuclear scanner demonstrated that 2-[^{18}F]FDG becomes concentrated in that organ. Since the 1990s, glucose-analog 2-[^{18}F]FDG, initially used in brain PET examinations and later primarily used in the detection and staging of cancers, has demonstrated its promising role in detecting and managing infections. Over the last two decades, hybrid PET/CT has become widely available. Specifically, PET can provide vital information at the molecular level and consequently can be used to detect disease activity at its earliest manifestation. 2-[^{18}F]FDG is the most commonly used PET tracer, but it cannot distinguish between malignancy, inflammation, and infection. CT provides the exact anatomical localization of possible findings on PET.

The germanium/gallium generator-produced radionuclide ^{68}Ga has become commercially available independently of an onsite cyclotron. ^{68}Ga is a positron-emitting gallium isotope that is used in PET diagnostics. Compared to ^{67}Ga, it has many advantages for the diagnosis of bone infections: Its half-life is only slightly longer than one hour (67.7 min), much shorter than the three-days (78 hours) half-life of ^{67}Ga, allowing patients to be given higher tracer activities without receiving high radiation doses and to be discharged almost free of radioactivity. Furthermore, the uptake phase of ^{68}Ga is short, as is whole-body image acquisition, allowing short-term imaging. Finally, when used in conjunction with CT, PET produces functional tomographic images with high spatial resolution, providing exact anatomical localization of the findings.

The introduction of PET/CT has revolutionized clinical PET. CT incorporates the anatomic information, thereby enhancing the interpretation of molecular function provided by PET. The leading scanner manufacturers no longer offer PET scanners without a CT component. Therefore, avoiding the potential risk of radiation-induced cancer associated with PET/CT examination and avoiding unwarranted scans are essential (**Figure 6**). PET/CT is solidly recommended for use in cases with a relevant clinical problem, the outcome depends on the PET/CT examination, and nonionizing alternatives such as MRI and US examination are inferior.

Radiation Exposure

Figure 6. Cancer Risk after CT

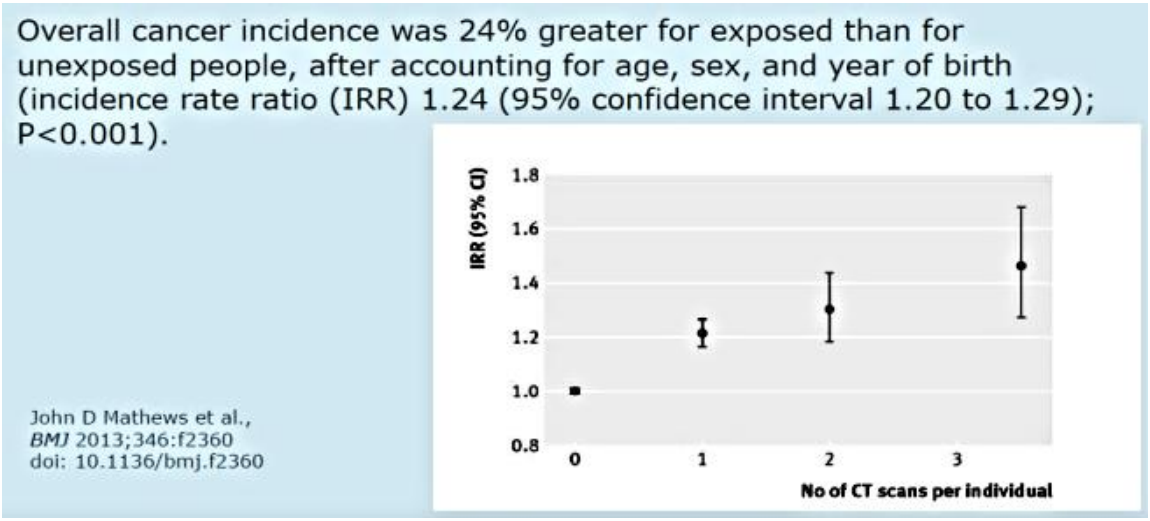

Figure 6. Cancer risk in 680,000 people exposed to computed tomography scans in childhood or adolescence: data linkage study of 11 million Australians. The figure is presented with the permission of John Mathews (Mathews *et al*., 2013) and BMJ.

Children, especially young children, are more sensitive to ionizing radiation than adults (Wall, 2004; Mathews *et al*., 2013) (**Figure 6, Table 1**). Their cells divide more often and live longer after radiation exposure, allowing potential cancers more time to develop. In modern health care systems, all procedures involving ionizing radiation exposure in children strive to optimize the reduction of dose burden without compromising the diagnostic performance and the image quality.

Table 1. Recommended Linear Dosing Guidelines, Critical Organ Dose, and Effective Dose to Healthy Subjects after Administration of 2-[^{18}F]FDG

Patient	Organ receiving the most significant radiation dose* mGy/MBq	Effective dose** mSv/MBq
Newborn	-	0.210
Child (1 y old)	Bladder, 0.51	0.080
Child (5 y old)	Bladder, 0.36	0.048
Child (10 y old)	Bladder, 0.24	0.032
Child (15 y old)	Bladder, 0.16	0.022
Adult	Bladder, 0.15	0.019

Reference (Stabin *et al*., 2018). ** Reference (Niven *et al*., 2003). The administered activity was 3.7-5.2 MBq/kg., minimum of 26.0 MBq* (Niven *et al.,* 2003; Mattsson *et al*., 2015; Stabin *et al*., 2018).

When using imaging modalities in children, radiation exposure should be balanced against the possibility of reaching a swift and valuable diagnosis in the individual case. Most procedures involving exposure to ionizing radiation are classical X-ray examinations. However, more advanced scans, such as CT and PET, play an increasing role in contributing to the overall radiation dose received through medical procedures.

Imaging infections is challenging, and no ideal imaging modality is available. The best imaging modalities and biomarkers should distinguish between infection and inflammation with high sensitivity and specificity in a way that is not related to the stage of infection, to its anatomical localization, or to blood flow and should be cost-effective, quickly performed, and results in low radiation exposure.

Animal Model

OM in children is most often acute. Bacteria usually reach the bone through the bloodstream, resulting in acute hematogenous OM. Rarely, an infection may spread to the bone from an adjacent infected focus or by direct introduction of bacteria through an open wound in the presence of an open fracture. Therefore, we used the below-mentioned animal model for hematogenous *S. aureus* to evaluate the bone-infection tracers applicable for PET and SPECT (**Paper I**). Localized OM was achieved by injecting *S. aureus* unilaterally into the femoral arteries of juvenile female domestic pigs as described in the model introduced by Johansen *et al*., 2012.

This group and others have noticed a similarity of the juvenile domestic pig model to the conditions pertaining to children, in whom OM most often involves the growth zones of the long bones of the lower extremities, perhaps due to more exposure to the long bones of the extremities to minor blunt trauma caused by childhood activities, creating a locus of little necrosis (Dartnell *et al*., 2012; Johansen *et al*., 2013). In 50% of cases, the affected children are less than five years of age,

and the condition is twice as frequent in boys as in girls (Gutierrez, 2005; Van Schuppen *et al*., 2012; Grammatico-Guillon, 2013). This may be due to the characteristics of blood supply to the long bones of juveniles (Resnick, 2002) (**Figure 5**).

Animal models are an essential link between *in vitro* testing and clinical studies (**Paper VIII**). A variety of animal models are usable in research on the pathophysiology, diagnosis, and therapy of OM (**Paper VIII)**. We refined a porcine juvenile pig model of *S. aureus*-induced OM (Alstrup *et al*., 2016; **Paper I**), and we used this model to test new potential tracers for OM in juveniles. The pigs developed foci of OM in the ipsilateral limbs, with minor signs of further spread to internal organs. The contralateral leg served as a control. We tested fifteen radioactive tracers.

MATERIALS AND METHODS:

The animal protocol used in the OM project is described in **Paper I**. The Danish Animal Experimentation Board approved the protocol under journal no. 2012-15-2934-00123 and 2017-15-0201-01239 in accordance with 2010/63/EU. The Danish Occupational Health Surveillance also approved it. A summary is given below.

The Animal Model

Hematogenous OM was induced in the right hindlimbs of clinically healthy and specific-pathogen-free Danish Landrace Yorkshire crossbred juvenile female pigs. After one week of acclimatization of the animals, a well-characterized *S. aureus* strain (Nielsen *et al*., 2009; Hasman *et al.*, 2010; Leifsson *et al*., 2010; Aalbæk *et al*., 2015) was introduced into the right femoral artery by intra-arterial inoculation as described by Johansen *et al*., 2012, 2013 (**Figure 7**). A clamp prevented the pathogen from spreading retrogradely to the rest of the body. This procedure does not involve trauma to the bone from the inoculation procedure, and ideally, OM can be induced in the inoculated limb without introducing systemic infection. Initially, extraosseous conditions were not always avoided. Therefore, it was necessary to refine the model; briefly, younger pigs weighing 20 kg (~9 weeks old) were used instead of pigs weighing 40 kg, and penicillin was administered to the pigs as described by Alstrup *et al*., 2016.

None of the pigs developed OM in the noninoculated (left) hindlimb; hence, the left hindlimb served as a control for the infected (right) hindlimb.

Figure 7. Preparation of Pigs

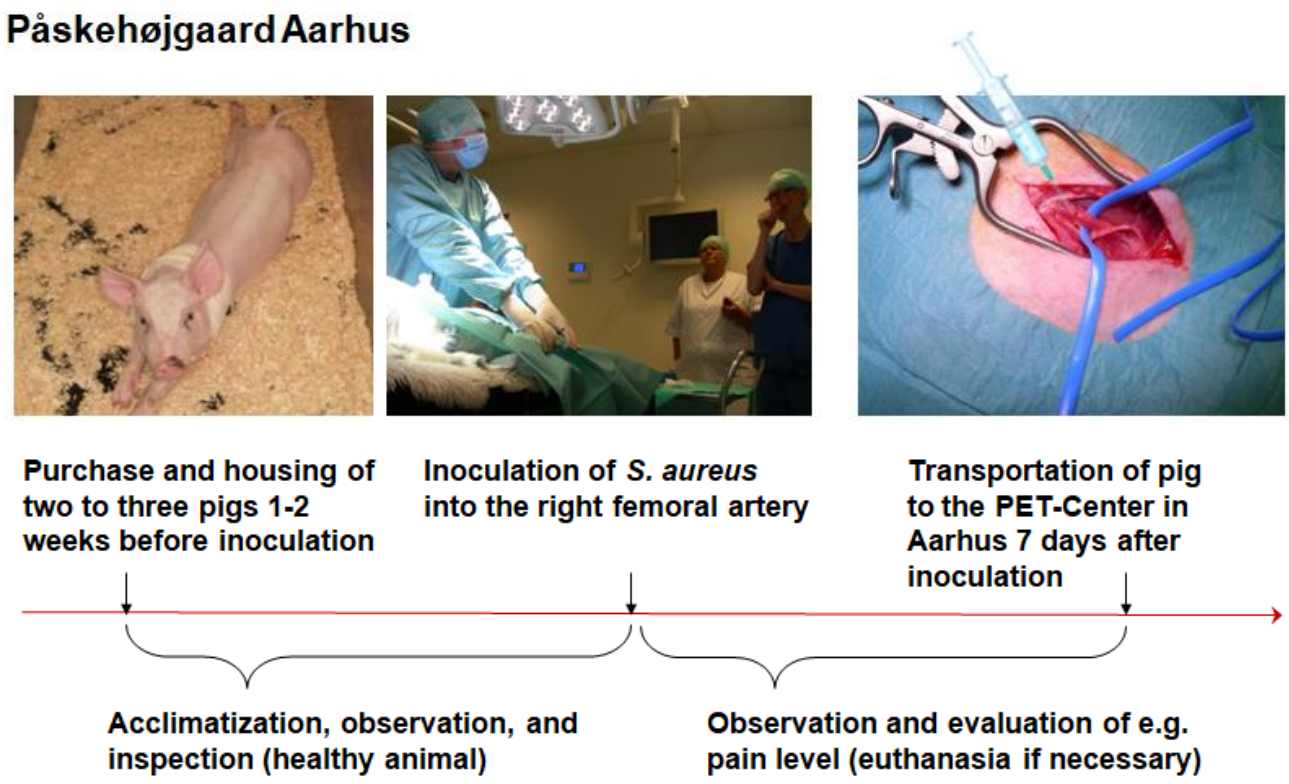

Figure 7. The sequence of acclimatization after purchase of pigs (left); inoculation of the right femoral artery with the well-characterized *S. aureus* strain (middle and right); and timeline (below).

One to three pigs were inoculated at a time, and if OM lesions were seen on CT after one week, one or two pigs were then subjected to scanning with radioactive tracers the day after CT. If a pig reached one of several predefined humane endpoints as listed in the protocol and approved by the authorities before the end of the week, it was euthanized and not scanned (Alstrup *et al*., 2016).

We planned a one-week protocol for testing involving acute OM (Lew *et al*., 2004). We attempted to prolong the protocol for two weeks, allowing more chronic OM to evolve. Nevertheless, four of the five two-week pigs were euthanized prematurely for humane reasons. We did not consider this high ratio of animals reaching the humane endpoints acceptable; thus, the two-week protocol was abandoned, and only a single pig was scanned in this protocol. For adequate blood sampling of metabolites in connection with the dynamic scans, we used 40-kg pigs (**Table 3,** page 43, pig 1-4, **Paper I**) instead of the 20-kg pigs used in the original model (Johansen *et al*., 2013). However, several of the 40-kg pigs were euthanized before PET and SPECT scanning due to the dissemination of *S. aureus* to the lungs and other internal organs (**Figure 8, Paper II).** Therefore, we decided to refine our model to improve the success rate by reducing the pigs' weight, returning to the original model (Johansen *et al*., 2013) (**Table 3** page 42, pig 5-27, **Papers II-VIII**). In addition, from the onset of the first clinical signs of infection, we treated seven pigs (one 40-kg and six 20-kg) with procaine benzylpenicillin, to which the bacterial strain was susceptible (Alstrup *et al*., 2016). We examined the effects of long-term anesthesia (up to 18 hours), repeated blood sampling (up to 20 mL blood per kilogram body weight), and road transportation (up to 1.5 hours between two imaging centers) on critical variables of the lung, heart, and brain function in the well-established pig model of *S. aureus* OM (Alstrup *et al*., 2020b). All pigs were scanned in the dorsal recumbent position (**Papers I-IX**)

Figure 8. Abscesses in the Lungs

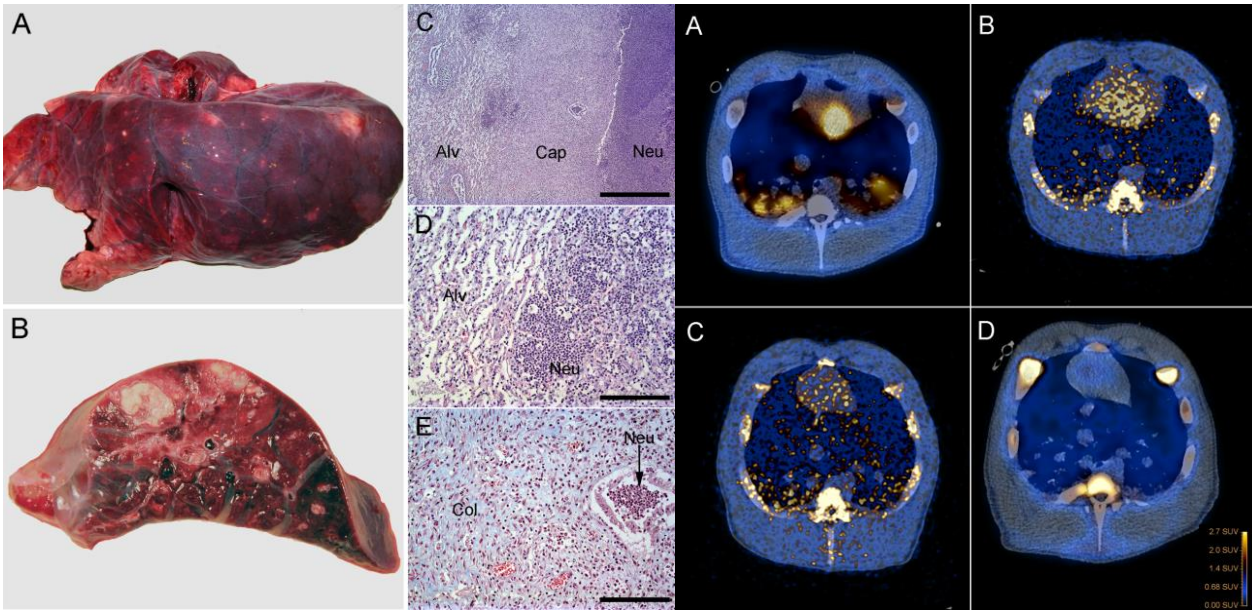

Figure 8. Gross pathology of abscesses in the lungs (A, B) of pig 2 (**Table 3,** page 42). (A) The costal surface of the left lung with disseminated abscesses. (B) The transverse section through the left ling presents two abscesses. (C-E) Histopathology of the capsule of a subacute lung abscess (C-E). (C) Hematoxylin and eosin staining revealed the presence of neutrophils (Neu), a capsule (Cap) consisting of granulation tissue, and surrounding atelectatic lung alveoli (Alv). Bar = 1 mm. (D) Hematoxylin and eosin staining of lung tissue peripheral to the abscess capsule, demonstrating acute suppuration, i.e., the presence of neutrophils (Neu), in the alveoli and atelectatic alveoli (Alv). (E) Masson trichrome staining (collagen is stained blue) of the central part of the abscess capsule, showing an abundance of collagen (Col) and neutrophils (Neu) within a bronchiole. Bar (D, E) = 100 µm. Fused PET/CT images of lungs with abscesses and axial views, with A: 2-[^{18}F]FDG, B: L-[*S*-methyl-^{11}C]methionine, C: [^{11}C]PK11195, and D: [^{68}Ga]Ga-citrate (**Paper II**).

In a recent study, we examined whether repeated noninvasive scanning in the ventral recumbent position *per se* affected internal organs and postscan welfare of animals in Göttingen minipigs (**Paper X**).

Tracers for Imaging of OM

Molecular nuclear medicine offers a variety of approaches and radiopharmaceuticals that can be used not only for diagnostic purposes but also for *in vivo* histological characterization of lesions, for the correct assessment of disease activity, for planning appropriate therapy, and for response evaluation. Different approaches to targeting OM were examined, including bone-seeking, blood flow, metabolism, biofilm, and some of the signaling molecules involved in the OM process (**Table 2, Papers I-VII** and **IX**).

Table 2. Tracers

Tracer	Radionuclide Half-life	Radiation Dose
PET		
[^{15}O]H_2O	2.04 min	0.0011 mSv/MBq*
[^{11}C]PK11195	20.38 min	0.0028 mSv/MBq****
L-[*S*-methyl-^{11}C]methionine	20.38 min	0.0082 mSv/MBq*
2-[^{18}F]FDG	**109.77 min**	**0.019 mSv/MBq***
[^{68}Ga]Ga-citrate	67.7 min	0.020 mSv/MBq**
[5-^{11}C-methoxy]donepezil	20.38 min	0.0052 mSv/MBq***
[^{68}Ga]Ga-DOTA-K-A9	67.7 min	Not done
[^{68}Ga]Ga-DOTA-GSGK-A11	67.7 min	Not done
[^{68}Ga]Ga-DOTA-Siglec-9	67.7 min	0.024 mSv/MBq*****
Na[^{18}F]F	109.77 min	0.024 mSv/MBq*
[^{68}Ga]Ga-NOTA-ubiquicidin	67.7 min	0.017 mSv/MBq*******
SPECT		
[^{99m}Tc]Tc-HDP/DDP	6.01 h	0.0049 mSv/MBq*
[^{99m}Tc]Tc-IL-8	**6.01 h**	**0.0041 mSv/MBq*******
[^{111}In]In-oxine-leukocytes	**2.8 d**	**0.36 mSv/MBq***
[^{99m}Tc]Tc-HSA-nanocolloid	6.01 h	0.0097 mSv/MBq**

Table 2. Tracers used in the experiments described in the thesis. *Adult radiation dose from ICRP Publication 128; Mattsson *et al.*, 2015. **Adult radiation dose from ICRP Publication 80, Valentin, 1998. ***Calculation by Gjerløff *et al*., 2014. ****Calculation by Kumar *et al*., 2010. *****Calculation by Virtanen *et al*., 2017. *******Calculation by Ebenhan *et al*., 2018. *******Calculation by Bleeker-Rovers *et al*., 2007. The dosimetry of the phage-based tracers [^{68}Ga]Ga-DOTA-K-A9 and [Ga-68]Ga-DOTA-GSGK-A11 is unknown. The radiation dose depends on physical parameters (type and energy of radiation, physical half-life) and pharmacokinetics (uptake and retention times in individual organs and tissues). The physical parameters are known, but the determination of the pharmacokinetics often requires a paper in itself. However, **Table 2** shows that other possible infection tracers based on ^{68}Ga (and ^{18}F) have factors of ~0.02 mSv/MBq; thus, the radiation dose received by the animals in this study was likely of this order, e.g., within a factor of 2.

[^{15}O]H_2O (flow)

Except in the case of purely diffusion-limited tracers, the blood perfusion of the tissue influences the tracer kinetics. A noninvasive, quantitative method for studying perfusion is the use of dynamic [^{15}O]water-PET. Water (H_2O) passes quickly through the capillary walls, and the first-pass extraction fraction in tissue contains close to 100% of the perfused water (Jødal *et al*., 2017a). As [^{15}O]water is thoroughly mixed within the blood plasma, its initial uptake reflects blood flow in the tissue. Additionally, as inflamed tissue generally has increased perfusion, we measured blood perfusion in the areas that were studied with infection tracers. To our knowledge, this was the first time [^{15}O]water has been used to study OM. We performed kinetic modeling to study the uptake and release of the tracers. Volumes of interest (VOIs) on lesion sites in the right limb were drawn and compared with those on noninfected sites using similar VOIs in the left limb. In a specific VOI, the mean PET signal (Bq/mL), measured over time, was analyzed.

The uptake and release of [^{15}O]water were modeled using a 1-tissue compartment model (1TCM) (Jødal *et al.*, 2017a), i.e., a model with input from the blood to a single tissue compartment;

nothing further happens to water in tissue (except that it returns to the blood pool). The half-life of ^{15}O is two minutes, limiting the time available for scanning to a few minutes and reducing the delay before initiating a new scan, as well as minimizing the radiation dose, which is relevant in the case of human studies.

A pilot study examined a few pigs where the radioactively labeled water was injected into the bone through CT-guided screws placed in the OM lesions in the right hindlimb and the identical anatomical site in the left leg. We also measured the medullar bone pressure in both limbs (**Figure 9**).

Figure 9. Measurement of Marrow Pressure

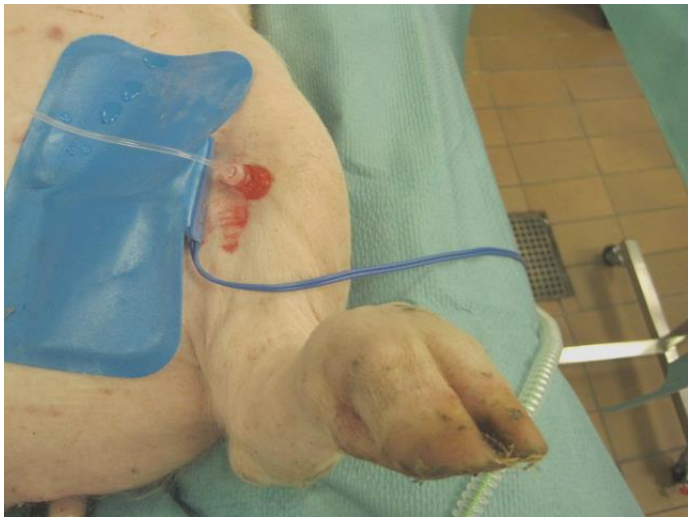

Figure 9. Setup for measurement of bone marrow pressure in the medial left distal femur (not yet published).

[^{11}C]PK11195 (Immune Response, Steroid Synthesis, and Apoptosis

[^{11}C]PK11195(1-[2-chlorophenyl]-*N*-[1-methyl-propyl]-3-iso-quinoline carboxamide) is an isoquinoline carboxamide and a high-affinity ligand for the 18-kDa mitochondrial translocator protein (TSPO), previously known as the peripheral benzodiazepine receptor (PBR). The TSPO receptor is expressed intensely on cells of the mononuclear phagocyte lineage. Since the early 1980s, [^{11}C]PK11195 has been used to image inflammatory diseases in the human brain by PET based on the low expression of PBRs in normal brain tissue and the high expression of PBRs in activated microglia, the resident phagocytes in brain tissue (Bananti *et al.* 2000; Turner *et al*., 2004). [^{11}C]PK11195 has also been used to visualize inflammation at other anatomical sites, such as sites in rat models in which macrophage-dominated infiltrates of blood vessels and tissue membranes surrounding loosening prostheses are present (Cagnin *et al*., 2002; Ren *et al*., 2012) and in humans (Pugliese *et al*., 2010). Despite the widespread use of [^{11}C]PK11195-PET, the whole-body distribution and dosimetry of [^{11}C]PK11195 have not been studied until recently (Roivainen *et al*., 2009; Hirvonen *et al*., 2010; Kumar *et al*., 2010).

L-[S-methyl-^{11}C]Methionine (Protein Synthesis)

Methionine is a naturally occurring essential amino acid that is transported into cells via the L-type amino acid transporter-1. Methionine is necessary for protein synthesis and is also involved in the synthesis of phospholipids. Methionine, thus, reflects both amino acid transport and protein synthesis. When cells replicate, the demand for proteins, phospholipid synthesis, and essential amino acids increases. Therefore, we assumed that methionine accumulation also reflects tissue healing in OM. PET imaging using the positron-emitting isotope ^{11}C can visualize methionine accumulation, reflecting increased amino acid transport. Although L-[*S*-methyl-^{11}C]methionine is known to accumulate in inflammatory lesions (Stöber *et al*., 2006; Hirata *et al*., 2012), it is used primarily for the detection of brain tumors (Zhao *et al*., 2008). The biodistribution of L-[*S*-methyl-^{11}C]methionine was evaluated in children and young adults 5-15 min after injection of 740 MBq L-[*S*-methyl-^{11}C]methionine/1.7 m^2 of body surface area (Harris *et al*., 2013). High uptake of (L-[*S*-methyl-^{11}C]methionine was found in the liver and pancreas, consistent with the anabolic functions of these organs and excretion to the bladder. That study does not mention the small intestine; however, the images presented indicated that there is slight excretion in that organ. The low physiological uptake that occurs in the pelvis and extremities facilitates OM diagnostics in these areas.

2-[^{18}F]FDG (Glucose Metabolism)

2-fluoro-2-deoxy-D-glucose (FDG) is a glucose analog that cells take up via glucose transporters (GLUTs). Like glucose, the FDG molecule is phosphorylated by the glucose-metabolizing enzyme hexokinase at the first step in glycolysis. However, while the metabolic product of glucose (glucose-6-phosphate) becomes metabolized further, the metabolic product of FDG is FDG-6-phosphate, a relatively poor substrate of the enzyme. For this reason, the subsequent metabolism of FDG-6-phosphate in the glycolytic chain is effectively blocked. At the same time, because the cell membrane is poorly permeable to FDG-6-phosphate, the metabolite remains >trapped< within the cell (Sokoloff *et al*., 1977). The result is a progressive, time-dependent accumulation of radioactive positron-emitting 2-[^{18}F]FDG-6-phosphate in tissues in an amount that correlates with glucose metabolism. Unlike glucose, 2-[^{18}F]FDG is rapidly excreted by the kidneys, and this improves image contrast by reducing the background signal emanating from the tracer that is not taken up by the tissue (Gallagher *et al*., 1978). These qualities make 2-[^{18}F]FDG an optimal choice for imaging glucose metabolism.

Many types of cancer cells rely heavily on glycolysis, in which glucose is metabolized to lactate to produce energy and, therefore, take up glucose for aerobic glycolysis, known as the Warburg effect (Potter *et al*., 2016). For this reason, 2-[^{18}F]FDG is widely used in cancer diagnosis. Physiologically, the brain, striated muscle, and brown fat have high physiological glucose uptake. Due to the increased expression of GLUTs on cells that occurs during acute and chronic inflammation, glucose also accumulates in immune cells (Zhao *et al*., 2002; Signore *et al*., 2011). Accordingly, 2-[^{18}F]FDG is increasingly being used as an infection tracer. A review of radionuclide imaging of OM reported a sensitivity of >95% and a specificity of 75-99% for 2-[^{18}F]FDG-PET/CT (Palestro, 2020).

However, a limitation of this method is its lack of specificity, as FDG metabolism may reflect the presence of infections, inflammatory, reparative, and reactive changes, as well as cancer. Another drawback is physiological uptake in those organs and tissues with high FDG metabolic activity or excretion, potentially leading to incorrect interpretation. False positives can occur in organs with unexpectedly high physiological uptake. False negatives can occur when an infectious, cancerous, or inflammatory focus is overlooked because it is located in tissue that is expected to have a high uptake of FDG.

[^{68}Ga]Ga-Citrate (de novo Synthesis)

Gallium is a metal ion that shares chemical properties with iron and accumulates in infectious and inflammatory sites (Nanni *et al*., 2010). A significant difference between gallium (Ga^{3+}) and iron (Fe^{3+}) is the inability of gallium to be reduced *in vivo*. In contrast, ferric ions are reduced and become part of tissues, while gallium remains bound to its carrier protein (Hoffer, 1980). Iron transfer involves the reduction of Fe^{3+} to Fe^{2+}. Ga^{3+} is not reduced, and the elimination rate of gallium is slower than that of iron (Chitambar *et al*., 2016). [^{67}Ga]Ga-citrate scintigraphy was the leading modality used in imaging inflammation and infections of musculoskeletal origin in the 1970s and early 1980s (Gelrud *et al*., 1972; Balair *et al*., 1973; Burleson *et al*., 1973; Littenberg *et al*., 1973; Deysine *et al*., 1974). The relatively long half-life of ^{67}Ga of 78 hours results in a relatively high radiation dose per MBq of activity injected compared to other diagnostic radionuclides; this sets quite low limits for the amount of radioactivity that can safely be injected, and the broad energy spectrum of the gamma rays emitted by ^{67}Ga reduces image quality and resolution. Other drawbacks of using ^{67}Ga for imaging are its high background activity, interference from uptake in liver and bowel uptake or activity, a delay in postinjection imaging of at least 48-72 hours, which is undesirable if early diagnosis is needed, the associated high radiation exposure, and the high cost of the radionuclide. However, late postinjection imaging is advantageous if a late image is desired, as in cases of slow chronic infections. In our protocol, it was necessary to acquire pictures within one to two hours, as it was impossible to wait for all of the injected gallium to be taken up by the tissues or excreted, also making [^{68}Ga]Ga-citrate a better choice.

[^{68}Ga]Ga-citrate is a marker of infection and accumulates solely in infectious lesions (Nanni *et al*., 2010). Compared to ^{67}Ga, imaging infections with various PET tracers is quicker and provides higher resolution with less injected activity. ^{68}Ga has a shorter half-life, provides practical imaging within 60 min postinjection, is cost-effective, results in less radiation exposure, and the early time point causes less background uptake in the liver and bowel. The cellular uptake and accumulation of [^{68}Ga]Ga-citrate in infectious foci are complex and not fully understood. Once injected, the Ga-citrate complex quickly dissociates into Ga^{3+} and $citrate^{3-}$ within the blood. Then, 99% of the gallium ions are attached to transferrin (Tsan, 1985; Kumar *et al*., 2011) and accumulate in inflammatory lesions. Thus, the actual tracer is [^{68}Ga]Ga-transferrin. In addition, some ^{68}Ga may attach to bacterial siderophores, to lactoferrin inside neutrophils which are present in high concentrations in abscess fluid, and to free lactoferrin at the site of infection, where macrophages partially absorb it (Hoffer, 1980; Palestro *et al.*, 2004a; Kumar *et al*., 2012). For imaging of OM, [^{68}Ga]citrate appears promising (Mäkinen *et al*., 2005; Nanni *et al*., 2010; Salomäki *et al*., 2017).

[5-^{11}C-methoxy]Donepezil (Signaling)

[5-^{11}C-methoxy]donepezil is a non-competitive, reversible acetylcholinesterase ligand that was previously validated for imaging cerebral levels of acetylcholinesterase (Okamura *et al*., 2008). The biodistribution of [5-^{11}C-methoxy]donepezil used to image acetylcholinesterase recently showed significant uptake in a postoperative abscess of a pig (Gjerløff *et al*., 2014). Nonneuronal cholinergic signaling is involved in immune responses to infections, especially in the responses of lymphocytes (Kawashima *et al*., 2012), indicating that acetylcholinesterase is not only a neurotransmitter but also has a regulatory role in immune cells that express the receptor for the neurotransmitter.

Jørgensen *et al.* studied the uptake of [5-^{11}C-methoxy]donepezil during infection and inflammation in mice, pigs, and humans. In all three species, [5-^{11}C-methoxy]donepezil showed elevated uptake in infectious lesions, and one human with pneumonia had an exceptionally high uptake (Jørgensen *et al*., 2017).

[^{68}Ga]Ga-DOTA-K-A9 and [^{68}Ga]Ga-DOTA-GSGK-A11 (S. aureus Biofilm)

When *S. aureus* enters the skin, both neutrophils and macrophages migrate to the site of infection. *S. aureus* avoids this imminent attack by the host's immune system in various ways. For example, by blocking the chemotaxis of leukocytes, sequestering host antibodies, hiding from detection by forming a polysaccharide capsule, forming complex microcolonies termed "biofilms" on inert surfaces and dead tissues, and resisting destruction after ingestion by phagocytes. In conjunction with the multitude and redundancy of its virulence factors in avoiding host responses and influencing disease, the biofilms formed by *S. aureus* on inert surfaces and dead tissues represent a sheltered environment for the bacteria, offering protection from the effects of antibiotics and host immune defenses (Hoiby *et al.*, 2010). Therefore, biofilms induce an ongoing inflammatory reaction (Costerton *et al*., 1999). Although neutrophils are capable of invading biofilms, bacterial colonies can prevent and survive an immune attack. Current therapies for chronic biofilm-mediated infections are limited but may be essential when planning surgery or during prolonged treatment. Bacteriophages are viruses that infect bacteria exclusively and have no specificity for mammalian cells (Rusckowski *et al*., 2004). Most bacteriophages are specific for a single bacterial strain. The binding mechanism consists of the attachment of the phages to particular surface receptors or domains located on the bacterial surface; the phages subsequently transfer their genetic material into the host cell, causing it to become dedicated to phage replication/reproduction (Summers *et al*., 2001). We previously examined two ^{68}Ga-labeled peptides with affinity for *S. aureus* biofilms that were selected from a phage display, [^{68}Ga]Ga-DOTA-K-A9 and [^{68}Ga]Ga-DOTA-GSGK-A11, and evaluated their potential as bacteria-specific PET imaging agents (Nielsen KM *et al*., 2016, 2018).

[^{68}Ga]Ga-DOTA-Siglec-9 (Leukocyte Trafficking)

Vascular adhesion protein 1 (VAP-1), which is involved in leukocyte extravasation and is expressed on monocytes and neutrophils, is important in leukocyte trafficking (Koskinen *et al*., 2004, Arvilommi *et al.,* 1996). Sialic acid-binding immunoglobulin-like lectin 9 (Siglec-9) is a natural ligand of VAP-1, and the PET tracer [^{68}Ga]Ga-DOTA-Siglec-9 binds to VAP-1. Our collaborators at Turku PET Centre have found this tracer promising for detecting infection and inflammation (Jaakkola *et al*., 2000; Jalkanen *et al*., 2008; Aalto *et al*., 2011; Athinen *et al*., 2014; Retamal *et al*., 2016; Vitanen *et al.*, 2017).

[^{68}Ga]Ga-NOTA-Ubiquicidin (Bacterial Cell Membranes)

Differentiation between bacterial infection and sterile inflammation is of particular interest. Theoretically, highly infection-specific radiolabeled antimicrobial peptides such as the human antimicrobial peptide ubiquicidin appear to be a worthy approach. Ubiquicidin is found in mammals, birds, amphibians, and insects and protects these animals against infection (Akhtar *et al*., 2005). Antimicrobial peptides such as ubiquitin can distinguish among mammalian, bacterial, and fungal cells. They may target vector candidates for molecular imaging due to their selectivity for bacterial cell membranes in the innate immune system response (Ebenhan *et al*., 2018; Bhusari *et al*., 2019).

A synthetic component derived from the human antimicrobial peptide ubiquicidin (UBI) labeled with ^{99m}Tc was recently used to distinguish bacterial infections from sterile inflammatory processes (Welling *et al*., 2001; Brouwer *et al.,* 2006). Welling *et al*. examined several peptides and concluded that UBI_{29-41} (Thr-Gly-Arg-Ala-Lys-Arg-Arg-Met-Gln-Tyr-Asn-Arg-Arg, molecular weight 1693 Da), a derivative of the bacterial binding domain of ubiquicidin, is an optimal candidate for the differentiation of bacterial and fungal infections in mice, rats, and rabbits. We used

the small cationic [^{68}Ga]Ga-NOTA-UBI$_{29-41}$, a synthetic peptide derived from humans that electrostatically interacts with the anionic portions of bacterial membranes, as a bacteria-specific imaging probe (Ebenhan *et al*., 2018). This UBI binds preferentially to bacteria *in vitro*; it does not bind to activated leukocytes and can distinguish bacterial infections from inflammation with greater specificity than other UBI peptides (Ferro-Flores *et al*., 2003; Akhtar *et al*., 2005; Ebenhan, 2014a; Ebenhan, 2014b). A pooled meta-analysis of clinical studies in which [^{99m}Tc]UBI$_{29-41}$ was used was very encouraging, showing a sensitivity of 94%, a specificity of 95%, and an accuracy of 94% in various clinical settings (Welling *et al*., 2019).

[^{99m}Tc]Tc-DPD/-HDP and Na[^{18}F]F (Bone Remodeling)

Phosphonates in the blood are taken up by forming bone and incorporated into the hydroxyapatite crystal that constitutes a major part of the bone matrix. The phosphonates used in bone-scintigraphy are [^{99m}Tc]technetium-methylene-diphosphonate ([^{99m}Tc]Tc-MDP), [^{99m}Tc]technetium-hydroxy-methylene-diphosphonate ([^{99m}Tc]Tc-HDP), and [^{99m}Tc]technetium-2,3-dicarboxy-propane-diphosphonate ([^{99m}Tc]Tc-DPD). The clinical differences among these three bisphosphonates are minor (Frühling, 1986). The uptake reflects blood flow and the rate of new bone formation, and the tracer accumulates in both bone tumors and bone infections in locations where the body is replacing degrading bone lesions.

Na[^{18}F]F-PET is an emerging alternative to conventional scintigraphy for the evaluation of bone metabolism. Na[^{18}F]F is a bone-seeking agent that is taken up through mechanisms similar to those involved in the uptake of [^{99m}Tc]Tc-DPD. Na[^{18}F]F binds to bone faster than [^{99m}Tc]Tc-DPD due to its smaller molecular size and lack of protein binding (Francis *et al*., 1980; Piert *et al*., 1998). Na[^{18}F]F is reported to have a twofold higher bone uptake and better sensitivity for metastatic osteoblastic metastases (Beheshti *et al*., 2015). The increased uptake at sites of rapid blood clearance within bones results in a quickly achieved high bone-to-background ratio. That and the high sensitivity of modern PET scanners allow the acquisition of high-resolution images beginning 15-30 min after administration of the radiopharmaceutical. Imaging is completed within one hour after injection, compared to several hours required for [^{99m}Tc]Tc-DDP imaging. The radiation dose from Na[^{18}F]F bone scans is similar to that received during [^{99m}Tc]Tc-MDP imaging.

We used [^{99m}Tc]Tc-DPD-SPECT/CT to examine bone remodeling in pigs. We did not perform triple-phase bone scintigraphy or late imaging. We observed no tracer uptake in the OM lesions compared to the similar anatomical location in the noninfected hindlimb (**Paper II**). We, therefore, also used sodium fluoride Na[^{18}F]F in the present study.

Although exceptional results have been reported for the use of Na[^{18}F]F in the detection of bone metastases in adults, with higher sensitivity than obtained with conventional bone-scintigraphy (Schirrmeister *et al*., 1999), and it is reported to help diagnose battered child syndrome (Drubach *et al*., 2008), published data on pediatric patients are scarce, and further studies are necessary to confirm that sensitivity is also higher in the pediatric patients and to evaluate the impact on clinical management.

[^{99m}Tc]Tc-IL-8 (Chemokine)

Suppurating inflammatory lesions such as OMs caused by *S. aureus* attract neutrophils and macrophages (Luster *et al*., 1998; Zurek *et al*., 2015). Neutrophils express two types of interleukin-8 (IL-8)-receptors, the G-protein-coupled C-X-C motif chemoreceptors 1 and 2 (CXCR1 and CXCR2) (Luster *et al*., 1998), and IL-8 binds to these receptors with high (0.3-4 nM) affinity (Holmes *et al*., 1991; Murphy *et al*., 1991; Lee *et al*., 1992; Cerretti *et al*., 1993). IL-8 (also denoted

CXCL8, the first chemokine to be characterized) acts in humans as a chemoattractant, a primer, and an activator of neutrophils during inflammation in various contexts (Harada *et al*., 1994; Luster *et al*., 1998; Scapini *et al*., 2000; Zeilhofer *et al*., 2000; Jalkanen *et al*., 2008; Sadik *et al*., 2011; Tecchio *et al*., 2014; Zurek *et al*., 2015). Like several other cell types, neutrophils initiate IL-8 synthesis in response to proinflammatory stimuli (Strieter *et al*., 1992). Isolated lipopolysaccharide-stimulated porcine pulmonary alveolar macrophages secrete IL-8 and have chemotactic activity toward neutrophils (Goodman *et al*., 1991), and IL-8-receptors are upregulated in various organs during inflammatory and infectious diseases in the pig (McIlwain *et al*., 2010; van Malenstein *et al*., 2010). Osteoclasts produce IL-8 (Rothe *et al*., 1998), and IL-8 stimulates osteoclast genesis and bone resorption independently of the receptor activator of the core-factor kappa-B ligand (RANKL) pathway (Bendre *et al*., 2003). IL-8 may be necessary for RANKL-induced osteoclast formation (Kopesky *et al*., 2014). In a previous study, Gross *et al*. showed that ^{131}I-labeled IL-8 could be used to visualize OM lesions during active foot infections in diabetic patients (Gross *et al*., 2001). However, Rennen *et al.* demonstrated that radiolabeling with iodine affected the *in vivo* biodistribution of IL-8 (Rennen *et al.*, 2002a). They also showed that labeling with ^{99m}Tc was preferable to labeling with ^{131}I for clinical applications, as the target-to-background was superior and the radiation exposure was lower (Rennen *et al.*, 2002b). This group also showed a better target-to-background ratio for ^{99m}Tc-labeled IL-8 than was obtained with [^{67}Ga]Ga-citrate or [^{99m}Tc]Tc-MDP (Gratz *et al*., 2001) and accumulation of a high total fraction of the tracer in inflamed tissues, both *in vivo* and *in vitro* (7-15% ID) (Rennen *et al*., 2003). They also prepared material with high specific activity (80 MBq/μg IL-8 and activity as low as 70 ng/kg protein, making the labeled chemokine a potential tracer for OM in humans (Rennen *et al*., 2002a). Therefore, we selected ^{99m}Tc-labeled IL-8 and tested the tracer as a possible alternative to leukocyte scintigraphy for imaging of acute OM.

[^{111}In]In-oxine-Leukocytes (Leukocyte Homing)

Since the 1970s, traditional nuclear imaging of infection has included labeled leukocyte scintigraphy (McAfee *et al.*, 1976a, 1976b; Thakur *et al*., 1977a), which detects tagged white blood cells migrating to the site of infection through chemotaxis and diapedesis. Indium-111 chelated with 8-hydroxyquinoline (oxine) is the most efficient of several radioactive particles and soluble agents that have been investigated for labeling leukocytes (MacAfee *et al*., 1976a, 1976b). Most labeled leukocytes are neutrophils, and the procedure helps detect neutrophil-mediated inflammatory processes, i.e., bacterial infections. It is less useful for illnesses in which the predominant cellular response is not neutrophilic, such as most opportunistic infections and spinal OM, because lymphocytes are susceptible to radiation, and the maximum specific activity tolerated is 20 μCi/10^8 cells (Trowell, 1952; Signore *et al*., 1983; Thakur *et al*., 1984). The accepted activity means that only 20 μCi can be routinely administered to patients, and this amount is unsuitable for *in vivo* diagnostic use. However, it is unlikely that the administration of labeled lymphocytes would cause detrimental effects such as lymphoid malignancy, as these cells are usually eliminated through apoptosis or phagocytosis. Liquid-soluble [^{111}In]In-oxine diffuses through the cell membrane, and up to 90% of the activity remains associated with intracellular components at 22 hours postinjection (Thakur *et al*., 1977b). Its insignificant elution makes ^{111}In-labeling of cells unsurpassed by any other radionuclide.

When injected intravenously into a patient, radiolabeled white blood cells migrate rapidly to the lungs and, if not damaged, proceed to the liver, spleen, and reticuloendothelial system, including the bone marrow; if an infection is present, approximately one hour later, the injected cells further migrate to infected tissue due to chemotactic attraction caused by biofilms and their soluble products. *In vitro* labeling of leukocytes is time-consuming and poses a personnel safety risk of radiation exposure, infection, and cross-contamination. It requires isolating leukocytes from a patient,

labeling them *in vitro*, and finally reinjecting the leukocytes. ^{99m}Tc-labeling has also proven useful (Palestro *et al*., 2020). [^{99m}Tc]hexamethyl-propylene-amine-oxine (HMPAO)-labeled leukocytes are better for use in children (Jaakkola *et al*., 1998); in our work, we only had access to [^{111}In]In-oxine.

[^{99m}Tc]Tc-HSA-nanocolloid (Red Bone Marrow)

[^{99m}Tc]Tc-HSA-nanocolloids, usually ^{99m}Tc-labeled colloidal ~100-nm nanoparticles without infection-specific uptake for scintigraphy or SPECT imaging, leak into inflamed tissues as a result of nonspecific extravasation due to increased vascular permeability. Once they enter the inflammatory foci, they accumulate through phagocytosis by cells of the reticuloendothelial system, including macrophages and granulocytes. Thus, they accumulate in both sterile and infectious inflammatory regions. They are characterized by rapid blood clearance, and an excellent target-to-background ratio is obtained soon after the injection (De Schrijver *et al*., 1987). They have been helpful in the early diagnosis (within 60 min) of bone and joint infections, with high sensitivity reported (Nijhof *et al*., 1997).

This radiopharmaceutical is no longer used in this application but remains a valuable tracer in bone marrow scans. Accumulation of leukocytes in the natural reservoir of healthy red bone marrow can lead to incorrect interpretation of leukocyte scans. This is a problem in prosthesis-related OM when the insertion of prosthesis material has displaced the marrow. To facilitate understanding of leukocyte scintigraphy and bone marrow scintigraphy, ^{99m}Tc-labeled nanocolloid is usually a valuable supplement. The particles accumulate in the liver, spleen, and bone marrow, corresponding to normal leukocyte uptake (Palestro *et al*., 2004b) and bone marrow scans, thus providing a map of physiological white cell uptake. Any discordance in white cell uptake between the two scans indicates a focus of infection (Mettler *et al*., 2012). Due to the different photon energies of ^{111}In and ^{99m}Tc, ^{111}In-labeled leukocytes can be imaged simultaneously with a ^{99m}Tc-labeled bone marrow tracer (dual-isotope scanning) (Palestro *et al*., 2004b).

Protocol

The OM project used an ambitious protocol in which we scanned each pig several times using a combination of scanning techniques (SPECT/CT and PET/CT) and a series of tracers (**Figure 10**). Furthermore, the protocol involved three different institutions. Therefore, it was necessary to apply quite an elaborate setup within a relatively short schedule, taking the pigs' welfare and the attainment of the best tracer sequence into account (Jødal *et al*., 2014, 2016) (**Table 2**). Except in the case of 2-[^{18}F]FDG, the protocol was planned so that each PET/CT scan was performed at least five half-lives after injection of the previous PET tracer. After injection of the ^{68}Ga-labeled tracer (half-life 67.7 min, **Table 2**), the injected activity of 2-[^{18}F]FDG was higher to compensate for the fact that we did not wait 5 × 67.7 min ≈ six hours after the injection of ^{68}Ga-labeled tracer before performing 2-[^{18}F]FDG scanning.

10. An Example of the Scanning Schedule

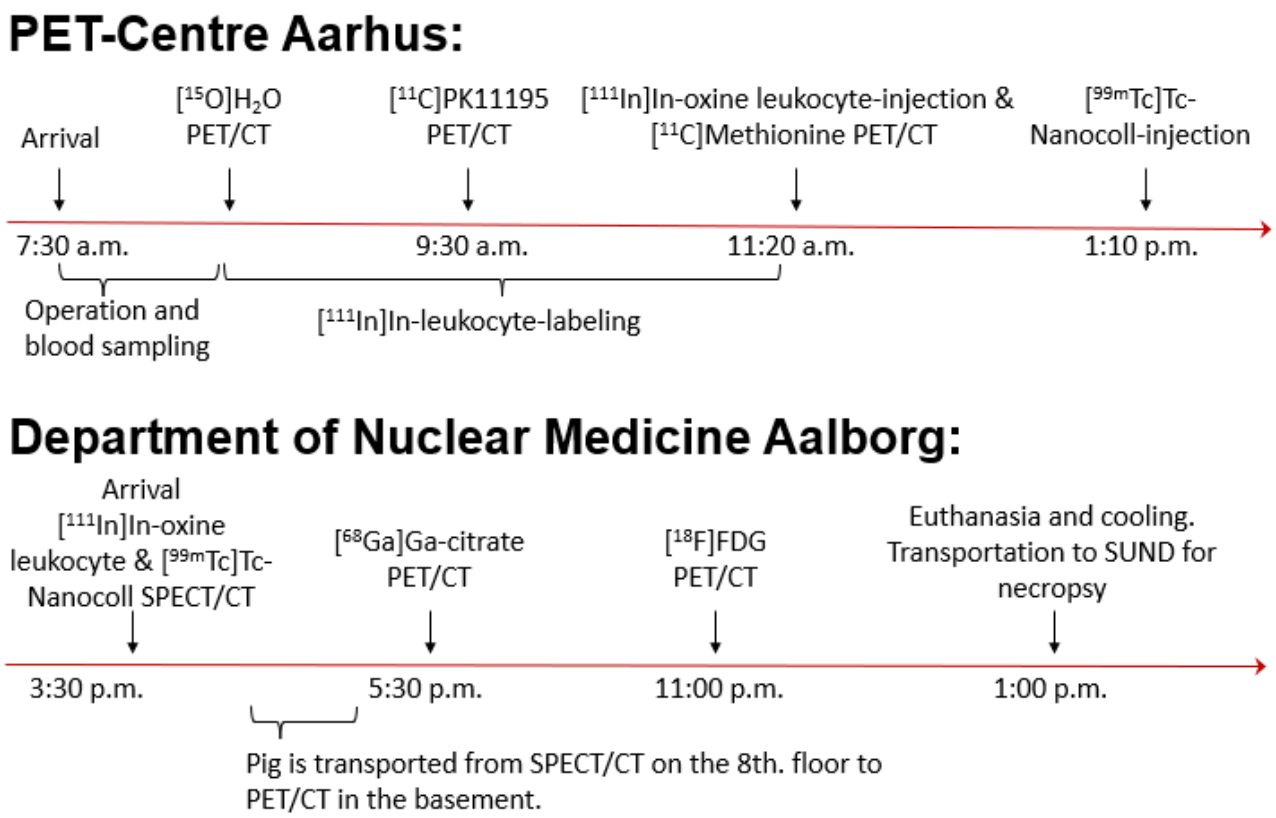

Figure 10. An example of a planned schedule for scans. The protocol was very time-consuming, and we often finished at 4-5 a.m. Later, we performed a 2-[^{18}F]FDG-PET/CT scan the day before conducting examinations of new tracers.

Often, the scans finished at 4 a.m. As unexpected events prolonged the procedures, new tracers were supplied, and in the end, we scanned two pigs per experiment.

Scanning

The pigs were scanned in both Aarhus and Aalborg, all in dorsal recumbency (**Figure 11**). Planar gamma imaging supplied with SPECT/CT was performed in Aalborg on the pelvic limbs and the region included in a single bed position using a Symbia T16 SPECT/CT (Siemens Medical Solutions, Hoffman Estates, Illinois, USA). The residual activity from PET isotopes was recognized as a source of background radiation on the SPECT scanner. Therefore, we applied medium-energy collimators as suggested by Jødal *et al.* 2014. Whole-body planar images were acquired on a dual-headed gamma camera with simultaneous anterior and posterior whole-body acquisition.

We performed an initial scouting view for PET and CT to ensure body coverage from snout to tail. 2-[^{18}F]FDG-PET/CT was performed at either the Department of Nuclear Medicine and PET in Aarhus or the Department of Nuclear Medicine in Aalborg. All L-[*S*-methyl-^{11}C]methionine-PET/CTs were performed in Aarhus. In Aarhus, all examinations were performed using a Siemens Biograph TruePoint™ 64 PET/CT scanner (Siemens Healthineers, Erlangen, Germany).

Reconstruction was performed with four iterations, 21 subsets, and a 3-mm Gaussian postprocessing filter. The voxel size was 2×2×2 mm^3 in a 336×336 matrix. In Aalborg, two different scanners were used because the original scanner was replaced during the project. The first 15 pigs were scanned on a GE VCT Discovery True 64 PET/CT scanner (GE Healthcare, Chicago, Illinois, USA). The reconstruction used two iterations, 28 subsets, and a 6-mm Gaussian filter. The voxel size was 5.5×5.5×3.3 mm^3 in a 128×128 matrix. The last five pigs (nos. 16-20 in Table 1) were scanned on a Siemens Biograph mCT (Siemens, Erlangen, Germany) with time-of-flight (TOF) detection. The reconstruction parameters were three iterations, 21 subsets, and a 3-mm Gaussian filter. The voxel size was 1.02×1.02×2.03 mm^3 in a 400×400 matrix.

Figure 11. Scans Conducted in Aarhus and Aalborg

Figure 11. Pigs during SPECT/CT and PET/CT scans. For PET scans, blood samples were generally drawn every five seconds during the first minute, at 70, 80, 90, 100, 120, 140, 160, 180, 210, 240, 270, and 300 seconds and at 6, 7, 8, 9, 10, 15, 20, 25, 30, 35, 40, 50, and 60 min after injection of the tracer. Blood activity was measured in a NaI(Tl) well counter in a Packard Cobra gamma counter (Aarhus) and Wallac Wizard 2480 (Aalborg) cross-calibrated with the PET camera. We applied an energy window of 450-1200 keV. For metabolite analysis, perchloric acid was added to blood samples, and the supernatants were analyzed by high-performance liquid chromatography.

Although the pigs were anesthetized, we found it necessary to construct a device to ensure the exact positioning of the pigs during scanning to simultaneously enable interpretation of the contralateral limb and control the volume of interest (VOI) for the dynamic scans (**Figure 12**).

Figure 12. Fixation Device

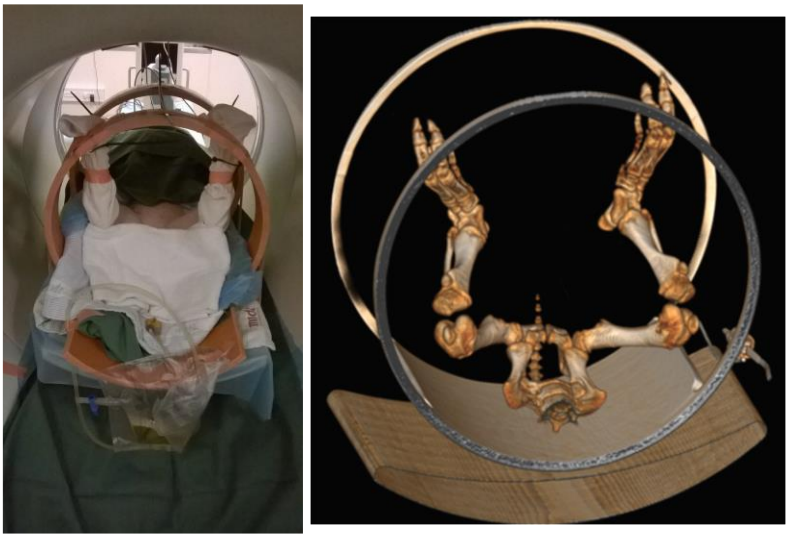

Figure 12. The fixation device facilitated symmetric limb positioning and precluded limb movement during the long scanning sessions.

The use of dynamic (rather than static) PET scans allows kinetic analysis of the results. Dynamic PET gives details on the uptake process and thereby provides more information on the advantages and disadvantages of the studied tracers.

Autopsy and Microbiology

Necropsy was performed according to Madsen *et al.*, 2011. It included mid-sagittal sawing through the bones of the right and left pelvic limbs (femur, femoral head and neck, patella, tibia, calcaneus, talus, tarsus, metatarsus III, metatarsus IV, and phalanges of toes III and IV) and the head (**Figure 13**).

Figure 13. Necropsy

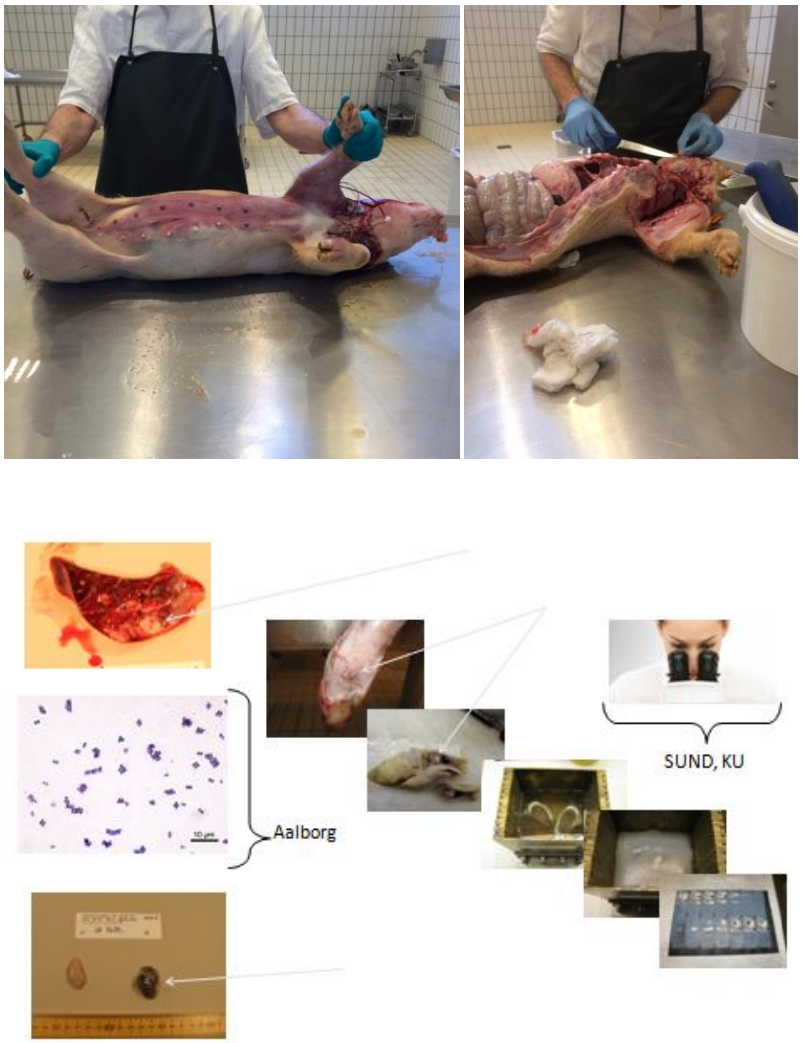

Figure 13. Necropsy of a pig at SUND, Copenhagen University. Samples were collected, and swabs were taken for histopathology and microbiology.

If indicated, for example, by the presence of signs of spread of the infection, mid-sagittal sectioning of the vertebral column, humerus, radius, and ulna was also performed. Necropsy included inspection of the lymph nodes draining the pelvic limbs, i.e., the right and left mammary, subiliac, and medial iliac nodes (**Figure 14**).

Figure 14. Enlarged Lymph Node

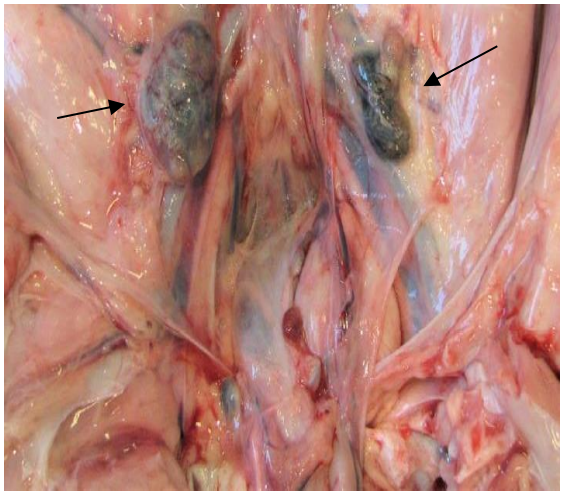

Figure 14. Medial enlarged iliac lymph node on the infected right side (left side of the picture) versus the noninfected smaller lymph node on the left side, pig 4 (**Table 3** page 42**, Paper IX)**.

Predefined tissues and organs were sampled for microbial cultivation, and biopsies were obtained from the lungs and from the distal metaphyseal/physeal interfaces of the right and left femurs. Predefined tissues and organs were selected for histopathology, including right and left medial iliac lymph nodes and bone from the right and left pelvic limbs. Lymph nodes were weighed. Identification of gross lesions at necropsy generally resulted in additional sampling for microbiology and histopathology.

Tissue specimens and swabs obtained at necropsy were smeared on 5% horse blood agar and evaluated after overnight incubation. The presence of *S. aureus* was confirmed, and contaminants were sparse.

RESULTS

Animal Model

After the refinement of the protocol (Aalstrup *et al*., 2016), the incidence of dissemination of *S. aureus* to the lungs decreased from two of three 40-kg pigs (67%) to two of seven 20-kg pigs (29%) (Alstrup *et al.*, 2016). After the extensive *in vivo* interventions were completed on the pigs, their lungs and hearts, but not their brains, were affected. Traditional monitoring parameters cannot always reveal the development and progression of subordinate organ pathology (Alstrup *et al*., 2020b). However, CT imaging can be a valuable addition to classic monitoring parameters. It revealed cardiac and pulmonary problems that needed treatment of some pigs during the transportation from Aarhus to Aalborg (**Figure 15**). We also recognized a case of urine bladder perforation that occurred before the transport of a pig from Aalborg to SUND, KU, as all the urine activity was in the abdomen. Later protocols used CT to alleviate pulmonary problems by positioning the pigs during transportation (**Figure 16)**.

Figure 15. Effects of Long-Term Scans (Heart)

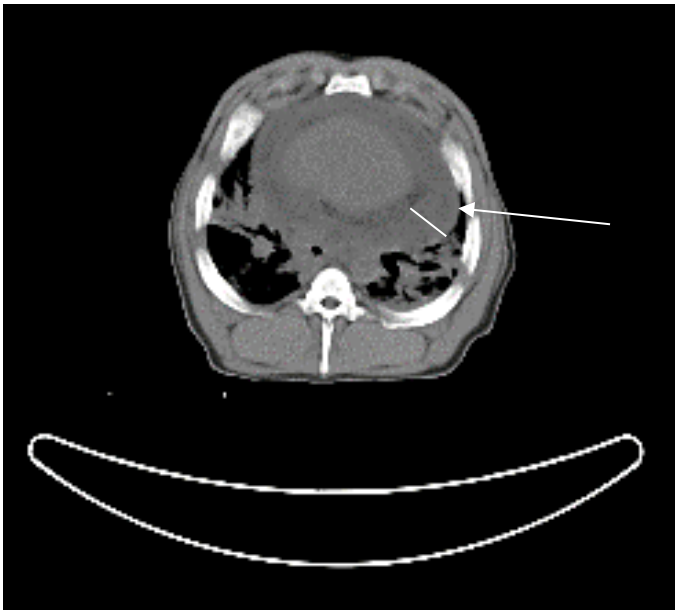

Figure 15 shows pericardial effusion in a pig.

Figure 16. Effects of Long-Term Scans (Lungs)

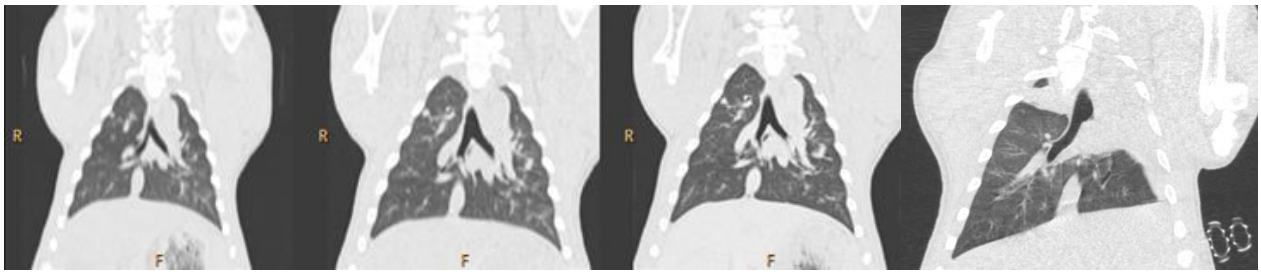

Figure 16. Consecutive CT scans of pig 1 (**Table 3,** page 42) show coronal views of the main bronchi at 0, 2, 4, and 15 hours after the first PET/CT scan. Prolonged anesthesia and transport between two institutions (120 km) and from the 8th floor to the basement at the final destination resulted in occlusion of the left main bronchus and atelectasis of the upper right lung and the dorsal portions of the left lung. At the last location (basement), we manually ventilated the pig as we realized that the standard oxygen supply device in the PET basement was malfunctioning.

In the study of anesthetized Göttingen minipigs (**Paper X**), we examined whether repeated noninvasive scans *per se* affect internal organs and postscan observations. Fourteen of 64 pigs (22%) reached the humane endpoint and were euthanized before scanning was performed, primarily due to limping/apparent limb pain. CT scans did not indicate the presence of significant organ damage in minipigs (n=4) placed in sternal recumbency for a few hours. Upon reviewing the medical records of minipigs positioned in sternal recumbence during PET scans (n=40), it was found that two pigs (5%) had minor complications during the first two weeks after scanning. Minipigs in a dorsal recumbent position that underwent surgical placement of femoral catheters for blood sampling

(n=14) were more frequently associated with minor to moderate postscanning complications (7 cases, 50%). We observed a nonsignificant decrease in body weight when the pigs were placed in a sternal or dorsal recumbent position. The results indicate that anesthetized Göttingen minipigs are slightly affected by the simple short-term scanning procedures and that blood sampling should be reduced when possible. Due to the higher incidence of postscanning complications in minipigs that were catheterized through the femoral artery, postoperative care should be improved. The pigs were not significantly affected by simple short-term scanning procedures without blood sampling and were positioned in the more favorable sternal recumbent position (**Paper X**).

Six pigs (9%) did not develop OM. In each inoculated pig, zero to six OM lesions developed in the growth zones of the long bones (**Figure 17, Paper V**). No OM occurred in the noninoculated hindlimb. In the one-week protocol, the porcine model demonstrated subacute rather than acute OM (**Figure 1, 3, 17**). We attempted to prolong the protocol for two weeks to allow more chronic OM to evolve. However, as described above, only one pig subjected to the two-week protocol was successfully scanned; the other pigs in which this was attempted reached humane endpoints, necessitating euthanasia before two weeks had passed.

Figure 17. Gross Pathology of Osteomyelitis Lesion

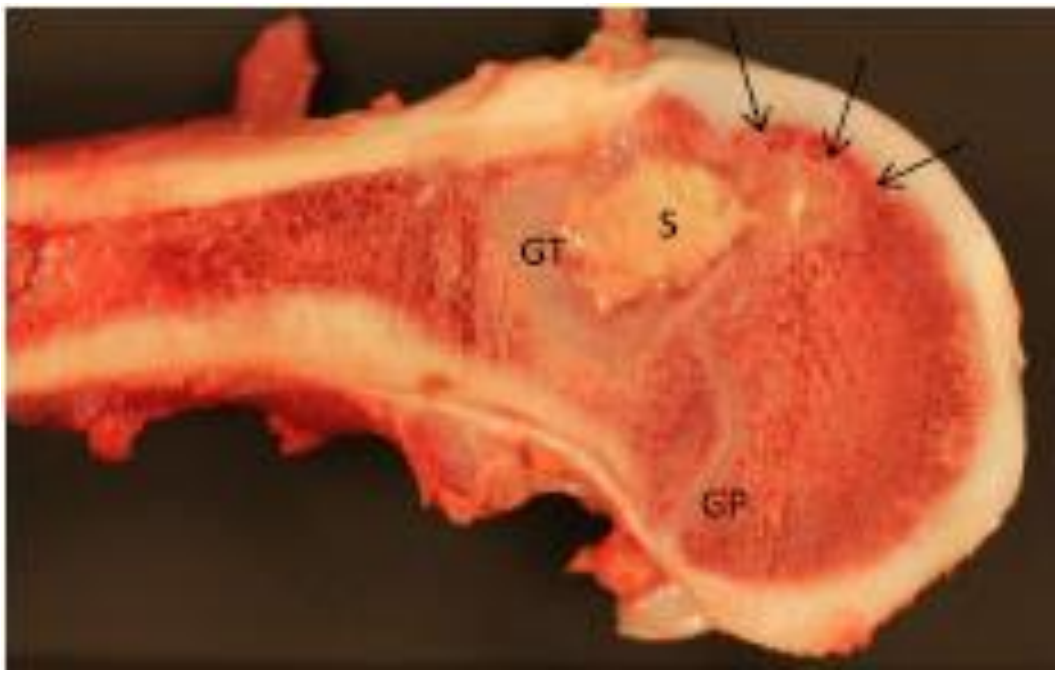

Figure 17. Midsagittal section through the distal femoral bone of the right hindlimb of a pig (OM13, **Table 3**, page 42) infected by inoculation of *S. aureus* into the femoral artery. Pathological chronic, purulent, sequestering OM (S) is seen in the metaphysis, with disruption of the growth plate (GP) and affection of the epiphysis (arrows). The lesion has a size (diameter) of approximately 2 cm. GT: The thick peripheral zone of granulation tissue. (**Paper V**).

CT detected all OM lesions (osteolysis, sequesters, fistulas, and cortical destruction). The lesion size ranged from 0.01 to 4.18 cm^3 (**Paper V**). The subsequent gross pathological analysis identified most lesions and the final histopathology and microbiology analyses confirmed OM.

We found that 52 (approximately 63%) of the lesions in the hindlimb were located in juvenile pigs' femoral, tibial, or fibular bones (**Figure 18**).

Figure 18. Locations of Osteomyelitis Lesions in the Hindlimb

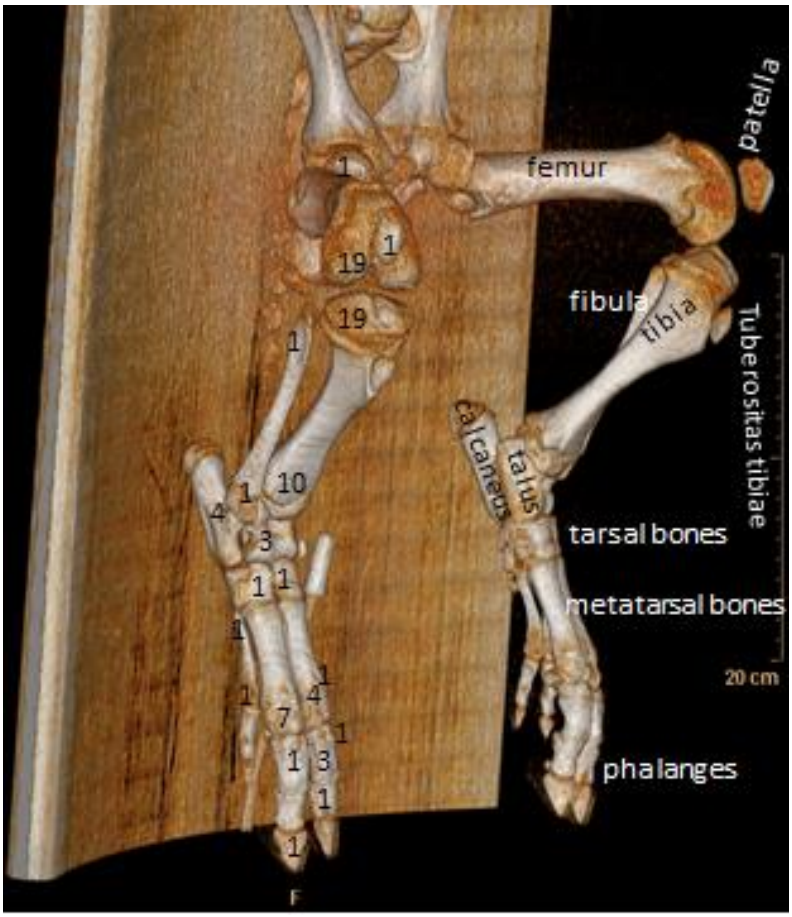

Figure 18. Volume rendering of a CT scan. The number of OM lesions in various anatomical locations in the right hindlimbs of 27 juvenile female pigs (**Table 3**, page 42) inoculated with *S. aureus* was evaluated by CT.

In some pigs, contiguous infections of periosseous tissue and/or abscesses evolved at the inoculation site (**Figure 19**), (**Paper I**).

Figure 19. Peripheral Abscess

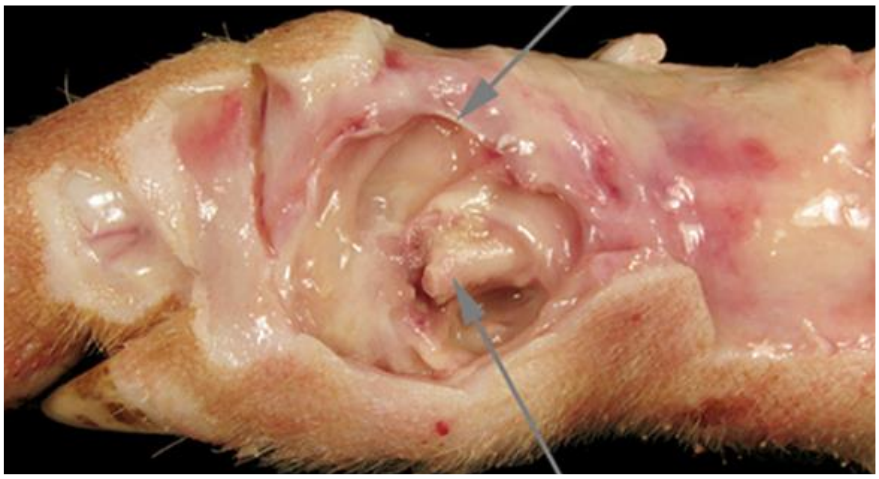

Figure 19. Gross pathology of the right medial foot of pig 2 (**Table 3,** page 42). An abscess was opened (upper arrow), and pus was evacuated, exposing necrotic metatarsus II bone and a pathological fracture along the growth plate in the distal part of the bone (lower arrow) (**Paper I**).

Based on the reading of the CT, 49 of the 56 OM lesions (88%) had formed sequesters, and 44 had developed fistulas (79%). Four lesions (7%) had developed neither sequesters nor fistulas one week after inoculation with *S. aureus* (**Paper V**). In three cases of fistula formation, there were no signs of sequestrum formation on CT. The lesions were, however, tiny (0.01 and 0.02 cm^3). The maximum standardized uptake value (SUV_{max}) was higher when sequesters (p=0.023) and fistulas had formed (p<0.0001) (**Paper V**).

Tracers for Imaging of OM

Table 3 presents the various tracers and pigs in the OM study. Several of the pigs were scanned with up to seven tracers, of which 2-[^{18}F]FDG served as a standard (**Papers I-VII, IX**). CT, microbiology, and histopathology confirmed the presence of OM (**Papers I-VII, IX**). We were unable to perform quantitative histopathology in which we quantitated cellular composition on all of the pigs due to the expense involved. Instead, we conducted a stereological study of lymph nodes in which we examined possible correlations between the accumulation of 2-[^{18}F]FDG and L-[*S*-methyl-^{11}C]methionine and the presence of proliferation and inflammation in the tissue (**Paper IX**).

Table 3. Various Tracers and Individual Pigs Used in the Thesis (Papers I-VII, IX)

Tracers \ Pigs	1	2	3	4	5	6	7	8	9	10	11	12	13	14	15	16	17	18	19	20	21	22	23	24	25	26	27
*PET/CT, very short-lived tracers (**d**ynamic/**s**tatic/**x:** both)*																											
L-[*S*-methyl-^{11}C]methionine	x	x	x	x	x	x	x	x	x	x																	
[^{11}C]PK11195	x	x	s	x																							
[5-^{11}C-methoxy]donepezil					x	x	x	s	x	x																	
[^{15}O]water	x	x	x	x	x	x	x	x	x	x	x		x	x	x												
SPECT/CT (static)																											
[^{111}In]In-oxine-leukocytes	s	s	s	s	s	s	s	s	s																		
[^{99m}Tc]Tc-HSA-nanocolloids	s	s	s	s																							
[^{99m}Tc]Tc-HDP					s																						
[^{99m}Tc]Tc-DPD						s	s		s																		
[^{99m}Tc]Tc-IL-8																		s	s	s	s	s	s	s	s	s	s
PET/CT, other tracers																											
[^{68}Ga]Ga-citrate	x	x	x	x	x																						
[^{68}Ga]Ga-DOTA-Siglec-9						x			x	x													x	x	x	x	x
[^{68}Ga]Ga-DOTA-K-A9											x	x	x	x													
[^{68}Ga]Ga-DOTA-GSGK-A11															x	x	x										
[^{68}Ga]Ga-NOTA-ubiquicidin																		x	x	x		x					
2-[^{18}F]FDG	x	x	x	x	x	x	x		d	x	x		x	x	x	x	x	s	s	s	s	s	s	s	s	s	s
Na[^{18}F]F																		x	x	x		x	s	s			
Stereology																											
O = stereology of OM lesion *l = stereology of lymph node*	l	l		l	l	l	O l	l	l	l																	

Table 3. Overview of tracers used and pigs scanned. Orange: No OM lesions. All reported pigs were studied using multiple tracers (up to seven). 1) The tracers marked with a light gray background are traditional OM tracers. 2-[^{18}F]FDG (**black**, bold type) was used as a standard in all but two of the pigs. Traditional SPECT tracers for OM detection (leukocyte, bone, and bone marrow are shown in maroon. 2) The tracers shown in purple (methionine, PK11195, donepezil, ubiquicidin) are established tracers but nontraditional as OM tracers. 3) OM tracer candidates are shown in olive green. The tracer candidates used in the latter group included a) [^{68}Ga]Ga-citrate produced according to a new protocol developed within the project and thought to bind to bacterial or leukocyte iron-binding proteins; b) [^{68}Ga]Ga-NOTA-Siglec-9 prepared by our Finnish partners and thought to attach to inflammatory endothelium; c) [^{68}Ga]Ga-DOTA-K-A9 and [^{68}Ga]Ga-DOTA-GSGK-A11, peptides developed within the project and selected for study by phage display based on their binding to the bacterial species used in the inoculation; d) [^{99m}Tc]Tc-IL-8, which binds to IL-8 receptors expressed during inflammation from our Dutch partners. Scanning using [^{15}O]water (shown in light blue) revealed perfusion of the lesion and was used for modeling tracer accumulation. We performed qualitative histopathology and microbiology as intended. Quantitative histopathology (e.g., quantitation of cellular composition) was not performed because this was too expensive. Instead, we conducted a stereology study of the animals' lymph nodes to explore possible correlations between the accumulation of 2-[^{18}F]FDG and/or L-[*S*-methyl-^{11}C]methionine and the presence of proliferation and/or inflammation in the tissue (**Paper IX**).

We analyzed the potential infection/inflammation tracers using the compartment model shown in **Figure 20** (right side). This model includes a second tissue compartment, allowing modeling of irreversible tracer uptake, and we generated a Patlak plot of the time-dependent signal to test irreversible tracer uptake. If uptake is irreversible, the Patlak plot will (after equilibrium is reached) be a straight line with a positive slope. The slope of the Patlak plot will be the "irreversible uptake rate" (the net influx rate), Ki, describing the irreversible uptake. The Patlak plot becomes linear when the blood pool and the "reversible" compartment have reached equilibrium. Ki describes

the irreversible uptake from this combined blood/reversible compartment (see **Figure 21)** (Jødal *et al*., 2017a, 2017b).

The plasma measurements of L-[*S*-methyl-^{11}C]methionine and [^{11}C]PK11195 were metabolite-corrected; the other tracers did not show significant metabolism.

Figure 20. Models for Kinetic

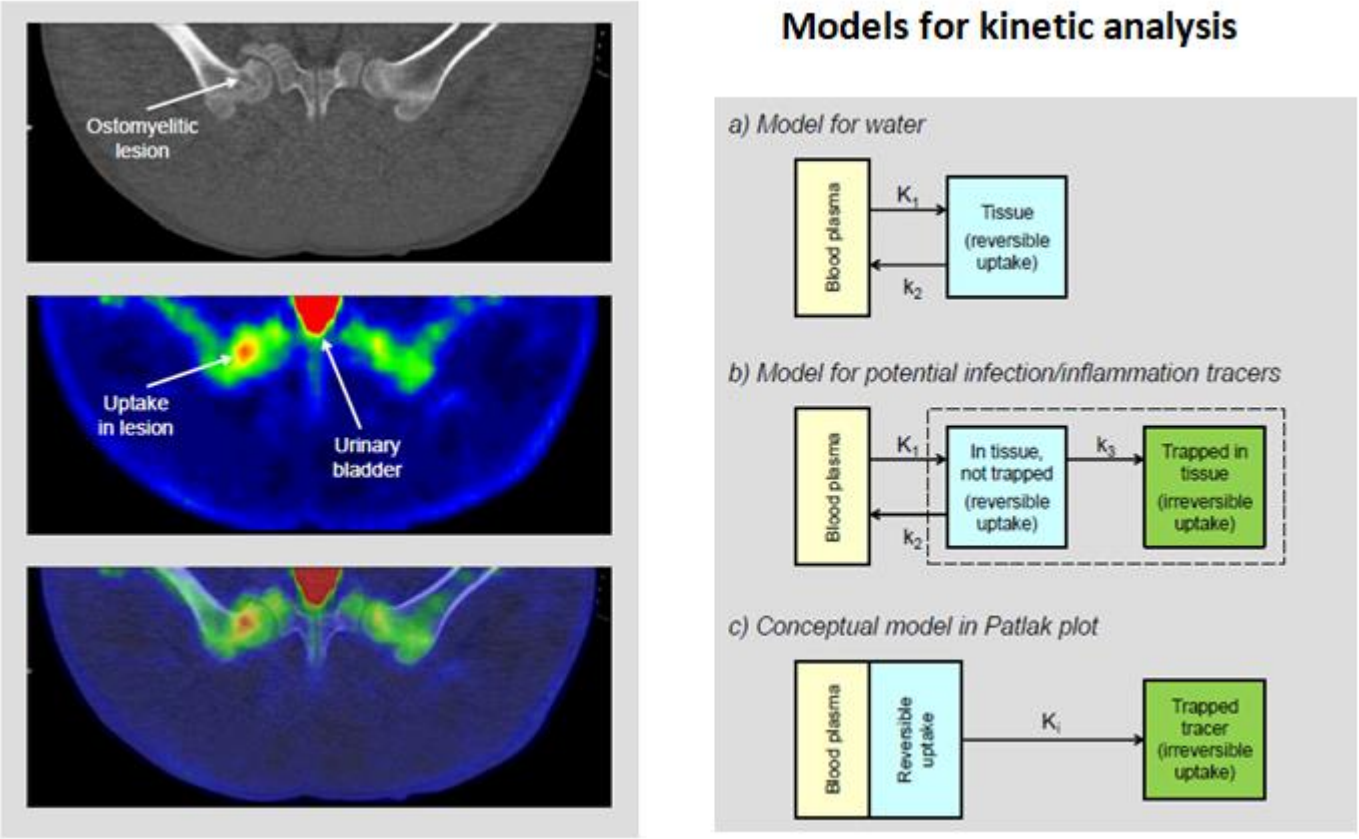

Figure 20. Upper panel: CT scan of pig 1 (**Table 3**) showing OM lesions in the right femoral head/neck. Middle panel: PET scan with 2-[^{18}F]FDG. Lower panel: Fused PET/CT image.

Figure 21. Example of a Patlak Plot

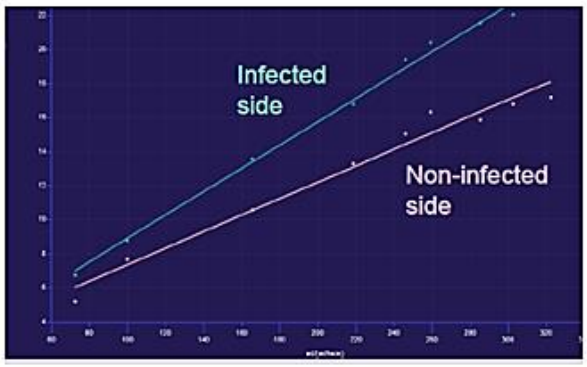

Table I. Model results for water (measure of blood flow)

Lesion	Tracer	K_1		ratio infected/ non-infected
		infected	non-infected	
Femoral head/neck	^{15}O-water	0.30 min^{-1}	0.27 min^{-1}	1,1
Metatarsus II	^{15}O-water	0.10 min^{-}	0.11 min^{-1}	0.9

Table II. Model results for infection/inflammation tracers

Lesion	Tracer	K_i		ratio infected/ non-infected
		infected side	non-infected	
Femoral head/neck	^{11}C-methionine	0.068 min^{-1}	0.048 min^{-1}	1.4
	^{11}C-PK11195	0.54 min^{-1} (*)	0.39 min^{-1} (*)	1.4
	^{68}Ga-citrate	0.008 min^{-1}	0.006 min^{-1}	1.2
	^{18}F-FDG	0.012 min^{-1}	0.006 min^{-1}	2.0
Metatarsus II	^{11}C-methionine	0.078 min^{-1}	0.023 min^{-1}	3.7
	^{11}C-PK11195	0.47 min^{-1} (*)	0.31 min^{-1} (*)	1.6
	^{68}Ga-citrate	0.0059 min^{-1}	0.0016 min^{-1}	3.8
	^{18}F-FDG	0.046 min^{-1}	0.010 min^{-1}	4.9

(*) Plasma curve for PK11195 may be unreliable, which could lead to too high values of K_i while ratio of K_i values would be more stable.

Figure 21. Sample Patlak plot**;** Patlak plot for L-[*S*-methyl-^{11}C]methionine uptake in femoral head/neck lesion in Pig 1 (**Table 3**).

Our results indicate that long bones have a lower perfusion reserve than soft tissues in the presence of infections (Jødal *et al*., 2017a). The studies also showed that the tracers 2-[^{18}F]FDG, [^{68}Ga]Ga-citrate, and [^{11}C]PK11195 are flow-limited, whereas L-[*S*-methyl-^{11}C]methionine is diffusion-limited (Jødal *et al*., 2017b). Evaluation of the kinetics helped establish the optimal scan times for future scans (**Figures 20 and 21**). Table 4 lists the optimal scan time based on our kinetic studies and the actual scan time in the model.

Table 4. Optimal Scan Time (Papers I-VII, IX)

Tracer	Optimal time after injection (minutes)	Actual static scan time (minutes)
PET		
[^{15}O]H_2O	Dynamic	Dynamic
[^{11}C]PK11195	~20*	65
L-[*S*-methyl-^{11}C]methionine	15	63-68
2-[^{18}F]FDG	**60**	**50-94**
[^{68}Ga]Ga-citrate	120	120-133
[5-^{11}C-methoxy]donepezil	30	64-82
[^{68}Ga]Ga-DOTA-K-A9	n.a.y	60-61
[^{68}Ga]Ga-DOTA-GSGK-A11	n.a.y	62
[^{68}Ga]Ga-DOTA-Siglec-9	n.a.y	60-186
Na[^{18}F]F	n.a.y	33-78
[^{68}Ga]Ga-NOTA-ubiquicidin	n.a.y	66-69
Gamma		
[^{99m}Tc]Tc-HDP/MDP	not determined	120-160
[^{99m}Tc]Tc-IL-8	**not determined**	**139-341**
[^{111}In]In-oxine-leukocytes	**not determined**	**330-388**
[^{99m}Tc]Tc-HSA-nanocolloids	not determined	45

n.a.y; not analyzed yet. *van der Laken *et al*., 2008

Figure 22 shows the biodistributions of the various tracers we investigated in the OM project. Table 5 shows the tracers' performances with respect to OM detection and accumulation in infected lymph nodes.

Figure 22. Biodistribution of Tracers

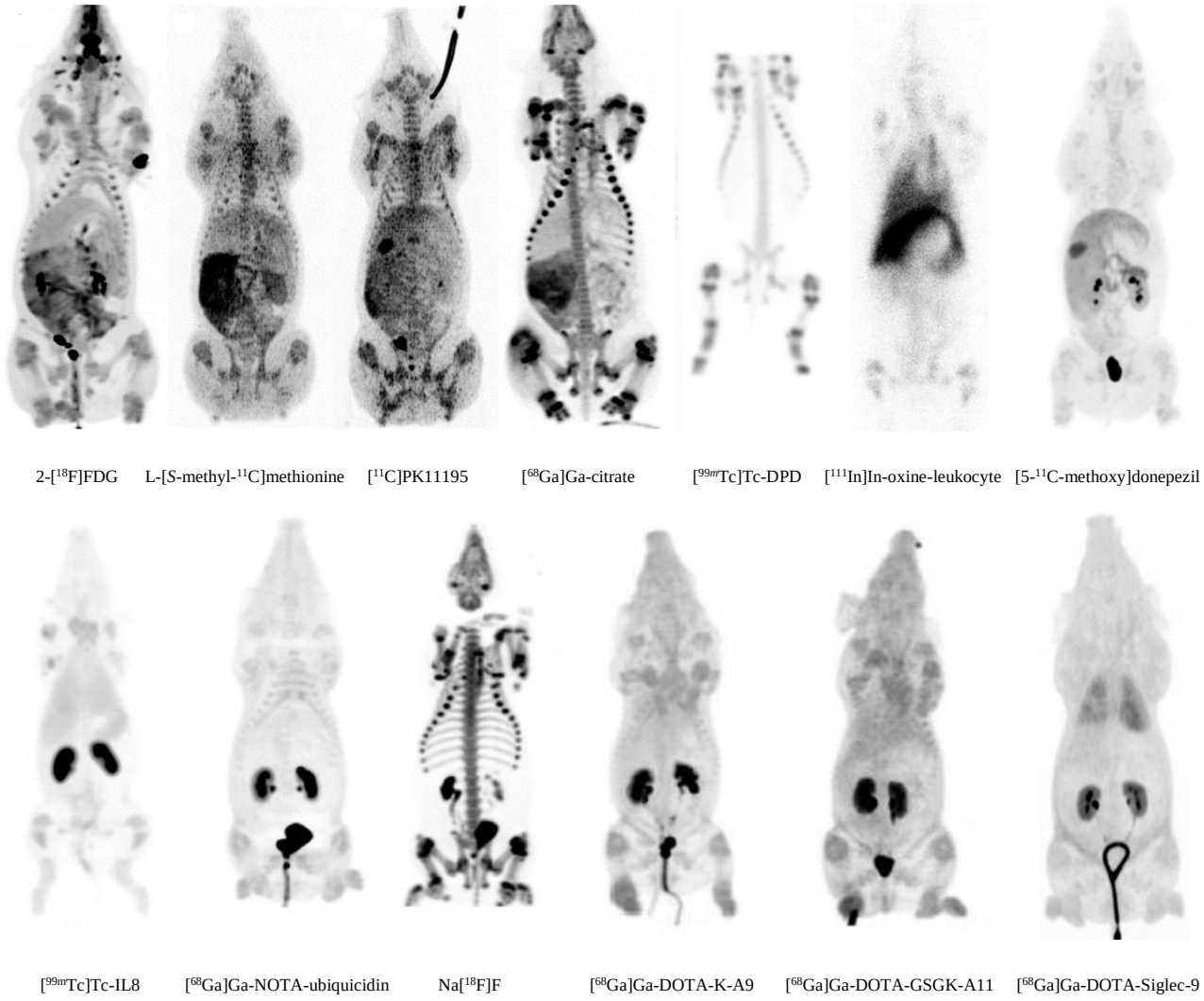

Figure 22. Maximum intensity projection (MIP) of whole bodies from the ventral view showing the distribution of various tracers in juvenile pigs without *S. aureus* infection. 2-[^{18}F]FDG, L-[*S*-methyl-^{11}C]methionine, [^{11}C]PK11195, and [^{68}Ga]Ga-citrate (**Paper II**). [^{99m}Tc]Tc-DPD, [^{111}In]In-oxine-leukocytes, and [5-^{11}C-methoxy]donepezil (**Paper III**). [^{99m}Tc]Tc-IL-8 (**Paper VI**). ^{68}Ga]Ga-NOTA-ubiquicidin, Na[^{18}F]F, [^{68}Ga]Ga-DOTA-K-A9, [^{68}Ga]Ga-DOTA-GSGK-A11, and [^{68}Ga]Ga-DOTA-Siglec-9 (**Paper VII**).

The [^{99m}Tc]Tc-IL8, [^{111}In]In-leukocyte, and [5-^{11}C-methoxy]donepezil tracers had optimal targets for background activity. 2-[^{18}F]FDG and L-[*S*-methyl-^{11}C]methionine also showed uptake in the growth zones, the sites of OM in juveniles.

The biodistribution of L-[*S*-methyl-^{11}C]methionine in juvenile pigs differed from the results reported for pediatric patients undergoing L-[*S*-methyl-^{11}C]methionine studies for malignancies; in human pediatric patients, the pancreas and liver consistently showed the most significant uptake of L-[*S*-methyl-^{11}C]methionine (Harris *et al*., 2013), which was not the case in our studies. However, we did not examine the liver and pancreas until >60 min had elapsed due to the hindlimb region's dynamic examination (which lasted 60 min). Alternatively, this may be a matter of species differences.

Table 5. Performance of Tracers (Papers I-VII)

Tracer	OM	Enlarged iliac lymph node
PET:		
[^{15}O]H_2O	dynamic	dynamic
[^{11}C]PK11195	0%	20%
L-[*S*-methyl-^{11}C]methionine	**79%**	**100%**
2-[^{18}F]FDG	**100%**	**50%**
[^{68}Ga]Ga-citrate	20%	40%
[5-^{11}C-methoxy]donepezil	58%	75%
[^{68}Ga]Ga-DOTA-K-A9	0%	0%
[^{68}Ga]Ga-DOTA-GSGK-A11	0%	0%
[^{68}Ga]Ga-DOTA-Siglec-9	0%	0%
Na[^{18}F]F	0%	0%
[^{68}Ga]Ga-NOTA-ubiquicidin	0%	0%
SPECT:		
[^{99m}Tc]Tc-HDP/-DDP	0%	0%
[^{99m}Tc]Tc-IL-8	**70% (92%)**	**0%**
[^{111}In]In-oxine-leukocytes	**79%**	**38%**

Percentages of OM and of enlarged reactive iliac lymph nodes (as a fraction of the total number of reactive iliac lymph nodes) detected by tracers.

[^{15}O]H_2O (Flow)

^{15}O-water was quickly distributed in the left femur, but its distribution was blocked in the infected limb when the cortex of the bones was intact (**Figure 23**). However, in cases in which fistulous tracts had formed, the [^{15}O]water passed freely. In both cases, the blood flow was slightly higher (~1.5-fold) in the region with OM in the infected limb and ~sixfold higher in soft tissues compared to the left limb (Jødal *et al*., 2017a).

Figure 23. [^{15}O]H_2O Distribution after Direct Injection into the Bone Marrow next to an OM Lesion

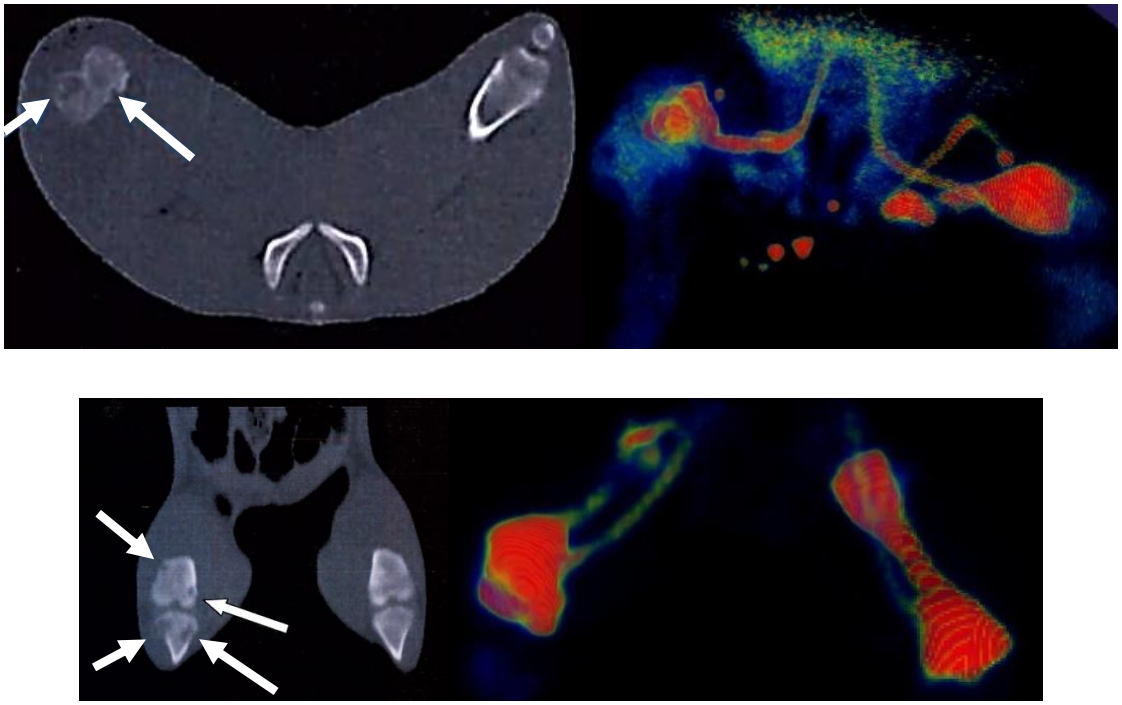

Figure 23. Left, upper panel: CT of OM lesions in the lateral epicondyle and at the growth plate in the distal right femur of pig (OM31, not yet published). Right, upper panel: MIP showing the distribution of [^{15}O]H_2O (mean activity (45 sec - 5 min)) after injection of 200 MBq directly into the bone next to an OM lesion and in the same location on the left side. Left, lower panel: CT of OM lesions in the medial epicondyle and at the distal lateral right femoral corpus and the lateral and medial tibial bone of pig (OM26, not yet published). Right, lower panel: MIP showing the distribution of [^{15}O]H_2O (mean activity (45 sec - 5 min)) after injection of 200 MBq directly into the bone next to an OM lesion and in the same location on the left side.

[^{11}C]PK11195 (Immune Response, Steroid Synthesis, and Apoptosis):

After venous injection of [^{11}C]-PK11195, high amounts of radioactivity were found in the gall bladder, pyloric antrum/duodenum, urinary bladder, and small intestine, and less activity was found in other regions such as bone, liver, kidney, and thymus; there was slight accumulation in the lungs and in muscle tissue **(Figure 22)**. The tracer did not accumulate significantly in OM lesions on static scans (0%) and detected only 20% of infected iliac lymph nodes (**Table 5**).

*L-[S-*methyl-*^{11}C]Methionine (Protein Synthesis)*

Analysis of the biodistribution of L-[*S*-methyl-^{11}C]methionine showed high uptake in the pancreas but lower uptake in the liver and increased accumulation in the small intestine (**Figure 22**). Compared to the examination reported in Harris *et al.* 2013, our static images were obtained much later after injection because we performed the dynamic scans first (**Table 4**).

L-[*S*-methyl-^{11}C]methionine proved to be a sensitive tracer for detecting OM (~79%) (**Table 5**), and it was even better for detecting lymph nodes as draining *S. aureus*-infected foci

accumulated more L-[*S*-methyl-^{11}C]methionine than did control nodes (100%) (**Table 5, Figure 24 and 25**). This was better than the performance of 2-[^{18}F]FDG (50%) (**Table 5, Figure 24, Paper III**). L-[*S*-methyl-^{11}C]methionine accumulation in the OM lesions presented a regional appearance, as the tracer tended to accumulate in the deep portions of the lesions (**Paper III**). This finding could be related to local variations in the inflammatory process (formation of granulation tissue or new bone) and to perfusion.

Figure 24. Tracer Uptake in Infectious Lesions

	Total number	L-[*S*-methyl-^{11}C]methionine	[5-^{11}C-methoxy]donepezil	[^{99m}Tc]Tc-DPD	[^{111}In]In-oxine-leukocytes	2-[^{18}F]-FDG
Osteomyelitis	24	19/24	14/24	0/24	19/24	18/18
Periosseos abscess	4	4/4	4/4	0/4	4/4	3/3
Inoculation hematoma	2	0	0	0	0	0
Lymph node enlargement	8	8/8	6/8	0/8	3/8	3/6

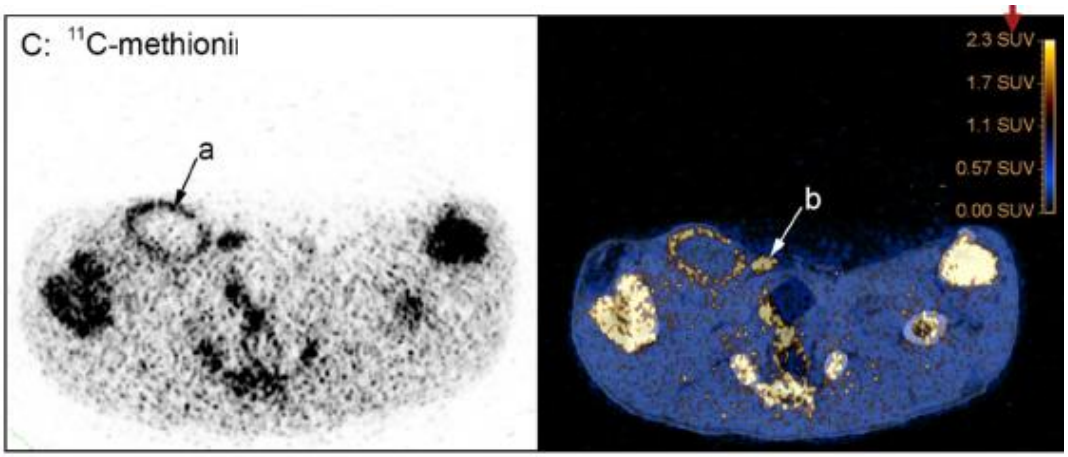

Figure 24. Five pigs (pigs 6-10, **Table 3**) were scanned, and 24 OM lesions and eight enlarged lymph nodes were found (**Paper III**). In pig 2, an enlarged right iliac lymph node (b) with increased L-[*S*-methyl-^{11}C]methionine uptake and an abscess (a) in the inoculation site with increased L-[*S*-methyl-^{11}C]methionine uptake in the abscess wall were found (**Paper I**). PET (left image) and fused PET/CT (right image).

An example of L-[*S*-methyl-^{11}C]methionine accumulation in the right popliteal lymph node is shown in **Figure 25**.

Figure 25. L-[*S*-methyl-^{11}C]Methionine Accumulation in a Popliteal Lymph Node

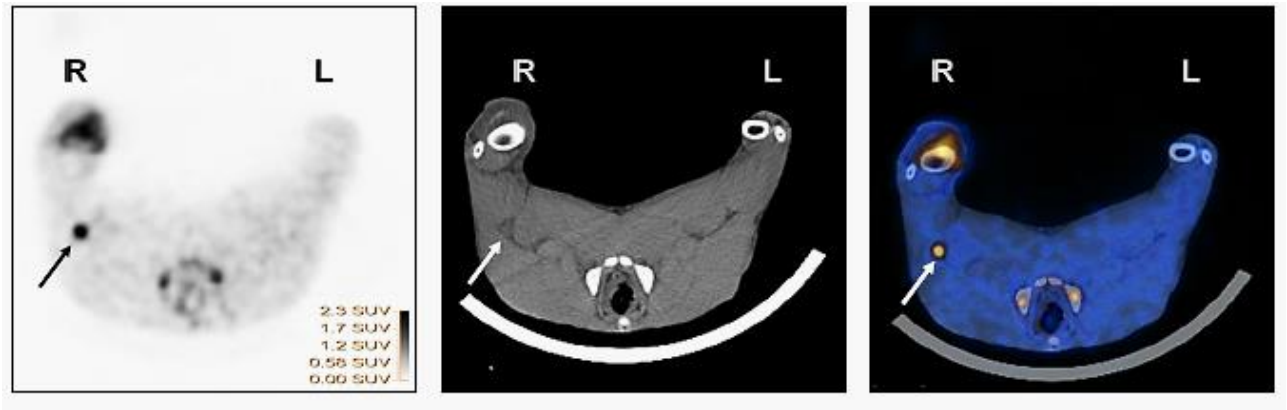

L-[*S*-methyl-^{11}C]methionine-PET **CT** **L-[*S*-methyl-^{11}C]methionine-PET/CT**

Figure 25. PET, CT, and fused PET/CT images of the pelvic limbs of pig 10 (**Table 3**). Arrow: The right popliteal lymph node was increased in size and showed L-[*S*-methyl-^{11}C]methionine accumulation. The right proximal tibial bone contained an OM lesion (**Paper IX**).

We determined the *in vivo* SUVs of 2-[^{18}F]FDG and L-[*S*-methyl-^{11}C]methionine in lymph nodes, and we correlated these values with the area fractions of three different cell-associated antigens identified by immunohistochemistry (IHC) (**Paper IX)**. We chose the proliferation marker Ki-67 (clone MIB1) (Ezzelarab *et al*., 2014) as a measure of the overall proliferation stage of the lymph nodes, the marker L1 (clone MAC387) (Sarli *et al.*, 2001; Soerensen *et al*., 2012) to detect the accumulation of macrophages, granulocytes, and monocytes in lymph nodes, and the activation marker IL-8 (clone 8M6) (Soerensen *et al*., 2012; Lauersen, 2014) to detect any cells, preferentially activated neutrophils and macrophages, expressing the cytokine (**Figure 26, Paper IX**).

Figure 26. Area Fractions

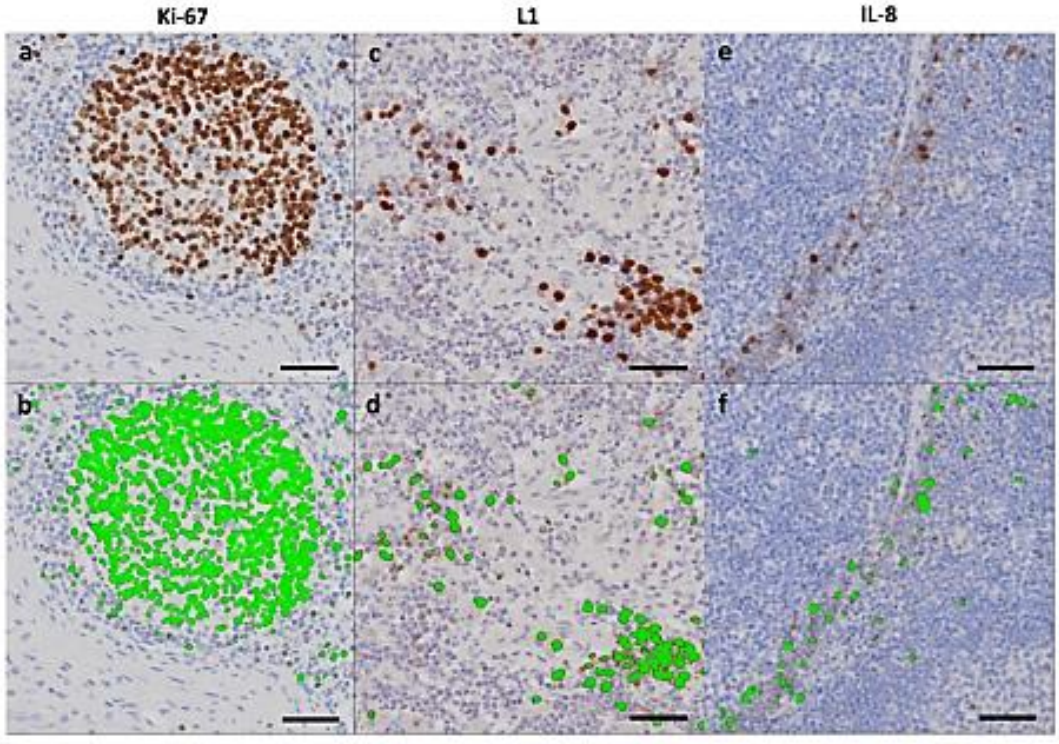

Figure 26. Area fractions. Lymph nodes from the nine 2-[^{18}F]FDG and L-[*S*-methyl-^{11}C]methionine PET/CT-scanned pigs (pigs 1-2 and 4-10) were cut into 3-4 mm slabs and embedded in paraffin. Sections (3-5 µm) were prepared for IHC of Ki-67 (clone MIB1), L1 (clone MAC387), and IL-8 (clone 8M6). IHC-stained lymph node tissue identifying Ki-67- (pig 3), L1- (pig 2), and IL-8-positive cells (pig 5) as indicated (a, c, e) and corresponding automatic threshold identification of positive cells with subsequent green labeling of the cells using Visiopharm Image Analysis Software (b, d, f) are shown. Scale bar = 50 µm (**Paper IX**)

We found that the weights of the animals' mammary and medial iliac lymph nodes and their SUV_{FDGmax} values showed a significant increase in the inoculated right hind limb compared to the left hind limb. Popliteal lymph node weight and FDG uptake did not differ significantly in the two hindlimbs.

The area fractions of Ki-67 and IL-8 in the right mammary lymph nodes and SUV_{Metmax} in the right popliteal lymph nodes were significantly increased compared with the left (control) side and concluded that the PET tracers 2-[^{18}F]FDG and L-[*S*-methyl-^{11}C]methionine and the IHC markers Ki-67 and IL-8, but not L1, showed increased values in lymph nodes draining soft tissues infected with *S. aureus*. Ki-67 and IL-8 may be reliable markers of the lymph node response to *S. aureus* infection. Increased L-[*S*-methyl-^{11}C]methionine accumulation may indicate a more acute lymph node response, whereas increased 2-[^{18}F]FDG accumulation may indicate a more chronic response.

2-[^{18}F]FDG (glucose metabolism)

The lesion size ranged from 0.01 to 4.18 cm^3, but all lesions accumulated 2-[^{18}F]FDG-PET (**Paper V**). A volume of 0.01 cm^3 appears to be the approximate limit for CT evaluation, and the FDG accumulation facilitated the interpretation. The results demonstrate that for OM diagnostics, it is possible to reduce the injected activity of a radiotracer even more, given that even small lesions are visible after injection of an amount of activity as low as 0.19 MBq/kg body weight (0.005 mCi/kg) (**Figure 27** and **28, Paper V**).

Figure 27. 2-[^{18}F]FDG Activity in a Large Osteomyelitis Lesion

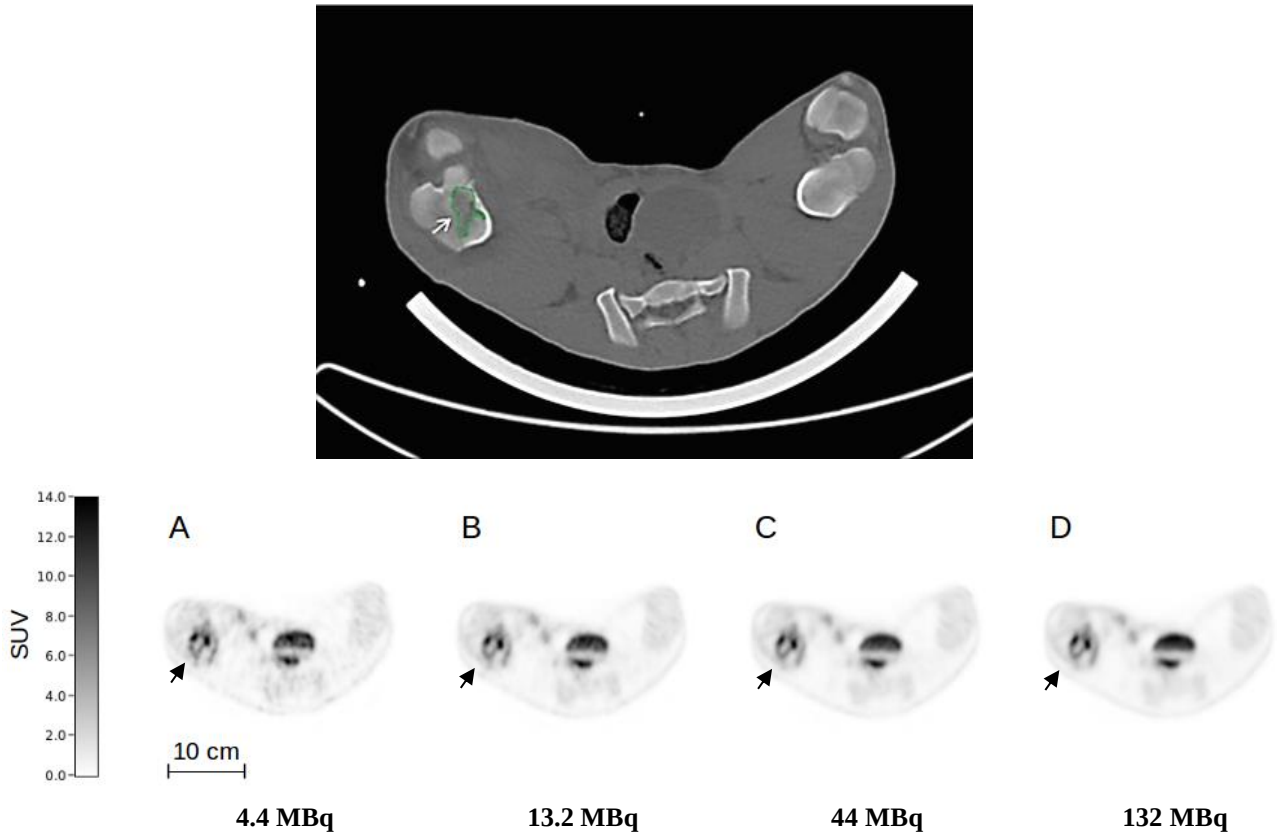

Figure 27. Above: CT scan (bone window) of the more significant medial, irregular (1.52 cm^3) OM lesion in the right distal femur of pig 17 (indicated by the arrow) (**Table 3**). The original SUV_{max} on Philips EBW was 8.0 g/mL. Below: Increasing activities of 2-[^{18}F]FDG in the OM lesion in the right distal femur (indicated by arrows): 4.4 MBq (A), 13.2 MBq (B), 44 MBq (C), and 132 MBq (D) simulated injected activity (**Paper V**).

Figure 28. 2-[^{18}F]FDG Activity in a Small Osteomyelitis Lesion

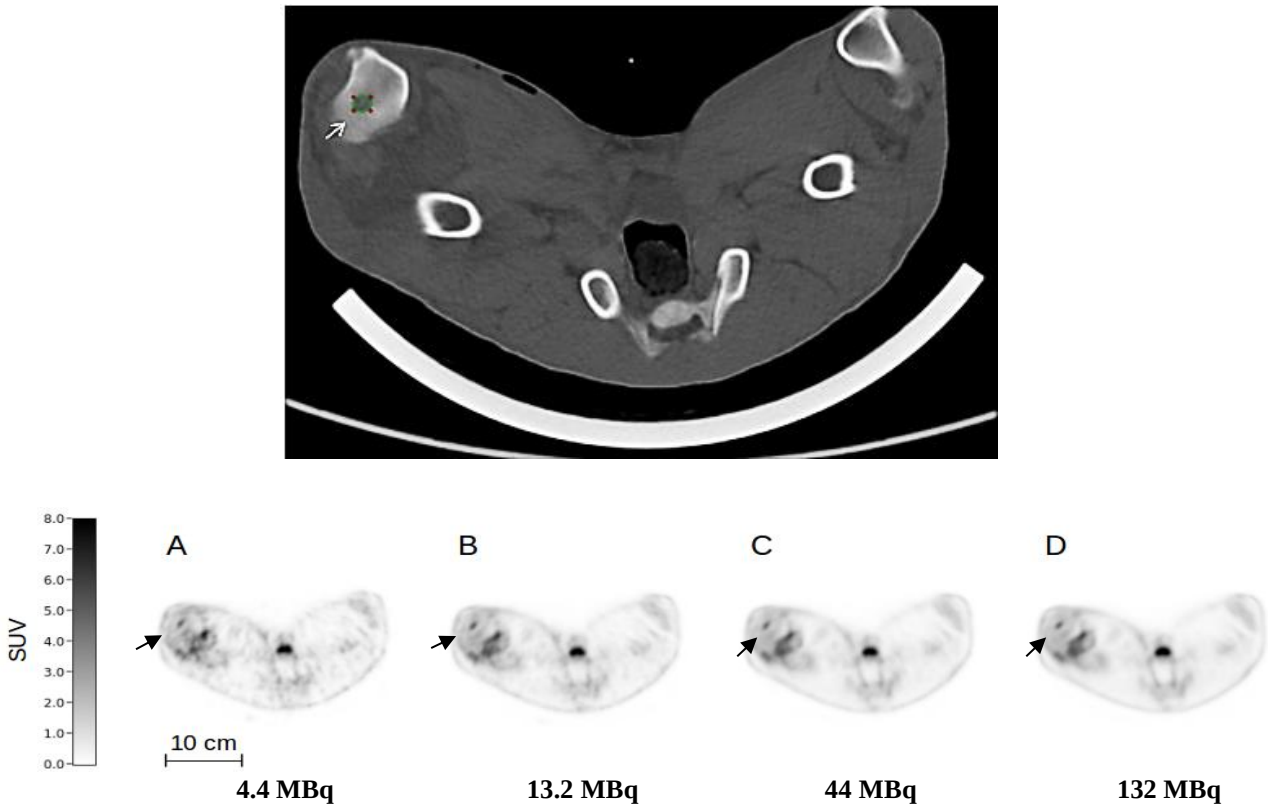

Figure 28. Above: CT scan (bone window) of a minor (0.21 cm^3) OM lesion (osteolysis) in the right proximal tibia of pig 18 (indicated by the arrow) (**Table 3**). Below: Increasing activities of 2-[^{18}F]FDG in the OM lesion of the right proximal tibia (indicated by arrows): 4.4 MBq (A), 13.2 MBq (B), 44 MBq (C), and 132 MBq (D) simulated injected activity (**Paper V**).

[^{68}Ga]Ga-Citrate (de novo Synthesis)

The difference between infected and noninfected sites appeared to be greater in soft tissue (nonOM) than in bone (OM) lesions. [^{68}Ga]Ga-citrate was not helpful for imaging OM (**Table 5**, **Paper II**). Its uptake was slow and diffusion-limited. Therefore, we suggest imaging at 120 min after injection as the best compromise between allowing sufficient time for uptake and performing imaging before ^{68}Ga has decayed to the point where imaging is no longer possible (**Figure 29**, **Paper II**).

Figure 29. Tracer Accumulation in a Neck Abscess and Histopathology

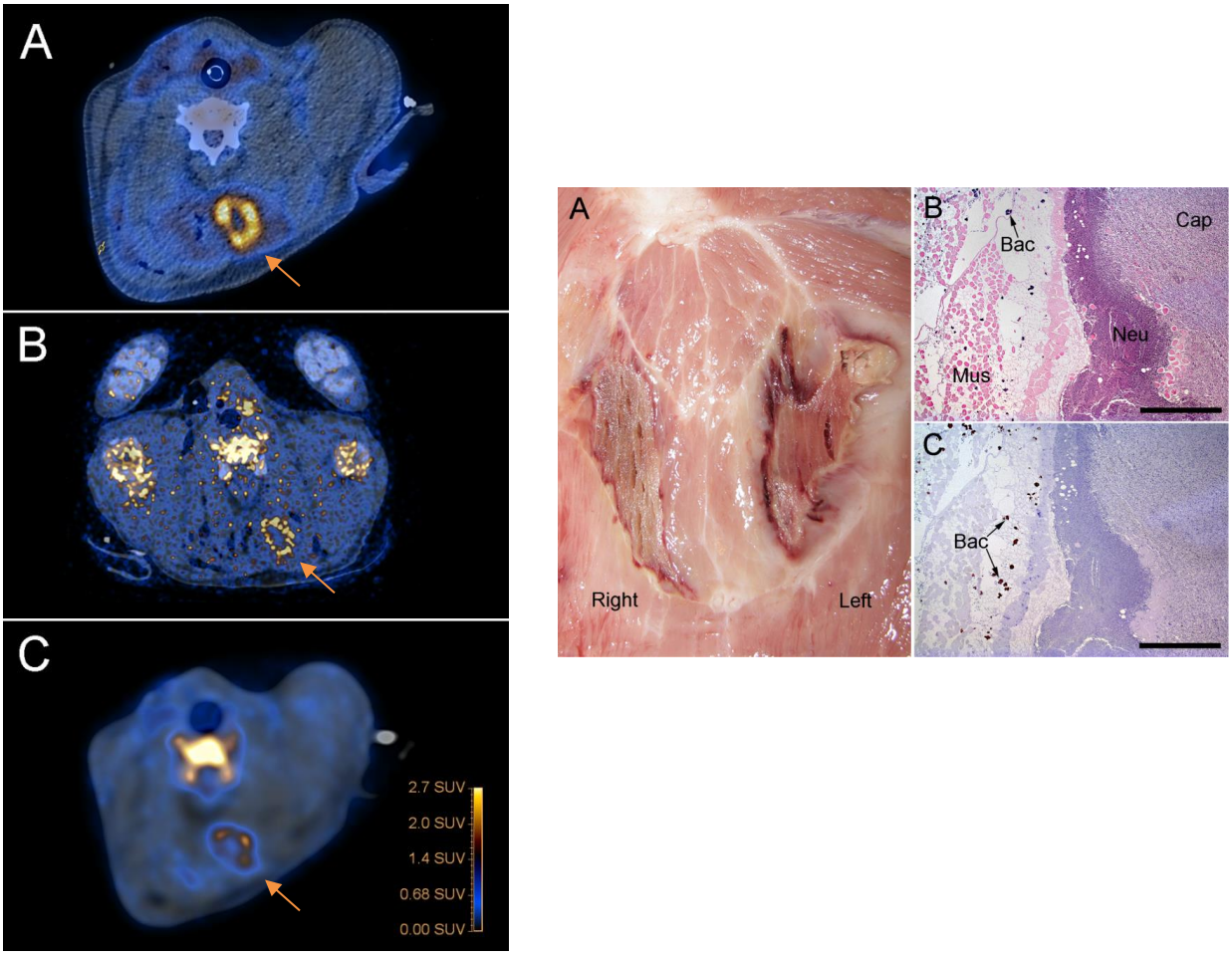

Figure 29. Left panel: Fused PET/CT images showing axial views of pig 1 (**Table 3**) after injection of 2-[^{18}F]FDG (**A**), L-[*S*-methyl-^{11}C]methionine (**B**), and [^{68}Ga]Ga-citrate (**C**). (**A**) and (**C**) have been aligned to (**B**) so that the cervical vertebrae are in the same plane; the neck region with muscle necroses is shown. The left muscle exhibited *S. aureus* infection and peripheral suppuration (orange arrow). High tracer uptake in the lesion within the left muscle. Only a faint uptake of 2-[^{18}F]FDG, but no uptake of the other two compounds, was observed in the margin of the necrotic areas within the right muscle. Right panel: Gross pathology of skeletal muscle necrosis in the neck region (**A**). The lesion in the left muscle had peripheral suppuration. The histopathology of a skeletal muscle lesion consisting of necrosis and peripheral suppuration (left-sided lesion in **A**) is shown. (**B**, **C**). Hematoxylin and eosin staining demonstrate capsule formation (Cap) consisting of granulation tissue, neutrophils (Neu), and necrotic transversely sectioned striated muscle cells (Mus) and bacterial colonies (Bac) (**B**). The same region showed immunohistocytochemical staining demonstrating the presence of *S. aureus* bacteria (Bac) (**C**). Bars (**B**, **C**) = 1 mm (**Paper II**).

[5-^{11}C-methoxy]Donepezil (Signaling)

Evaluation of blood samples and dynamic PET data from the same project indicated that more rapid metabolism of [5-^{11}C-methoxy]donepezil occurs in pigs than in humans. The analyses were complicated because a significant metabolic product included the ^{11}C atom (and was thus visible on the PET scans) and had an affinity for the same receptors as donepezil (Jødal *et al.*, 2017b). [5-

^{11}C-methoxy]donepezil was not helpful for imaging OM, detecting only 58% of lesions, but it appeared better for the detection of affected lymph nodes (75%) (**Table 5**, **Paper III)**. The uptake of [5-^{11}C-methoxy]donepezil in OM seemed to depend more on perfusion (flow-limited) than on differences between infected and noninfected tissues (Jødal *et al*., 2017b).

[^{68}Ga]Ga-DOTA-K-A9 and [^{68}Ga]Ga-GSGK-A11 (S. aureus biofilm)

We observed no increased tracer activity of the two *S. aureus* phage-displayed selected peptides, [^{68}Ga]Ga-DOTA-K-A9 (**Figure 30**) and [^{68}Ga]Ga-DOTA-GSGK-A11 (**Figure 30**), in porcine OM lesions (**Table 5**, **Paper VII**). **Figure 22** shows the biodistribution of the peptides in pigs. The liver and kidneys excreted both peptides.

Figure 30. Accumulation of [^{68}Ga]Ga-DOTA-K-A9 and [^{68}Ga]Ga-DOTA-GSGK-A11 in Osteomyelitis Lesions compared to 2-[^{18}F]FDG

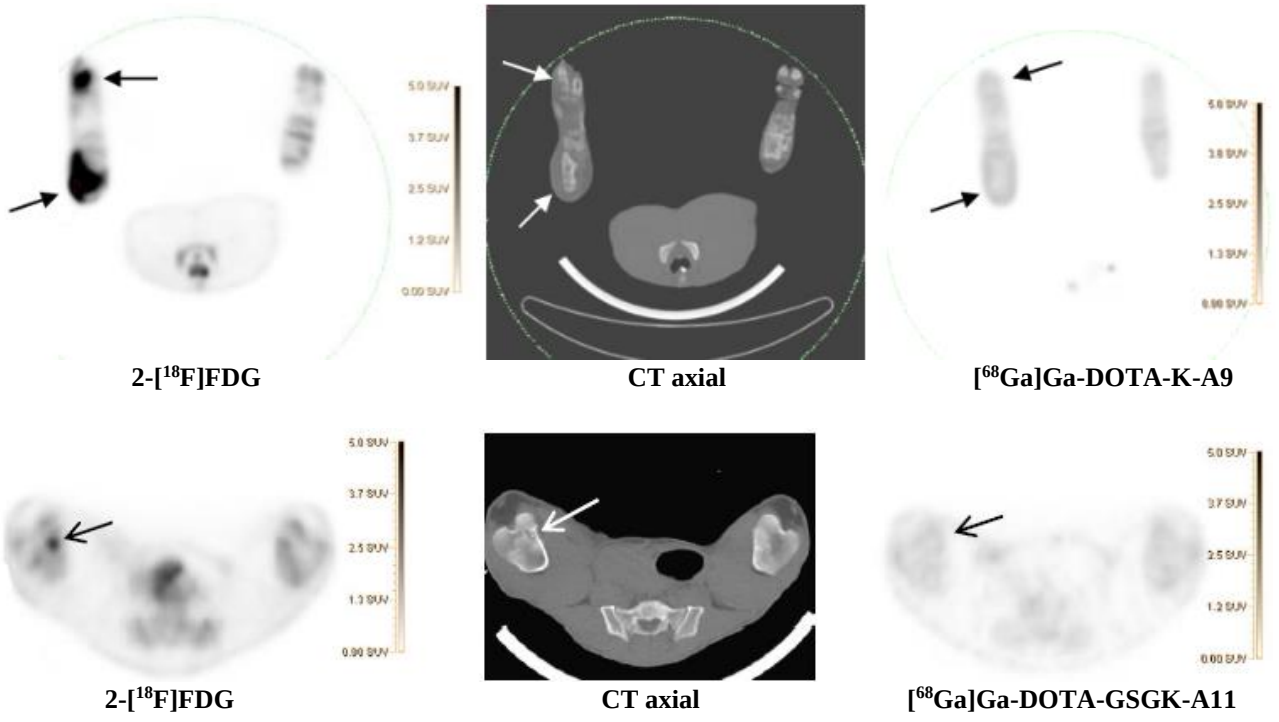

Figure 30. Uptake of [^{68}Ga]Ga-DOTA-K-A9 in the right calcaneus and distal II metatarsus of pig 11 (**Table 3**) and of [^{68}Ga]Ga-DOTA-GSGK-A11 in the right distal femur of pig 16 (**Table 3**) compared to 2-[^{18}F]FDG in OM lesions and corresponding CT in axial views (**Paper VII**).

Dynamic scans (not published yet) showed diffuse, low uptake by the tissue along the right hindlimb (data not shown). The OM location in the calcaneus is shown in **Figure 30**. The left picture in **Figure 31** shows uptake into the marrow (not specifically a focus) of the right femur (shown

in dark pink) and the left femur (shown in light pink). There was no difference between the two legs, and there was no sign of the tracer being attached. The right picture shows uptake in soft tissue at the calcaneus; there is higher uptake on the right side (shown in orange-brown) than on the left side (shown in green). Nevertheless, it does not attach, so the curves may only indicate that more blood passes through the infected hindlimb than the noninfected left limb. The general picture is that the tracer elements are primarily not attached, and only the bladder produces a strong signal. The kidneys were not in the field of view surveyed in the dynamic scans.

Figure 31. Dynamic Scans of OM [^{68}Ga]Ga-DOTA-K-A9

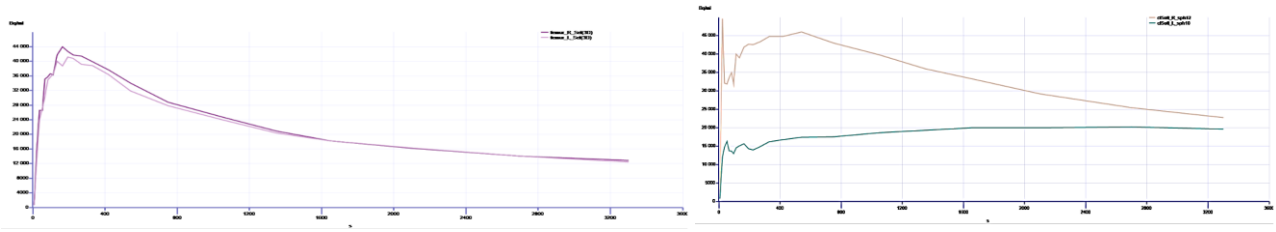

Figure 31. Screenshots of graphs prepared using Carimas software from Turku. Dynamic scans of [^{68}Ga]Ga-DOTA-K-A9 in the femur and calcaneus of the noninfected and infected hindlimbs of pig 11 (**Table 3**) are shown. The panel on the left shows the right femur (dark pink) and the left femur (light pink). The panel on the right shows the right calcaneus (orange-brown) and the left calcaneus (green).

Figure 32. Dynamic Scans of OM 2-[^{18}F]FDG and [^{68}Ga]Ga-DOTA-GSGK-A11

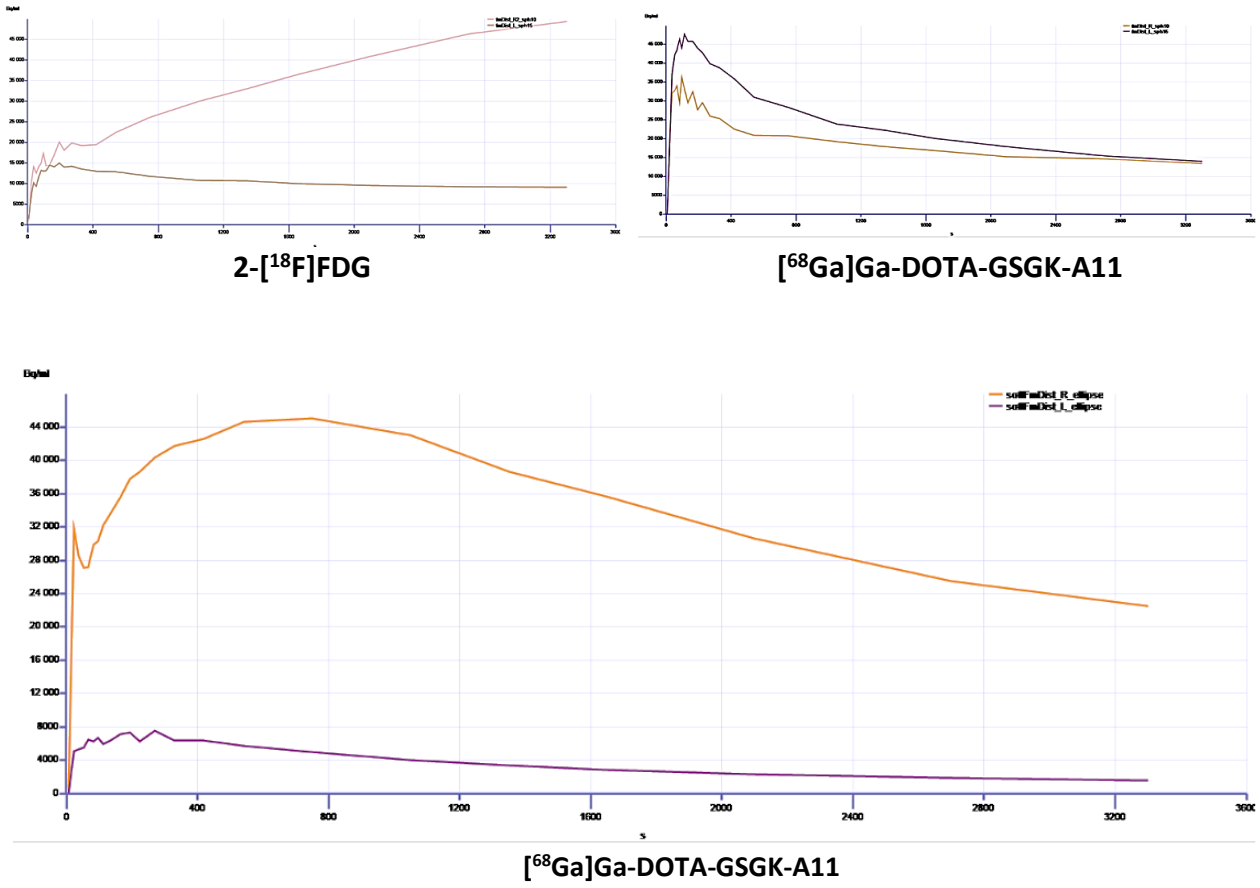

Figure 32. Screenshots of graphs prepared using Carimas software from Turku. Upper panel: Dynamic scans showing 2-[^{18}F]FDG and [^{68}Ga]Ga-DOTA-GSGK-A11 in OM of the distal femur of the noninfected and infected hindlimbs of pig 17 (**Table 3**). The upper panel on the left (shows the right femur (shown in red) and the left femur (shown in brown). The upper panel on the right shows the right femur (shown in dark color) and the left femur (shown in orange-brown). Lower panel: Dynamic scans showing [^{68}Ga]Ga-DOTA-GSGK-A11 in the knee of the noninfected hindlimb (shown in dark pink) and in the knee of the infected hindlimb (shown in orange).

[^{68}Ga]Ga-DOTA-GSGK-A11 was also disappointing compared to 2-[^{18}F]FDG (**Figure 32**, upper right). There was no difference between the two legs, and there was no sign of the tracer being attached. The lower panel shows uptake in soft tissue at the knee; there is higher uptake on the right side (shown in orange) than on the left side (shown in dark pink). Nevertheless, it does not attach, so the curves may only indicate that more blood passes through the infected hindlimb than the noninfected left limb.

[^{68}Ga]Ga-DOTA-Siglec-9 (leukocyte trafficking)

We observed no tracer activity in early or late images obtained using [^{68}Ga]Ga-DOTA-Siglec-9 (**Table 5**, **Figure 33**, **Paper VII**). Nevertheless, the tracer accumulated in infectious foci in

the dorsocaudal parts of both lungs, and we noted a general tendency for [^{68}Ga]Ga-DOTA-Siglec-9 to accumulate in these parts (**Figure 34**). We also observed this in pigs that did not develop OM or pulmonary infections.

Figure 33. 2-[^{18}F]FDG and [^{68}Ga]Ga-DOTA-Siglec-9 Accumulation in Osteomyelitis Lesions

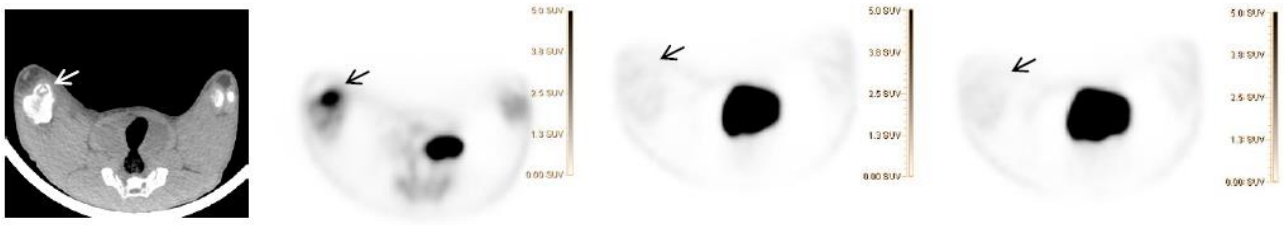

CT axial **2-[^{18}F]FDG** **Early** **Late** **[^{68}Ga]Ga-DOTA-Siglec-9**

Figure 33. 2-[^{18}F]FDG and [^{68}Ga]Ga-DOTA-Siglec-9 (early and late acquisition; 1 and 2 h) uptake in an OM lesion in the right medial condyle of the right distal femur (indicated by an arrow) and the corresponding CT (axial view) of pig 6 (**Table 3, Paper VII**).

A CT image (axial view) of the dorsocaudal parts of the lungs of a pig with signs of infection and partial atelectasis (arrow) and the [^{68}Ga]Ga-DOTA-Siglec-9 uptake in the corresponding anatomical area of the animal are shown in **Figure 34**. Axial views of CT and PET and a MIP (side view) of [^{68}Ga]Ga-DOTA-Siglec-9 distribution in the pig's body are shown. The SUV scale bar is shown in the axial PET image (**Figure 34**, **Paper VII**)

Figure 34. [^{68}Ga]Ga-DOTA-Siglec-9 Accumulation in the Lungs

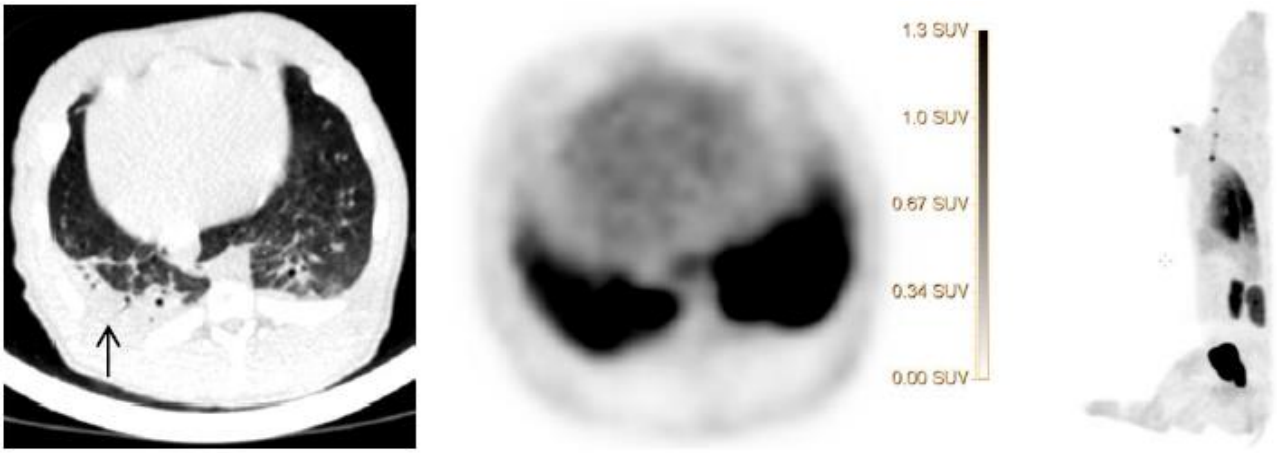

CT axial view **[^{68}Ga]Ga-DOTA-Siglec-9** **PET MIP side view**

Figure 34. [^{68}Ga]Ga-DOTA-Siglec-9 uptake in the lungs of pig 23 (**Table 3**). Left: CT scan axial view. Middle: PET scan axial view. Right: Maximal intensity projection (MIP) side view (**Paper VII**).

Figure 35 demonstrates, in images acquired 10-30 min after tracer injection, marked [^{68}Ga]Ga-DOTA-Siglec-9 uptake in the margin of an inguinal abscess (indicated by a solid arrow) adjacent to the *S. aureus* inoculation site. In static images acquired after 60 min, the activity of [^{68}Ga]Ga-DOTA-Siglec-9 decreased, whereas 2-[^{18}F]FDG activity in the margin of the abscess increased slightly (**Figure 35**, **Paper VII**). Note the similar uptake of [^{68}Ga]Ga-DOTA-Siglec-9 in the growth zones of the distal femur and proximal tibia and the intense uptake of 2-[^{18}F]FDG in the OM lesions of these bones (with sequestrum and fistula formation) in the right hindlimb. A hyperplastic medial iliac lymph node on the right side (indicated by a broken arrow) displayed increased 2-[^{18}F]FDG uptake compared to the lymph node in the noninfected left hindlimb. The second image in **Figure 35** was acquired 60 min after injection of the tracers. At that time, the activity of [^{68}Ga]Ga-DOTA-Siglec-9 in the abscess had decreased, whereas that of 2-[^{18}F]FDG had increased (**Paper VII**).

Figure 35. [^{68}Ga]Ga-DOTA-Siglec-9 and 2-[^{18}F]FDG Accumulation in an Abscess

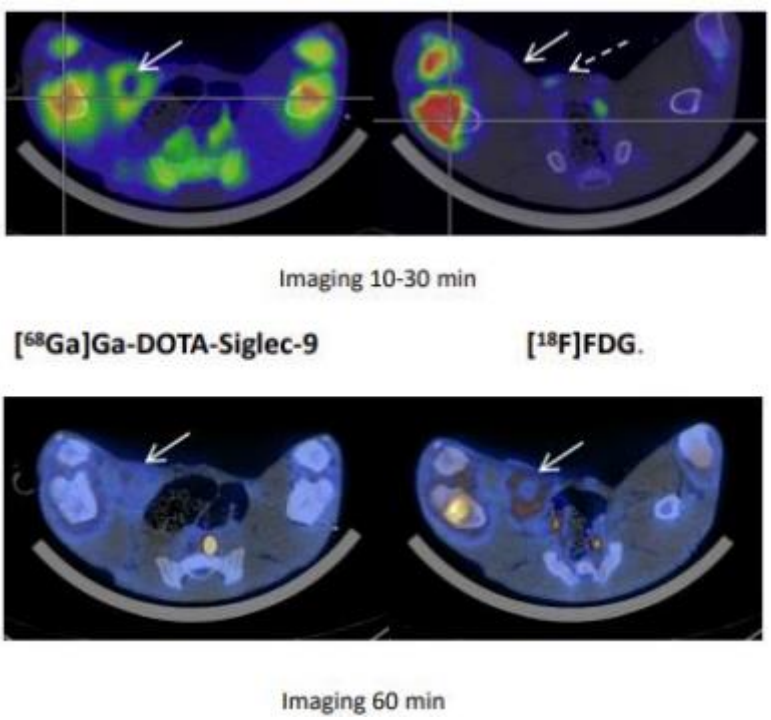

Figure 35. Upper panel: [^{68}Ga]Ga-DOTA-Siglec-9 uptake by a 5×3×2 cm chronic abscess (solid arrow) in the right inguinal region 10-30 min after tracer injection; the image is an average of the frames covering the period 10-30 min, simulating a static image and uptake of 2-[^{18}F]FDG in the same region in pig 23 (**Table 3, Paper VII**). The broken arrow marks the medial iliac lymph node. Lower panel: Fused static images were acquired 60 min after injection of the tracers.

[^{68}Ga]Ga-NOTA-ubiquicidin (bacterial cell membranes)

We observed no accumulation of [^{68}Ga]Ga-NOTA-ubiquicidin in OM lesions (**Figure 36, Table 5**). [^{68}Ga]Ga-NOTA-ubiquicidin was excreted by the kidneys (**Figure 22**).

Figure 36. [^{68}Ga]Ga-NOTA-Ubiquicidin, Na[^{18}F]F, and 2-[^{18}F]FDG Accumulation in Osteomyelitis Lesions

CT axial view **2-[^{18}F]FDG** **[^{68}Ga]Ga-NOTA-ubiquicidin** **Na[^{18}F]F** **Na[^{18}F]F scale 0-20 SUV**

Figure 36. Uptake of [^{68}Ga]Ga-NOTA-ubiquicidin and Na[^{18}F]F compared to [^{18}F]FDG in OM lesions in the proximal tibial bone of pig 18 (**Table 3**). Corresponding CT in axial view to the left (**Paper VII**).

[^{99m}Tc]Tc-HDP/DDP and Na[^{18}F]F (bone remodeling)

The biodistribution of the bone tracer [^{99m}Tc]Tc-HDP/DDP was similar in juvenile pigs and children (**Figure 37**). The figure shows intense tracer uptake in the physis secondary to osteoblastic activity in the growth zones of long bones in both children and juvenile pigs. We observed no tracer uptake in OM in young pigs. The same was true for Na[^{18}F]F (**Figure 22**). To some extent, the high physiological uptake in the physis due to osteoblast activity during growth requires careful comparison with the location in the noninfected limb, as OMs tend to occur in that location (**Figure 36, 37, Paper III**).

Figure 37. Bone Scintigraphy of a Child and a Juvenile Pig

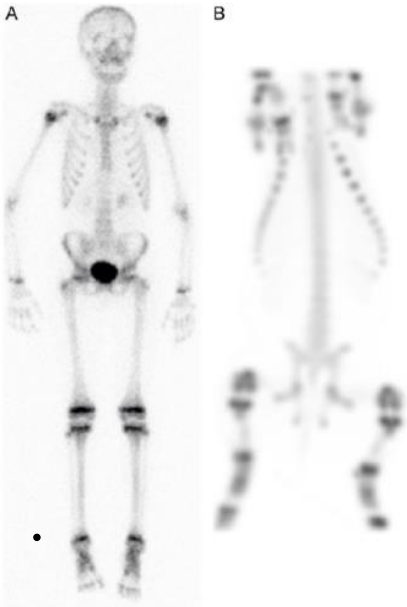

Figure 37 Whole-body-[^{99m}Tc]Tc-DPD bone scintigraphy of A: 7-year-old child (anterior view); B: 12-week-old pig without OM (ventral view MIP) (**Paper III**).

[^{99m}Tc]Tc-IL-8 (chemokine)

[^{99m}Tc]Tc-IL-8 was easily and relatively quickly prepared. Imaging was possible two hours after injection of the tracer. Even though there was a diffuse physiological accumulation of the tracer in the epiphyses/metaphyses of the long bones in pigs, it was possible to differentiate between normal diffuse physiological uptake and increased focal and pathological uptake of [^{99m}Tc]Tc-IL-8 in OM lesions in similar locations (**Figure 38**, **Paper VI**). [^{99m}Tc]Tc-IL-8 revealed 70% of OM lesions in peripheral bones compared to a 100% sensitivity of 2-[^{18}F]FDG (**Table 5**, **Paper VI**). However, [^{99m}Tc]Tc-IL-8 performed even better when scanning was delayed (revealed 4 of 10 lesions (40%) at 139-150 min) versus 12 of 13 lesions (92%) at 239-341 min) (**Paper VI**, data not shown).

Figure 38. 2-[^{18}F]FDG and [^{99m}Tc]Tc-IL-8 Accumulation in Osteomyelitis Lesions and CT and Histopathology of an Osteomyelitis Lesion

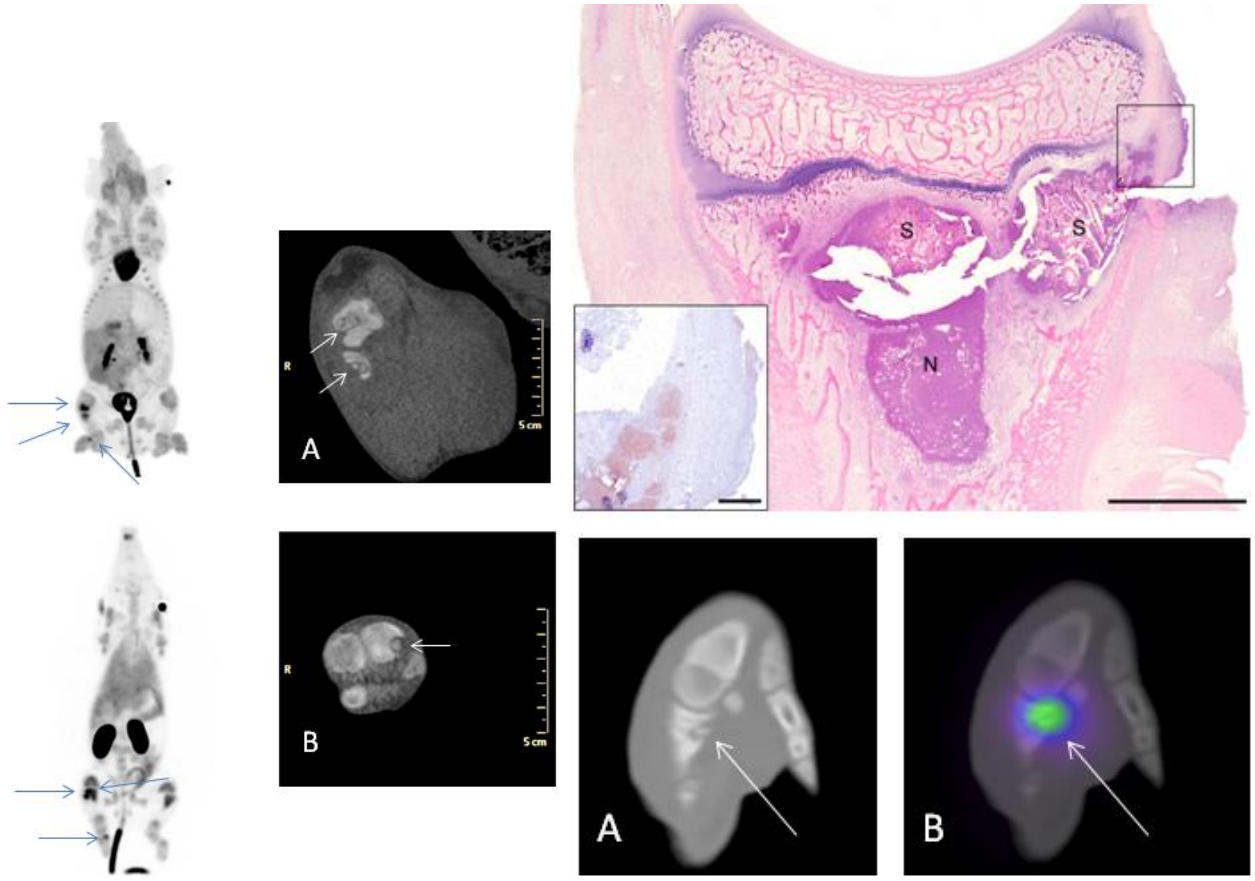

Figure 38. Left: 2-[^{18}F]FDG (maximal intensity projection (MIP), upper) and [^{99m}Tc]Tc-IL-8 uptake (MIP, lower) in pig 21 (**Table 3**), in which there were three OM lesions in the right hindlimb (indicated by arrows). Middle: A: CT (bone window): OM in the proximal tibia and fibula and B: OM in the third metatarsal bone. All OMs formed sequesters and fistulous tracts. The lesions are marked with arrows. A size scale (5 cm) is shown on the right of the CT images. Right: Histopathology of a mid-sagittal section of the right proximal phalanx from toe IV of pig 26 (**Table 3**) is shown. OM is seen in the metaphysis distal to the growth plate, and the infection penetrates the cortical bone. Sequesters (S) and neutrophils (N) form an intramedullary abscess close to the growth plate. Scale bar, 4.5 mm. Hematoxylin and eosin stain. IHC staining for IL-8 corresponds to the inserted framed area, showing prominent locations of positive cells, primarily neutrophils. Scale bar, 0.54 mm. Below are a CT scan (A) and fusion images obtained by IL8 scintigraphy and CT (B) of the same lesion indicated by arrows (**Paper VI**).

[^{99m}Tc]Tc-IL8 accumulated in the lungs (**Figure 39**, **Paper VI**). However, the infectious foci in the lungs were distinguishable from physiological activity in abscesses at the site of inoculation, and the [^{99m}Tc]Tc-IL8 tracer performed well. IHC showed the presence of IL-8-producing neutrophils and a higher degree of exudation in the periphery of the OM lesion. Sequestra occupy the space in the center of the OM, preventing the accumulation of neutrophils.

Figure 39. Biodistribution of [^{99m}Tc]Tc-IL-8 and 2-[^{18}F]FDG and [^{99m}Tc]Tc-IL-8 Accumulation in the Lungs

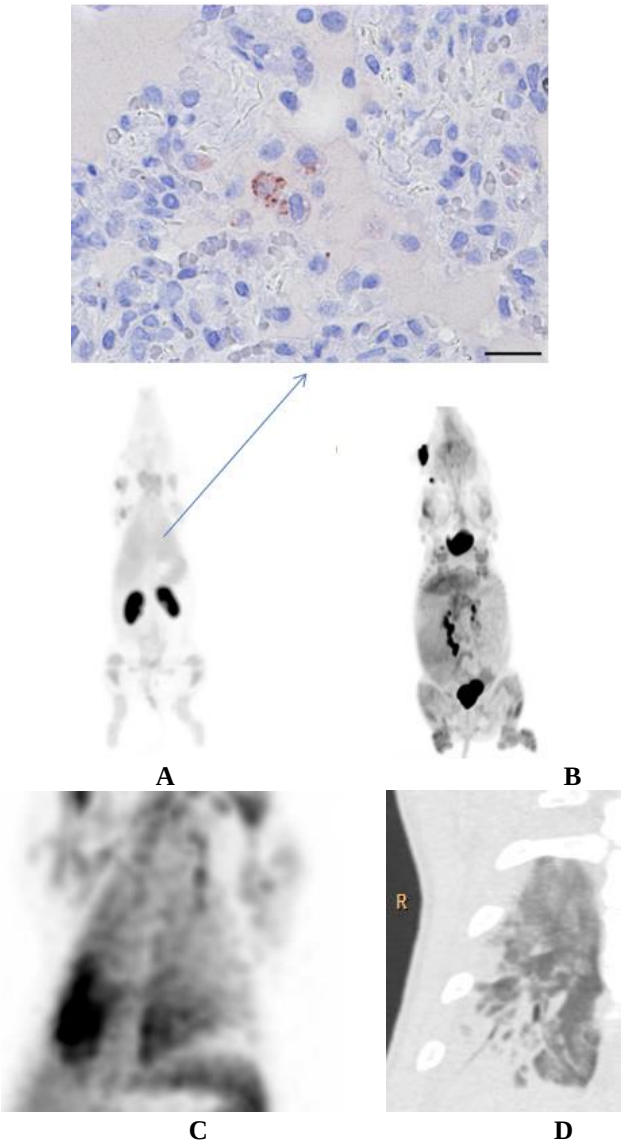

Figure 39. MIPs (ventral views) are showing the biodistribution of [^{99m}Tc]Tc-IL8 (A) and 2-[^{18}F]FDG (B) in pig 25 (**Table 3**) without OM or pneumonia. Immunohistochemical staining for IL-8 in the lung (scale bar: 25 µm). There was detectable IL-8 inside the lung parenchyma and close to macrophages (IHC stain for IL-8). Below, the figure shows [^{99m}Tc]Tc-IL-8 uptake in pig 19 (**Table 3**), also without OM (C), and in the atelectasis and edematous changes in the left caudal lung without pneumonia. (D): CT of the right lung. IHC staining for IL-8 showed no detectable IL-8 in the lung parenchyma (not shown). R: Right side (**Paper VI**).

[^{111}In]In-oxine-Leukocytes (Leukocyte Homing)

[^{111}In]In-oxine-leukocytes detected 79% of OM but few infected lymph nodes (38%) (**Table 5, Paper III)**. The main difference in leukocyte distribution between humans and pigs is the

persistent accumulation of leukocytes in porcine lungs, whereas, under normal circumstances, such accumulation is a transient phenomenon in human lungs (**Figure 40**, **Papers III-IV**).

Figure 40. Whole Body [^{111}In]In-oxine-Leukocyte Scintigraphy of an Adult Human and a Juvenile Pig

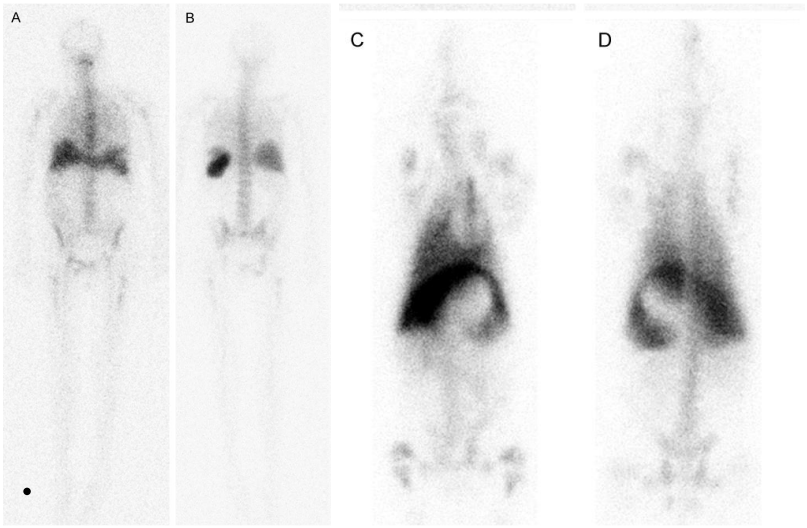

Figure 40. Whole-body [^{111}In]In-oxine-leukocyte scintigraphy of an adult human 24 hours after inoculation with [^{111}In]In-leukocytes (A: anterior view; B: posterior view) and of a 12-week-old juvenile pig without OM 6 hours after inoculation (C: ventral view; D: dorsal view). The central sparing in the pig between the liver and spleen represents a full stomach. As in humans, prolonged clearance of labeled leukocytes from the liver and spleen is seen, as is low excretion of the labeled cells in feces and urine. The significant difference between humans and pigs was the accumulation of activity in the lungs of juvenile pigs; such accumulation is only a transient phenomenon in healthy human lungs (**Paper III**).

For animal ethics, we also decided to examine the pigs that were planned to be euthanized before examinations of tracers in another study (**Paper IV**, **Figure 41**). We demonstrate that it is possible to perform SPECT/CT with ^{111}In-labeled autologous leukocytes almost 24 hours after euthanasia and achieve the same detectability of OM lesions as in living pigs (78% versus 79%) (**Paper IV**). The pigs that had been euthanized were maintained under the same experimental conditions as the living pigs. They were examined in parallel with the living pigs, except they were euthanized before the leukocyte scan.

Figure 41. Postmortem [^{111}In]In-oxine-Leukocyte SPECT and CT

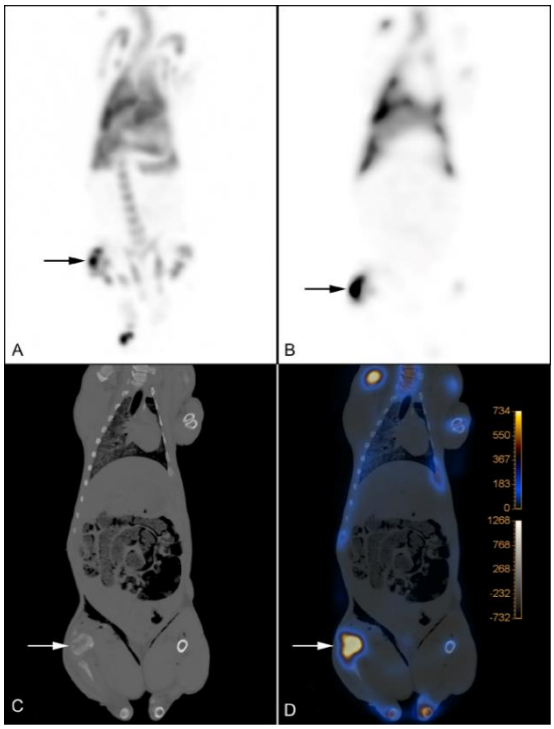

Figure 41. Postmortem [^{111}In]In-oxine-leukocyte SPECT; (A). [^{111}]In-oxine-leukocyte scintigraphy in ventral projection; (B). CT scan; (C) (bone window); and (D) fused images of a juvenile pig demonstrating increased leukocyte accumulation in an OM lesion in the proximal tibia (indicated by arrows) of the right hindlimb. In (A), leukocyte accumulation is also seen in the distal femur and the distal metatarsal bones III and IV (**Paper IV**).

[^{99m}Tc]Tc-HSA-Nanocolloid (red bone marrow)

The liver, spleen, and bone marrow took up [^{99m}Tc]Tc-HSA-nanocolloid nanoparticles, corresponding to normal physiological leukocyte uptake. We observed no uptake in OM.

DISCUSSION

OM often manifests as a chronic and disabling disease in humans, and high-performance diagnostics are imperative. The diagnosis of OM can be challenging. Molecular imaging can visualize infectious and inflammatory processes in their earlier stages; however, it is sensitive but not very specific. Therefore, we aimed to develop a novel PET tracer as sensitive as 2-[^{18}F]FDG but theoretically more specific for infection. We based the selection of tracers on their affinity for either OM or critical inflammatory mediators. We focused on radiotracers based on the ^{68}Ga radionuclide, which has some favorable characteristics, and compared the tracers to several more-or-less well-established ^{11}C- and ^{18}F-based tracers. We also included SPECT with [^{99m}Tc]Tc-IL-8 and traditional ^{111}In-labeled autologous leukocytes. We scanned 27 pigs using 16 radionuclide tracers with up to seven different tracers each. The animals developed 83 OM lesions in the right hindlimb and some soft tissue abscesses, making it possible to reach specific conclusions.

Using animals for scientific purposes is a long-lasting practice in medicine and a frequent matter of debate in societies. The remarkable anatomical and physiological similarities between humans and animals, particularly mammals, have driven the investigation of mechanisms and assessment of novel therapies in animal models before applying the findings to humans. However, not all results obtained on animals can be directly translated to humans. This observation is underlined by those who disprove any value of animal research. At the same time, the right to use animals to benefit human purposes, with the possibility that animals are harmed, is debated. These two aspects are often mixed into confusing arguments, which do not provide a clear picture of the matter.

Using an animal model of OM allows control of the precise timing and location of the OM and, to some extent, minimizes the confounding impact of colonization elsewhere. An animal model provides a unique opportunity to study some incompletely understood mechanisms involved in OM, such as the role of inflammation and the dynamics of bacterial colonization and infection. It also permits visualization of the molecular processes involved. Additionally, models allow testing of new radiotracers in a standardized and compatible way and make it possible to study the kinetics and dynamics of specific compounds, thereby providing essential information regarding the timing of scans.

Ideally, an animal model that is used to study human infectious disease should accurately reproduce the various aspects of the disease. A general approach to evaluating animal disease models (in our case, OM) is a study of their validity (Willner 1984). In the context of animal models of human physiology (here, the pathophysiology of OM), three forms of "validity" can be described (Willner 1984): "face validity" is defined as how well the animal model replicates the OM phenotype in humans; "predictive validity" shows how well the animal model predicts new aspects of human OM; and "construct validity" refers to how well the method used to induce OM reflects the pathogenesis of human OM. Others have reviewed various aspects of OM in animals (Johansen *et al*., 2013; Roux et al., 2021; Lüthje *et al*., 2020). Nevertheless, we focused mainly on the features of the disease that are essential for testing tracers.

Domestic pigs are more closely related to humans anatomically, genetically, and physiologically (Meurens *et al*., 2012) but not phylogenetically (Zhang *et al*., 2010) than are rodents. The porcine immune system resembles that of humans more closely than that of mice (78% and 73% of analyzed parameters, respectively ($p<0.0001$)) (Dawson *et al*., 2011), giving pig models high construct validity. The size of the pigs is also important in imaging and sampling blood. Therefore, pigs represent a more suitable animal model than rodents for studying various microbial infectious diseases. Experiments in pigs are more likely to help predict the effects of specific treatments in humans and in the imaging of molecular processes than are experiments in rodents. Using pigs as animal models has contributed to the acquisition of new knowledge that can be used to improve animal and human health (Alstrup *et al*., 2016, 2020a, **Papers VIII, X**).

Considering the decreasing effectiveness of antibiotics and the increasing number of methicillin-resistant *S. aureus* (MRSA) infections caused by inappropriate use of antibiotics and antiseptic agents, there is a need for discriminatory animal models that can be used to develop new therapeutic and diagnostic strategies. Pigs are a source of MRSA. *S. aureus* can be involved in various diseases, and models of *S. aureus* infection in pigs include wound infection (Svedman *et al*., 1989; Nielsen *et al*., 2021), OM (Jensen *et al*., 2010), pneumonia (Luna *et al*., 2009), and sepsis (Nielsen *et al*., 2009). In a porcine OM model that used 8-week-old pigs, lesions developed with a pattern and presentation similar to that of OM lesions in prepubertal children in whom there was a hematogenous spread of *S. aureus* (Jensen *et al*., 2010). In a pig, an age of 3-4 months is equivalent to an age of 6-7 years in a human (Tohyama *et al*., 2019).

In the original plan of this work, scanning acute and chronic OM pigs was an ambition. Acute OM was studied by scanning one week after inoculation, and chronic OM was studied by allowing two weeks to elapse between inoculation and scanning. An effect of a more aggressive infection than expected hindered the latter part of the study. In the one-week protocol, the developed OM lesions were subacute rather than acute. In the two-week protocol (chronic OM), it was necessary to euthanize most of the pigs before the protocol was completed based on reaching preset humane endpoints, and we ended that line of experiments. Only one pig was scanned 14 days after inoculation. However, as the pigs that were studied 6-8 days after inoculation (acute OM) all had subacute OM and even displayed signs of chronicity according to CT scanning and necropsy/histopathology, this was found not to disprove the results but instead to be an advantage (**Papers I-II;** Alstrup *et al*., 2016). As in the refinement study, most of the 20-kg pigs received penicillin; we were unable to establish whether the favorable results obtained in the 20-kg pig group were related solely to the younger age of the animals or whether penicillin treatment also modified the pattern of infection (Alstrup *et al*., 2016). However, the health status and success rate can be improved using 20-kg pigs treated with penicillin. After extensive *in vivo* scans and thus the long anesthesia of the pigs had been completed, their lungs and hearts, but not their brains, were affected (Alstrup *et al*., 2020b).

Monitoring standard parameters such as pulse, temperature, urine production, and oxygen saturation did not always allow us to identify the development and progression of subordinate organ pathology. However, CT imaging can be valuable as an adjunct to classic monitoring parameters (Alstrup *et al*., 2020a). Commercial pigs are generally suitable for use in proof-of-concept and model development work, as they are less expensive than minipigs. Nevertheless, minipigs are preferable for longer-term studies and are more appropriate for translational work. In a new study, we examined whether repeated noninvasive scans *per se* affect internal organs and postscan welfare in Göttingen minipigs (**Paper X**). The animals' postscan welfare results do not indicate that simple short-term scanning procedures significantly affect anesthetized and scanned Göttingen minipigs. We also learned that use of the more natural ventral recumbent position results in fewer complications (**Paper X**) and that blood sampling and transportation of the pigs should be minimized to prevent postscanning complications.

Johansen and Jensen reviewed the hematogenous spread of *S. aureus* OM in animal models (Johansen *et al*., 2013b). That group and others reported similarity to children, in whom OM most often involves the growth zones of the long bones of the lower extremities, perhaps due to more exposure of those bones to minor blunt trauma resulting from childhood activities, especially in boys, creating a locus of little necrosis (Johansen *et al*., 2013a, Dartnell *et al*., 2012). In our studies, *S. aureus* was also concentrated in the growth zones of the long bones of juvenile pigs (**Figure 18**, **Papers I**-**III** and **V**-**VII**), giving the pig model high face validity. This may be due to the characteristic blood supply to the long bones of juveniles (Resnick, 2002). Fifty percent of cases occur in children under five years of age, and the condition is twice as frequent in males as in females (Van Schuppen *et al*., 2012; Grammatico-Guillon *et al*., 2013). These facts and our results (**Paper V**) support the argument for limiting the use of CT to only scan the limbs in older children, a practice that would significantly reduce radiation exposure. While OM typically is solitary, multifocal bone involvement occurs in 7% of children and 22% of neonates (Jaramillo *et al*., 1995; Goergens *et al*., 2005). In neonates, there is a need for whole-body examination. It may be necessary to perform radionucleotide scans in children after administering some degree of anesthesia, and this could reinforce the idea of initiating the search for OM with the more rapidly performed CT.

According to Lew *et al*., 2004, acute OM evolves over a period of days or weeks, while chronic OM is somewhat arbitrarily defined as a long-standing infection that develops over months or even years and is characterized by the persistence of microorganisms, low-grade inflammation, and the presence of dead bone (sequestrum) and fistulous tracts. We demonstrated that 2-[^{18}F]FDG-

PET effectively detects OM lesions in the peripheral bones of juvenile pigs. We also observed sequesters and fistulas that had formed next to the growth zones as early as the first week after inoculation with *S. aureus*. The appearance of sequesters and fistulas indicates an unfavorable "chronic" stage of OM according to Cierny-Mader staging, which was developed for use in humans (Calhoun *et al*., 2009; Carek et al., 2001; Lazzarini *et al*., 2004). Thus, the differentiation between acute and chronic OM in humans and juvenile pigs may differ; there may be more aggressive pathogenesis in juvenile pigs, or the progression of the disease in children may be faster than has been assumed.

Injection of [^{15}O]water is an established method for quantitative *in vivo* blood perfusion measurement, but we were the first to use [^{15}O]water to study OM. We measured blood perfusion in acute/subacute lesions in infected pigs that were tested seven days after inoculation (Pig 1-15, **Table 3** (**Papers I-III**) Jødal *et al*., 2017a). We showed that acute/subacute bone lesions within cancellous bone compartments were generally accompanied by ~1.5-fold increased blood perfusion, as opposed to the ~sixfold increase in age-matched soft-tissue infections using [^{15}O]water-PET/CT scanning (Jødal *et al*., 2017a). Thus, bone tissue appears to behave differently than other tissues in many ways. The absence of lymph vessels in bone combined with the restrictive space within physically rigid bone tissue induces stasis and increased intraosseous pressure (Edwards *et al*., 2008). This low-grade increase may be related to the infection's necrotic character, the bone's low flow/perfusion reserve, and the bone's unique vasodynamic regulatory mechanisms. In a recent pharmacokinetic study conducted in pigs with five-day-old implant-associated *S. aureus* OM, the antibiotic cefuroxime penetrated incompletely into the implant cavity, and there was less complete penetration of infected cancellous bone than of infected subcutaneous tissue (Tøttrup *et al*., 2016). The authors speculated that differences in antibiotic penetration could result from impaired blood flow/perfusion. During acute OM, the formation of bone abscesses within the medullar cavity, metaphyseal space, or subperiosteal space may increase the pressure and lead to further bone necrosis. The advantages of using [^{15}O]water are that it involves a low radiation dose and that scans can be performed shortly after injection due to its short half-life (**Table 2**). The short half-life is also a disadvantage, as it requires the availability of a cyclotron and limits the time available for scanning.

The ideal imaging modality hardly exists, but such a perfect modality would be represented by a biomarker that can distinguish infection from inflammation with both high sensitivity and high specificity and is independent of the stage of disease, its anatomical location, and the tissue's blood supply; it would also be cost-effective, easy to manufacture, able to provide rapid imaging and accessible. Many diagnostic tools are available, but no single test has 100% diagnostic accuracy (Signore *et al*., 2017). CT detected all OMs (**Papers I-VII**). In our studies, it may have been easier to recognize even small OM lesions on CT scans than it would be in busy clinical work since the time available for interpretation of the pig CT scans was more or less unlimited, and we knew the pigs had OM. The results correspond to those reported by Gatidis *et al*., 2016 and Schmall *et al*., 2021 in PET/MRI studies. We only examined juvenile pigs that were healthy pigs prior to inoculation. The age of the pigs was comparable to that of prepubertal children. An advantage was that OM was limited to the right hindlimb. Children, in general, also suffer less frequently from degenerative disorders of joints and bones than adults do. In children, fewer competing illnesses lead to a less challenging analysis of glucose uptake by surrounding tissues, making interpretation of PET scans easier in juveniles.

More than four decades after its introduction, *in vitro* labeled leukocyte imaging still plays a dominant role in the molecular imaging of infection. Compared with the ideal radionuclide for molecular imaging infection, which should be safe, available, rapid to use, highly sensitive, and specific for the disease, labeled leukocytes have several weaknesses, as mentioned below. [^{111}In]In-

oxine-leukocytes detected 79% of OM (**Papers III-IV**). To date, no better radiotracer has been introduced. 2-[^{18}F]FDG has gained widespread use for imaging infections.

Although not specific, the 2-[^{18}F]FDG test is rapidly completed and provides high-resolution images. 2-[^{18}F]FDG is especially valuable for indications for which labeled leukocytes have a less prominent position, such as tuberculosis, spondylodiscitis, and fever of unknown origin. Nevertheless, 2-[^{18}F]FDG is a supplement, not a replacement, for labeled leukocytes (Palestro *et al*., 2020).

[^{111}In]In-oxine diffuses through the cell membrane and remains associated with the labeled cells. This is an advantage compared to many other tracers eluted from infectious cells. In pigs, this does not hinder imaging but results in better animal welfare since a shorter duration of anesthesia is needed. This makes transport easy, and simultaneous handling of several pigs is possible. These benefits were observed when we scanned pigs postmortem (**Paper IV**).

2-[^{18}F]FDG is currently the most frequently used tracer for clinical PET examinations in which tissue glucose uptake is visualized. 2-[^{18}F]FDG is very sensitive but is not specific. However, although it is considered routine in adults, PET/CT in children has been limited. The decision to utilize PET/CT in children should be individual, taking cumulative radiation exposure and the possible information to be gained from the scan into account. Given that many 2-[^{18}F]FDG-PET/CT, and especially CT, examinations are performed annually, reducing the amount of ionizing radiation without compromising the clinical information obtained is encouraged. The optimum amount of activity administered in any nuclear medicine or CT examination is a trade-off between radiation dose and the image's signal-to-noise ratio (SNR). The SNR defines obtainable clinical sensitivity. As we observed that 2-[^{18}F]FDG accumulated in all OMs (**Papers I-VII**), we performed a dose-reduction study (**Paper V**). The recommended maximum amount of injected activity of 2-[^{18}F]FDG for pediatric use is in the range of 3.7 to 5.2 MBq/kg (0.10-0.14 mCi/kg), with a minimum injected activity of 26 MBq (0.7 mCi) (Gelfand *et al*., 2011). In **Paper V**, we demonstrated that in OM diagnostics, it is possible to reduce the amount of radiotracer activity injected even more. The simulation study indicated that even small lesions are visible after injection of as little as 4.4 MBq of activity, corresponding to ~0.19 MBq/kg BW (0.005 mCi/kg), without compromising image quality in pigs (**Figures 27, 28**). Thus, we believe that the results we obtained using the pig model translate well to pediatric OM, supporting the application of CT and a reduced dosage of 2-[^{18}F]FDG in children to diagnose OM. Using this low amount of activity of 2-[^{18}F]FDG for PET/CT in children will result in lower radiation exposure than that incurred during a [^{99m}Tc]Tc-MDP/HDP bone scan: this further speaks for using PET/CT. Our purpose was not to examine the amount of exposure to ionizing radiation during CT. Nevertheless, much effort has been expended in developing new CT scanners and scanning protocols that markedly reduce the absorbed dose without compromising diagnostic performance and image quality (Leipsic *et al*., 2012; Liu, 2014; Klink *et al*., 2014; Gatewood *et al*., 2015; Padole *et al*., 2015; den Harder *et al*., 2015, 2016).

We observed no accumulation (SUV_{max}) of [^{99m}Tc]Tc-HDP/DDP, Na[^{18}F]F, or [^{99m}Tc]Tc-HSA-nanocolloid in OM lesions compared to similar locations in the noninfected left hindlimb. The absence of accumulation may indicate that osteoblast-induced reparative processes, including new bone formation, did not occur. OM lesions also did not accumulate [^{11}C]PK11195. That lack of accumulation suggests that immature porcine leukocytes may not express as much translocator protein (TSPO) as adult human leukocytes do or that a suboptimal scanning time was used (van der Laken *et al*., 2008; Gent *et al*., 2014). Recent analyses of pig blood samples for [5-^{11}C-methoxy]donepezil indicate that the tracer is metabolized more rapidly in juvenile pigs than in adult humans and that a significant metabolic product that contains the ^{11}C atom (and is thus visible on PET scans) has an affinity for the same benzodiazepine receptors as does donepezil, complicating the interpretation and understanding of the processes (Jødal *et al*., 2017b). [5-^{11}C-methoxy]donepezil did

not perform as well in OM (58%, **Table 5, Paper III**) as [^{18}F]FDG, probably because it is flow-dependent; the flow was, in general, not remarkably increased in the infected limb (Jødal *et al*., 2017b). It performed better in revealing soft tissue infections on static scans (lymph nodes, 75% (**Table 5**, **Paper III**) and abscesses, 100% (**Paper III**)) where blood flow was higher (~sixfold) than in noninfected tissue (Jødal *et al*., 2017b). But, too few dynamic data for soft tissue infection were available to reach a firm conclusion.

Compared to earlier studies of infection using ^{68}Ga (Mäkinen *et al*., 2005, Nanni *et al*., 2010, Kumar *et al*., 2011), the results we obtained for porcine OM were unexpected and disappointing, yielding a sensitivity of only 20% (**Table 5**, **Paper II**, Jødal *et al*., 2017b). Nanni *et al*. reported a sensitivity of 100% in humans. Less disappointing was the detection of enlarged lymph nodes (40%) (**Table 5**, **Paper II**) and contiguous abscesses (60%) (**Paper II**). The tracer is a Ga^{3+} ion with chemical similarities to the Fe^{3+} ion, making species differences unlikely. Our later dynamic studies indicated that the tracer could differentiate infected soft tissue from healthy tissue (despite its slow uptake rate) but was unsuitable for detecting bone infections (Jødal *et al*., 2017b). Nevertheless, too few data are available to allow us to draw conclusions. Mäkinen *et al.* found uptake in bone lesions in rats. But, they noted that a limitation of their study was that their model perhaps simulated OM arising from grossly contaminated long-bone fractures (Mäkinen *et al*., 2005). In contrast, our porcine OM model represents hematogenous OM that occurs without concomitant bone trauma. Later, we found that the scan time (120-133 min postinjection) was probably pushed to the limit (Vorster *et al*., 2014). In a study of lung lesions, Vorster *et al*. recommended that imaging be started no later than 120 min after injection of the tracer. Alternatively, our findings may be due to species or age differences (pigs/juveniles have slower absorption than humans/adults). Differences in the blood-background radioactivity of [^{68}Ga]Ga-citrate and the slight differences in the production of [^{68}Ga]Ga-citrate might also have contributed to the differences in the results (Jensen *et al*., 2015; Solomäki *et al*., 2017).

Neutrophilic granulocytes are the most common type of white blood cells (40-75%) in the blood of mammals. They are an essential part of the innate immune system. Neutrophilic granulocytes are phagocytic cells. Early in a bacterial infection, neutrophilic granulocytes respond to the condition and migrate through the blood vessels and the interstitial tissue to the site of infection, following chemical signals such as interleukin-8 (IL-8) in a process called chemotaxis. Neutrophilic granulocytes have high expression of two IL-8 receptors, CXCR1 and CXCR2 (Patel *et al*., 2001), and IL-8 binds to these receptors with high affinity (Holmes *et al*., 1991; Murphy *et al*., 1991; Lee *et al*., 1992).

[^{99m}Tc]Tc-IL-8 offers several advantages compared to radiolabeled leukocytes. The radionuclide ^{99m}Tc is preferable due to its ideal physical characteristics, which include a short half-life (6 hours), emission energy of 140 keV, which is perfect for scintigraphy, the low radiation burden it involves compared with the use of ^{111}In or ^{67}Ga, its cost-effectiveness, and its general availability through technetium generators. Preparation of [^{99m}Tc]Tc-IL-8 is relatively simple and rapid, requiring less than 45 min, and the product does not require further purification. In comparison, the preparation of labeled leukocytes is time-consuming; handling the living cells *ex vivo* must be done delicately to preserve their viability and migration capacity. There is also a potential for transmission of blood-borne infections to both patients and technicians. The radiation exposure to the technician is also higher.

Neutrophilic granulocyte-binding [^{99m}Tc]Tc-IL-8 loses its plasticity and is trapped in the lung microcapillaries (**Figure 22, 39**). Pulmonary release occurs gradually, and these cells migrate to the infectious tissue and extravasate at the site of infection. Because the release of the cells from the lungs was a gradual process, blood sample analysis showed a low percentage of radioactivity associated with the white blood cells. Analysis of the blood samples essentially reflected the unbound

[^{99m}Tc]Tc-IL-8. Quantitative image analysis revealed relatively slow pharmacokinetics of the cell-bound [^{99m}Tc]Tc-IL-8 fraction (Rennen *et al*., 2003). The infectious foci in the lungs were, however, distinguishable from foci that were present due to physiological activity (**Figure 39**, **Paper VI**), and [^{99m}Tc]Tc-IL-8 may be a fair tracer for infection/inflammation in the lungs of humans when plain radiography and CT cannot provide sufficient information, as IL-8 is the major neutrophil chemotactic factor in humans (Kunkel *et al*., 1991).

[^{99m}Tc]Tc-IL-8 performed well, detecting 70% of the OM lesions (**Table 5**, **Paper VI**), and its performance was even better (92%) when scanning was delayed. These values compare favorably to the 78-79% we and others previously observed for ^{111}In-labeled autologous leukocytes (Dartnell *et al*., 2012, **Paper III-IV**) and delaying scans almost to the 100% by 2-[^{18}F]FDG. Our tracer was based on IL-8 of human origin. We anticipate, therefore, that the results for humans will be better than those obtained for pigs. The quick and simple preparation, early and good image quality, and lower radiation burden achieved with its use suggest that [^{99m}Tc]Tc-IL-8 may be a suitable imaging alternative for scintigraphic evaluation of acute OM in children.

Abscess uptake of [^{99m}Tc]Tc-IL-8 in immunocompetent rabbits with intramuscular infection was strongly confirmed by *in vivo* and *ex vivo* assays (Rennen *et al*., 2003). In abscesses, at the site of inoculation, the [^{99m}Tc]Tc-IL-8 tracer performed well, but we observed no uptake in lymph nodes (**Table 5**). Early or acute OM is generally assumed to occur within seven days after inoculation/induction of the infection. Nevertheless, we observed the formation of both sequesters and fistulous tracts, indicating a more advanced stage of infection (Carek *et al*., 2001; Lazzarini *et al*., 2004; Calhoun *et al*., 2009). Histology also confirmed a subacute infection stage. IHC indicated the presence of IL-8-producing neutrophils and a higher degree of exudation in the periphery of OM lesions (**Figure 38**, **Paper VI**). Sequesters occupied the space in the centers of the OM lesions, preventing the accumulation of neutrophils. Additionally, IHC often favors the peripheral part of a tissue section; that part displays the brightest staining, possibly due to more favorable concentration gradients of antibodies along the periphery of the droplets applied to the tissue section. These results confirm that osteomyelitis remains challenging to diagnose based on systemic findings and add to an understanding that local investigation is necessary. The accumulation of [^{99m}Tc]Tc-IL-8 is a neutrophil-driven gradual process that is specific and efficient and can be performed within a short time. However, the performance of [^{99m}Tc]Tc-IL-8 was better when scanning was delayed: 40% sensitivity was achieved after ~2 hours, and ~92% sensitivity was achieved after ~4 hours; perhaps the tracer's performance would have been better if we had waited eight hours after injection (Rennen *et al.*, 2003). It is also possible that phagocytosed *S. aureus* reduced the production of CXCL8 by neutrophils concomitant with suppression of phosphorylation of nuclear factor-κB, accelerating cell death and, in this manner, favoring the survival of *S. aureus* and promoting disease (Zurek *et al*., 2015).

In Jødal *et al*., 2018, 2019, we analyzed the dynamics of [^{68}Ga]Ga-DOTA-Siglec-9. The uptake of [^{68}Ga]Ga-DOTA-Siglec-9 was reversible and could be modeled using a reversible two-tissue-compartment model (rev2TCM, 4k-model). We demonstrated that [^{68}Ga]Ga-DOTA-Siglec-9 is metabolized very quickly, and we observed no increase in [^{68}Ga]Ga-DOTA-Siglec-9 uptake in OM in either dynamic or static images (**Table 5**, **Paper VII;** Jødal *et al*., 2019) obtained one to three hours after injection of the tracer (**Table 4**). The tracer accumulated in the better-perfused soft tissue infections and, on some occasions, had disappeared on later static scans; we concluded that the tracer might have a role in early (after 30 min) imaging of soft tissue infections but is not suitable for imaging of OM (**Paper VII;** Jødal *et al*., 2019).

The development of radiotracers specific for bacteria in biofilms would be advantageous when searching for underlying focal infection, in discriminating infection from inflammation, and in helping direct therapy. In our work, the static imaging acquisition was

performed using the same setup after the dynamic scans had been completed for logistic and financial purposes. Therefore, we did not analyze the dynamic scans obtained using [^{68}Ga]Ga-DOTA-K-A9 and [^{68}Ga]Ga-DOTA-GSGK-A11 before performing the static scans. Preliminary retrospective dynamic results indicate that the tracer elements were not attached to OM (**Figures 31, 32**), and this is not likely simply because the static scans were performed later (**Table 4)**. Only the bladder shows a strong signal. The lack of [^{68}Ga]Ga-DOTA-K-A9 and [^{68}Ga]Ga-DOTA-GSGK-A11 labeling of OM lesions (**Table 5**, **Paper VII**) may indicate the presence of an early stage of infection in which the bacteria have not yet formed a biofilm, or the selection may have been incorrect. In retrospect, a possible explanation for these results could be that the phage-displayed selected peptides had an affinity for dead bacteria in the *S. aureus* biofilm rather than for living bacteria, as was intended. Also, it might have been better to choose a different phage display to select against dead bacteria (Nielsen *et al*., 2018). That would have ensured that the chosen peptides were selected for living rather than dead bacteria and would have increased the chance for the peptide to have a specific affinity for the *S. aureus* bacteria present within the lesions.

Our study showed no increase in [^{68}Ga]Ga-NOTA-ubiquicidin accumulation in the *S. aureus*-induced OM lesions (**Table 5**, **Paper VII**). It may be that a mouse or rabbit model inoculated with a human-derived *S. aureus* strain is not comparable to a pig model. Healthy pigs may eliminate bacterial infections quickly; thus, bacteria in the pigs may not be detectable using ^{68}Ga-labeled UBI_{29-41}. We have not thoroughly analyzed the dynamic scans obtained using [^{68}Ga]Ga-NOTA-ubiquicidin and, therefore, do not know the kinetics of this tracer in juvenile pigs. Thus, starting the static scans 60 min after tracer injection may be too late (**Table 4**). Another possibility is that heat, as Ebenhan mentioned, can quickly destroy peptides (Ebenhan *et al*., 2014), and the body temperature of pigs is slightly higher than that of humans.

L-[*S*-methyl-^{11}C]methionine performed at the same level as [^{111}In]In-oxine-labeled autologous leukocytes in detecting OM (~80%, **Table 5**, **Paper III**), and it performed even better in the detection of enlarged reactive lymph nodes (100%, **Table 5**, **Paper III**) and contiguous abscesses (100%, **Paper III**). Results were obtained using methionine, even though we now know from *Jødal et al*., 2017b that the optimal scan time after methionine injection is 15 min and not approximately 65 min used in our studies (**Papers I-III, IX**). In a more extensive study (**Paper IX**), L-[*S*-methyl-^{11}C]methionine was found to accumulate significantly only in the popliteal lymph nodes of the infected right hindlimb, whereas accumulation of 2-[^{18}F]FDG was also observed in the mammary and medial iliac lymph nodes. We found increased weight of the mammary and medial iliac lymph nodes and increased area fractions of Ki-67 and IL-8 in the mammary lymph nodes in response to *S. aureus* infection in pigs. For L-[*S*-methyl-^{11}C]methionine, we found no correlation between increased tracer signal and increased levels of Ki-67, L1, and IL-8 antigens (**Paper IX**). Future studies attempting to identify the inflammatory cells responsible for the accumulating PET tracers using the methods described here may benefit from increasing the group size and focusing on mammary lymph nodes in a porcine model with soft tissue lesions in the area in which mammary lymph node drainage occurs.

We have only recently become aware that stereochemistry plays an unexpected role in this context. Most amino acids exist in two chiral forms, L and D, but the amino acids that are found in animals and humans are homochiral and are of the L-form (Friedman, 1999). Accordingly, the synthesis of [*S*-methyl-^{11}C]methionine for PET scanning is generally based on L-methionine; in the above-cited PET studies on [*S*-methyl-^{11}C]methionine, we used L-methionine. However, a 2017 study demonstrated that bacteria such as *E. coli* and *S. aureus* display a high uptake of D-methionine, whereas the D-form has low uptake in animal and human tissue. For this reason, D-[*S*-methyl-^{11}C]methionine in a mouse model showed much more infection-specific uptake than did L-[*S*-methyl-^{11}C]methionine (Neumann *et al*., 2017). That group has since developed a novel synthesis method for D-[*S*-methyl-^{11}C]methionine, performed *in vitro* tests that demonstrate uptake of the tracer by a broad

range of clinically relevant bacteria, and is preparing for evaluation of the use of D-[*S*-methyl-^{11}C]methionine in human patients with, for example, vertebral spondylodiscitis (Stewart *et al*., 2020). In retrospect, the uptake of D-methionine (and other amino acids in the D-form) in bacteria perhaps is not so surprising, as Friedman mentions that D-amino acids are generally present in the bacterial cell walls that contribute to bacterial resistance to digestion by the body's (L-form) proteolytic enzymes (Friedman, 1999).

We originally planned to perform stereology but found that that procedure is more complex and labor-intensive than expected. The expense of evaluating a single OM lesion was 4,000 Euros; therefore, quantitating all OM lesions by stereology was unrealistic (**Figure 42**).

Figure 42. **Stereology is both Cumbersome and Expensive**

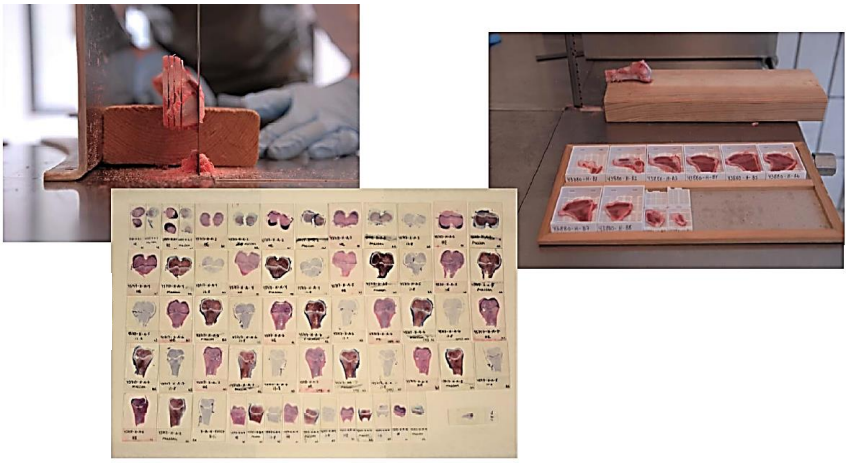

CONCLUSIONS

1. 2-[^{18}F]FDG and CT identified all 84 OM lesions.
2. An ~20-fold reduction in the 2-[^{18}F]FDG dose does not influence diagnostics; thus, low-dose scanning of children may be possible.
3. ^{111}In-labeled leukocytes performed well.
4. L-[*S*-methyl-^{11}C]methionine identified OM and soft tissue lesions.
5. No correlations exist between the accumulation of 2-[^{18}F]FDG and/or L-[*S*-methyl-^{11}C]methionine and proliferation and/or inflammation in lymph nodes.
6. [^{68}G]Ga-citrate did not perform well in our OM model.
7. [^{68}G]Ga-DOTA-Siglec-9 did not perform well in our OM model.
8. The accumulation characteristics of [^{68}Ga]Ga-DOTA-K-A9 and [^{68}Ga]Ga-DOTA-GSGK-A11 in pigs do not appear promising.
9. [^{99m}Tc]Tc-IL-8 performed as well as ^{111}In-labeled leukocytes and almost as well as 2-[^{18}F]FDG when the scan time was delayed, corresponding to the high density of IL-8 in OM lesions.
10. OM lesions have a lower perfusion reserve than do soft-tissue lesions.
11. We refined the OM model.

We refined a subacute porcine juvenile local *S. aureus* OM model by intra-arterial inoculation of the femoral artery with an isolate of porcine *S. aureus*. The inoculation had minimal systemic effects on the animal. We recommend streamlining the experimental protocols used in imaging studies in pigs to avoid affecting the physiology of the animals and inducing organ pathology. The model mimicked juvenile OM in humans very well, including occasional contiguous spread through the cortex to produce periosseous lesions; as in children, most of the lesions (~63%) developed in the femur, tibia, and fibula (Johansen *et al*., 2013; **Papers I-III, VII**).

Furthermore, we used PET, CT, and SPECT to compare and validate the techniques/tracers used to diagnose bone- and soft-tissue infections. These studies demonstrated that the pig model has high predictive validity, as the tracers routinely used in human clinics (e.g., 2-[^{18}F]FDG) gave similar results in pigs. Our studies demonstrated that among several tracers for SPECT (labeled leukocytes, IL-8, and bisphosphonates) and PET (^{18}F-, ^{68}Ga-, and ^{11}C-based tracers), 2-[^{18}F]FDG and CT were the most sensitive, and the results showed that [^{99m}Tc]Tc-IL-8 performed almost as well as 2-[^{18}F]FDG in detecting OM when the scanning was delayed (**Paper V** and data not shown). As radiation exposure must be minimal, we further showed that the radiation exposure received during a static 2-[^{18}F]FDG-PET/CT scan could be reduced to ~1/20 the currently used amount and still reveal small lesions with high sensitivity (**Paper V**).

The development of PET/CT and SPECT/CT tracers for the specific and sensitive diagnosis of inflammation and infection tested in a porcine OM model makes some of these tracers useful for human tests. We identified noninvasive procedures with low irradiation that are suitable for application in children. Thus, with this thesis, new goals have been reached in minimizing the radiation burden and maximizing the efficiency of noninvasive diagnostic methods using a juvenile pig model in ways that are directly clinically applicable to humans, especially in children.

LIMITATIONS

The scientific literature discusses several objections to the translation of animal models to human diseases, including problems with methodological quality and statistical analysis, publication bias, selection of model, congruence with humans, and reproducibility (**Paper VIII)**. We have attempted to circumvent some of these problems by using a well-characterized animal juvenile pig model known to mimic hematogenous OM in children. We would have liked to examine more pigs using fewer tracers and present chronic OM data. Optimally, we would have alternately inoculated the animals' right and left hind legs. We also wanted to characterize the labeled pig leukocytes. The use of anesthesia and penicillin may have also been a limitation. Quantifying the histopathological results would have strengthened the study by contributing to an understanding of the process's complexity and species differences. It would have thus helped validate the congruence of the model with OM in humans and its extrapolation to human diagnostics. Our findings exemplify the consideration that the kinetics and metabolism of tracers that undergo nonnegligible metabolism during the study should be examined before static scans are performed.

PERSPECTIVES

Lack of therapeutic success in individual patients affected with OM may have several interrelated causes. Thus, compromised blood perfusion in OM lesions causes impaired penetration of antibiotics, possibly necessitating supplementary surgical procedures and prolonged antibiotic

treatment lasting weeks or even months (Lew *et al*., 2004; Landersdorfer *et al*., 2009; Tøttrup *et al*., 2016; Jødal *et al*., 2017a). If not eradicated, bacteria cause chronic debilitating disease, and death can even result. Pharmacological and surgical therapy targeting the vascular bed facilitates the recruitment of inflammatory cells from the peripheral compartment, supports the occurrence of a regional lymph node response (surgical treatment), increases the intraosseous concentration of antibiotics, and accelerates healing.

No study has revealed the relationship between vascular insufficiency in OM and the effectiveness of systemic antibiotic therapy. Likewise, other than surgery, there is no unambiguous way to determine how many bacteria remained lodged in the infected tissue site after antibiotic treatment. We have not examined the distribution of antibiotics to OM lesions, but low perfusion could be one of several reasons that OM lesions are challenging to treat and slow to heal. Impaired perfusion reduces oxygen supply and results in a hypoxic microenvironment, aspects of OM that are also interesting to pursue. OM within the compact and rigid bone tissue may obstruct tissue perfusion by forming clots or necrotic tissue and high bone marrow pressure. There are no indications of lymphatic pathways in human bones, but we do not know whether this is the case in porcine bones. In a pilot study, we measured the interstitial pressure in the OM lesions and observed a tendency toward increased pressure before fistulous tracts were formed. Finding the association between the extent of vascular insufficiency and the effect of antimicrobial therapy in pig models of OM may lead to new research in humans to prove the concept in clinics and eventually foster new treatment protocols in which individual patients -and lesions- are chosen to receive either surgical treatment or tailored antibiotic therapy. Perfusion-directed personalized antibiotic treatment based on a porcine *S. aureus* OM model would benefit individual patients. Additionally, it would reduce the use of critically essential antibiotics and thus minimize antibiotic resistance, aligning with current national and international strategies to rationalize antibiotics ("Sundheds- & Ældreministeriet" 2017).

Pharmacological interventions (regulators of blood pressure and vascular tonus) and surgical interventions to induce increased lymphatic response may alter blood flow, peripheral blood pressure (capillaries and venules), hydrostatic interstitial fluid pressure, the flow of interstitial fluid, regional lymph node involvement, accumulation of antibiotics, the number of bacteria present, histopathology, OM size judged by CT, and the accumulation of 2-[^{18}F]FDG.

Personalized medicine has become increasingly important. There is an intention to dramatically reduce health care expenditures, along with improvements in the efficacy and safety of interventions tailored to the specific needs of individuals, through moving away from the earlier assumption of "one size fits all". Increasing treatment effectiveness for individuals and reducing the risks and expenditures associated with treating patients with an inappropriate drug are approaches to a new era of cheaper, more effective health care. In *S. aureus* infections, detailed information about an individual's biology and the microbial agent may be necessary. Both are necessary for successful identification and for choosing the most appropriate treatment. Medical imaging is one of the fastest-growing areas of medicine. It supplies biological information and information on physiology, organ function, biochemistry, metabolism, molecular biology, and functional genomics giving the practitioner the ability to map the disease biology of an individual patient. This information makes treatment that is tailored to the individual patient's disease biology and gene expression possible.

It will be interesting to perform FDG-PET/CT on children suspected to have OM, possibly preceded by a simulation study in adults with OM. We would also like to examine the use of [^{99m}Tc]Tc-IL-8, D- and L-[*S*-methyl-^{11}C]methionine in humans, especially children.

As stereochemistry appears to play an unexpected role (Neumann *et al*., 2017), it will be interesting to discover the potential of D-amino acids as infection tracers unfold in the coming years.

Increased life expectancy leads to increased numbers of joint prosthesis replacements, with several million prosthetic joints implanted yearly. Usually, replacements result in better joint function and pain relief, and the procedure is safe and cost-effective. However, prosthetic infection is a complication with an incidence ranging from 2.0 to 2.4% for primary interventions (Glaudemans *et al*., 2013) and increases to 20% for revision procedures (Cataldo *et al*., 2010). Like OM, prosthetic joint implant infection is a severe condition that may lead to repeated surgical intervention, prolonged hospitalization, and significant morbidity, and it is thus an economic burden. Prosthetic joint infections are classified by the time of onset after surgery as (1) early (within the first three months after surgery), (2) delayed (occurring between three months and two years after surgery), and (3) late (occurring more than two years after surgery) (Trampuz *et al*., 2005). Diagnosis of prosthetic implant infections in adults, like the diagnosis of OM, is challenging due to both possible displacements of the bone marrow and comorbidities such as arthritis/arthrosis. Microorganisms may reach the prosthesis at the time of implantation or later by hematogenous spread. It would be interesting to examine whether tracers such as [^{99m}Tc]Tc-IL-8 and L/D-[*S*-methyl-^{11}C]methionine are helpful in diagnosing those infections.

It will be interesting to follow the new artificial intelligence (AI) methods in CT and PET. AI can generate virtual attenuation-corrected PET/CT images which reduce patients' radiation exposure derived from CT. These methods can also improve image quality and quantitative accuracy of PET and SPECT imaging. In a time of lack of radiologists, it may relieve their work too.

REFERENCES

Aalbæk B, Jensen LK, Jensen HE, Olsen JE, Christensen H. Whole-Genome Sequence of *Staphylococcus aureus* S54F9 Isolated from a Chronic Disseminated Porcine Lung Abscess and Used in Human Infection Models. Genome Announc 2015; 3(5): e01207-15.

Aalto K, Autio A, Kiss EA, Elima K, Nymalm Y, Veres TZ, Marttila-Ichihara F, Elovaara H, Saanijoki T, Crocker PR, Maksimow M, Bligt E, Salminen TA, Salmi M, Roivainen A, Jalkanen S. Siglec-9 is a novel leukocyte ligand for vascular adhesion protein-1. It can be used in PET imaging of inflammation and cancer. Blood 2011; 118(13): 3725-3733.

Afzelius P, Nielsen OL, Alstrup AKO, Bender D, Leifsson PS, Jensen SB, Schønheyder HC. Biodistribution of the radionuclides ^{18}F-FDG, ^{11}C-methionine, ^{11}C-PK11195, and ^{68}Ga-citrate in domestic juvenile female pigs and morphological and molecular imaging of the tracers in hematogenously disseminated *Staphylococcus aureus* lesions. Am J Nucl Med Mol Imaging 2016; 6(1): 42-58. (a)

Afzelius P, Alstrup AKO, Schønheyder HC, Borghammer P, Jensen SB, Bender D, Nielsen OL. Utility of ^{11}C-methionine and ^{11}C-donepezil for imaging of Staphylococcus aureus induced osteomyelitis in a juvenile porcine model: comparison to autologous ^{111}In-labelled leukocytes, ^{99m}Tc-DPD, and ^{18}F-FDG. Am J Nucl Med Mol Imaging 2016; 6(6): 286-300. (b)

Afzelius P, Nielsen OL, Jensen SB, Alstrup AKO. Post Mortem Leukocyte Scintigraphy in Juvenile Pigs with Experimentally Induced Osteomyelitis. Contrast Media Mol Imaging 2017; 2017: 3603929: 1-6.

Afzelius P, Nielsen OL, Schønheyder HC, Alstrup AKO, Hansen SB. An untapped potential for imaging of peripheral osteomyelitis in paediatrics using [^{18}F]FDG PET/CT -the inference from a juvenile porcine model. EJNMMI Res 2019; 9(1): 29-37.

Afzelius P, Heegaard PMH, Jensen SB, Alstrup AKO, Schønheyder HC, Eek A, Boerman O, Nielsen OL. [^{99m}Tc]-labelled interleukin-8 as a diagnostic tool compared to [^{18}F]FDG and CT in an experimental porcine osteomyelitis model. Am J Nucl Med Mol Imaging 2020; 10(1): 32-46.

Afzelius P, Alstrup AKO, Nielsen OL, Nielsen KM, Jensen SB. Attempts to Target *Staphylococcus aureus* Induced Osteomyelitis Bone Lesions in a Juvenile Pig Model by Using Radiotracers. Molecules 2020; 25(18): 4329-43.

Afzelius P, Morsing MK, Nielsen OL, Alstrup AKO, Jensen SB, Jødal L. Lymph Nodes Draining Infections Investigated by PET and Immunohistochemistry in a Juvenile Porcine Model. Molecules 2022; 27: 2792-2806.

Ahtinen H, Kulkova J, Lindholm L, Eerola E, Hakanen AJ, Moritz N, Söderström M, Saanijoki T, Jalkanen, S, Roivainen A, Aro HT. ^{68}Ga-DOTA-Siglec-9 PET/CT imaging of peri-implant tissue responses and staphylococcal infections. EJNMMI Res 2014; 4: 45-55.

Akhtar MS, Qaisar A, Irfanullah J, Iqbal J, Khan B, Jehangir M, Nadeem MA, Khan MA, Afzal MS, ul-Haq I, Imran MB. Antimicrobial Peptide ^{99m}Tc-Ubiquicidin 29-41 as Human Infection-Imaging Agent: Clinical Trial. J Nucl Med 2005; 46: 567-573.

Alstrup AKO, Nielsen KM, Schønheyder HC, Jensen SB, **Afzelius P**, Leifsson PS, Nielsen OL. Refinement of a hematogenous localized osteomyelitis model in pigs. SJLAS 2016; 42(3): 1-4.

Alstrup AKO, Jensen SB, **Afzelius P**, Neto P, Pedersen M. Editorial. Use of Animal Models in Molecular Imaging. Contrast Media Mol Imaging 2020; 2020; 1-2. (a).

Alstrup AKO, **Afzelius PMT**, Jensen SB, Leifsson PS, Wegener KM, Nielsen OL. Effects of Long-term Anaesthesia, Blood Sampling, Transportation, and Infection Status on Hearts and Brains in Pigs Inoculated with *Staphylococcus aureus* Used for Imaging Studies. J Am Assoc Lab Anim Sci 2020; 59(1): 74-84. (b).

Alstrup AKO, Jensen SB, Nielsen OL, Jødal L, **Afzelius P**. Preclinical Testing of Radiopharmaceuticals for the Detection and Characterization of Osteomyelitis: Experiences from a Porcine Model. Molecules 2021; 26(14); 4221-33.

Alstrup AKO, Lillethorup TH, Landauer AM, **Afzelius P**. PET Imaging sessions do not cause detectable pathology in Göttingen minipigs. Scand J Lab Animal Sci. *Submitted.*

Arnold SR, Elias D, Buckingham SC, Thomas ED, Novais E, Arkader A, Howard C. Changing Patterns of Acute Hematogenous Osteomyelitis and Septic Arthritis: Emergence of Community-associated Methicillin-resistant *Staphylococcus aureus*. J Pediatr Orthop 2006; 26(6): 703-708.

Averill LW, Hernandez A, Gonzalez L, Peña AH, Jaramillo D. Diagnosis of Osteomyelitis in Children: Utility of Fat-Suppressed Contrast-Enhanced MRI. Am J Radiol 2009; 192(5): 1232-8.

Arvilommi A-M, Salmi M, Kalimo K, Jalkanen S. Lymphocyte binding to vascular endothelium in inflamed skin revisited: a central role for vascular adhesion protein-1 (VAP-1). Eur J Immunol 1996; 26(4): 825-33.

Banati RB, Newcombe J, Gunn RN, Cagnin A, Turkheimer F, Heppner F, Price G, Wegner F, Giovannoni G, Miller DH, Perkin GD, Smith T, Hewson AK, Bydder G, Kreutzberg GW, Jones T, Cuzner ML, Myers R. The peripheral benzodiazepine binding site in the brain in multiple sclerosis: Quantitative *in vivo* imaging of microglia as a measure of disease activity. Brain 2000; 123: 2321-37.

Balair DC, Carroll M, Carr EA, Fekety FR. ^{67}Ga-Citrate for Scanning Experimental Staphylococcal Abscesses. J Nucl Med 1973: 14(2); 99-102.

Beheshti M, Mottaghy FM, Payche F, Behrendt FFF, Van den Wyngaert T, Fogelman I, Strobel K, Celli M, Fanti S, Giammarile F, Krause B, Langsteger W. ^{18}F-NaF PET/CT: EANM procedure guidelines for bone imaging. Eur J Nucl Med Mol Imaging 2015; 42(11): 1767-77.

Bendre MS, Montague DC, Peery T, Akel NS, Gaddy D, and Suva LJ. Interleukin-8 stimulation of osteoclastogenesis and bone resorption is a mechanism for the increased osteolysis of metastatic bone disease. Bone 2003: 33(1): 28-37.

Bhusari P, Bhatt J, Sood A, Kaur R, Vatsa R, Rastogi A, Mukherjee A, Dash A, Mittal BR, Shukla J. Evaluating the potential of kit-based ^{68}Ga-ubiquicidin formulation of infection: A pilot study^{68}Ga. Nucl Med Commun 2019; 40(3): 228-34.

Bleeker-Rovers CP, Rennen HJJM, Boerman OC, Wymenga AC, Visser EP, Bakker JH, van der Meer JWM, Corstens FHM, Oyen WJG. ^{99m}Tc-Labeled Interleukin 8 for the Scintigraphic Detection of Infection and Inflammation: First Clinical Evaluation**.** J Nucl Med 2007; 48: 337-343.

Boutin R, Brossmann J, Sartoris DJ, Reilly D, Resnick D. Update on imaging of Orthopedic infections. Orthop Clin North Am. 1998; 29(1): 41-66.

Brouwer CPJM, Bogaards S, Wulferink M, Velders M. Synthetic peptides derived from human antimicrobial peptide ubiquicidin accumulate at sites of infections and eradicate (multi-drug resistant) Staphylococcus aureus in mice. J Nucl Peptides 2006; 27(11): 2585-91.

Burleson RL, Johnson MC, Head H. Scintigraphic Demonstration of Experimental Abscesses with Intravenous ^{67}Ga Citrate and ^{67}Ga Labeled Blood Leukocytes. Ann Surg 1973; 178(4): 446-51.

Cagnin A, Gerhard A, Banati RB. In vivo imaging of neuroinflammation. Eur Neuropsychopharm 2002; 12: 581-586.

Calhoun JH, Manring MM, Shirtliff M. Osteomyelitis of the long bones. Semin Plast Surg 2009; 23(2): 59-72.

Carek PJ, Dickerson LM, Sack JL. Diagnosis and management of osteomyelitis. Am Fam Physician 2001; 63(12): 2413-20.

Cataldo MA, Petrosillo N, Cipriani M, Cauda R, Tacconelli E. Prosthetic joint infection: recent developments in diagnosis and management. J Infect 2010; 61(6): 443-8.

Cerretti DP, Kozlosky CJ, Vanden Bos T, Nelson N, Gearing DP, Beckmann MP. Molecular characterization of receptors for human interleukin-8, GRO/melanoma growth-stimulatory activity and neutrophil activating peptide-2. Mol Immunol 1993; 30(4): 359-367.

Chitambar CR CR. Gallium and its competing roles with iron in biological systems. BBA Mol Cell Res 2016; 1863(8): 2044-53.

Conterno LO, Turchi MD. Antibiotics for treating chronic osteomyelitis in adults. Cochrane Database Syst Rev 2013 CD004439.

Costerton JW, Stewart PS, Greenberg EP. Bacterial biofilms: a common cause of persistent infections. Science 1999; 284(5418): 1318-22.

Dartnell J, Ramachandran M, Kartchburian M. Haematogeneous acute and subacute paediatric osteomyelitis: a systemic review of the literature. J Bone Joint Surg Br 2012; 94(5): 584-95.

Datz FL, Seabold JE, Brown ML, Forstrom LA, Greenspan BS, McAfee JG, Palestre CJ, Schauwecker DS, Royal HD. Procedure Guideline for Technetium-99m-HMPAO-Labeled Leukocyte for Suspected Infection/Inflammation. Society of Nuclear Medicine**.** J Nucl Med 1997; 38(6): 987-90

David R, Barron BJ, Madewell JE. Osteomyelitis, acute and chronic. Radiol Clin North Am 1987; 25(6): 1171-201.

Dawson, H. A Comparative Assessment of the Pig, Mouse, and Human Genomes: Structural and Functional Analysis of Genes Involved in Immunity and Inflammation. In The Minipig in Biomedical Research (Edited by *Peter A. McAnulty, Anthony D. Dayan, Niels-Christian Ganderup, Kenneth L. Hastings*), CRC Press, Taylor & Francis Group 2011; 321-341

De Schrijver M, Streule K, Senekowitsch R, Fridrichs R. Scintigraphy of inflammation with nanometer-sized colloidal tracers. Nucl Med Commun 1987; 8(11): 895-908.

Den Harder AM, Willemink MJ, De Ruiter QMB, Schilham AMR, Krestin GP, Leiner T, de Jong PA, Budde RPJ. Achievable dose reduction using iterative reconstruction for chest computed tomography: A systematic review. Eur J Radiol 2015; 84(11): 2307-13.

Den Harder AM, Willemink MJ, De Ruiter QMB, De Jong PA, Schilham AMR, Krestin GP, Leiner T, Budde RPJ. Dose reduction with iterative reconstruction for coronary CT angiography: a systematic review and meta-analysis. Br J Radiol 2016; 89(1058): 20150068-76.

Deysine M, Robinson R, Rafkin H, Teicher I, Silver L, Aufses AH. Clinical Infections Detected by ^{67}Ga Scanning. Ann Surg 1974: 897-901.

Drubach LA, Sapp MV, Laffin S, Kleinman PK. Fluorine-18 NaF PET imaging of child abuse. Pediatr Radiol 2008; 38(7): 776-9.

Ebenhan T, Chadwick N, Sathekge MM, Govender P, Govender T, Kruger HG, Marjanovic-Painter B, Zeevaart JR. Peptide synthesis, characterization and ^{68}Ga-radiolabeling of NOTA-conjugated ubiquicidin fragments for prospective infection imaging with PET/CT. Nuc Med Biol 2014; 41(5): 390-400. (a).

Ebenhan T, Zeevaart JR, Venter JD, Govender T, Kruger GH, Jarvis NV, Sathekge MM. Preclinical Evaluation of ^{68}Ga-Labeled 1,4,7-Triazacyclononane-1,4,7-Triacetic Acid-Ubiquicidin as a Radioligand for PET Infection Imaging. J Nucl Med 2014; 55(2): 308-14. (b).

Ebenhan T, Sathekge MM, Lengana T, Koole M, Gheysens O, Govender T, Zeevaart JR. ^{68}Ga-NOTA-Functionalized Ubiquicidin: Cytotoxicity, Biodistribution, Radiation Dosimetry, and First-in-Human PET/CT Imaging of Infections. J Nucl Med 2018; 59(2): 334-9.

Edwards JR, Williams K, Kindblom LG, Meis-Kindblom JM, Hogendoorn PCW, Hughes D, Forsyth RG, Jackson D, Athanasou NA. Lymphatics and bone. Hum Pathol 2008; 39(1): 49-55.

Espersen F, Frimodt-Moller N, Rosdahl VT, Skinhoj P, Bentzon MW. Changing pattern of bone and joint infections due to Staphylococcus aureus: study of cases of bacteremia in Denmark, 1959-1988. Rev Infect Dis 1991; 13(3): 347-58.

Ezzelarab MB, Ekser B, Isse K, Iwase H, Morelli AE, Ayares D, Cooper DKC. Increased soluble CD154 (CD40 ligand) levels in xenograft recipients correlate with the development of de novo anti-pig IgG antibodies. Transplantation 2014: 97(5); 502–8.

Ferro-Flores G, de Murphy CA, Pedraza-López M, Meléndez-Alafort L, Zhang Y-M, Rusckowski M, Hnatowich DJ. In vitro and in vivo assessment of ^{99m}Tc-UBI specificity for bacteria. Nucl Med Biol 2003: 306): 597-603.

Francis MD, Ferguson DL, Tofe AJ, Bevan JA, Michaels SE. Comparative evaluation of three disphosphonates: in vitro adsorption (C-14 labeled) and in vivo osteogenic uptake (Tc-99m complexed). J Nucl Med 1980; 21(12): 1185-9.

Friedman, M. Chemistry, Nutrition, and Microbiology of D-Amino Acids. J Agric Food Chem 1999; 47(9): 3457-79.

Fritz J, Tzaribachev N, Thomas C, Wehrmann M, Horger MS, Carrino JA, König CW, Pereira PL. Magnetic resonance imaging-guided osseous biopsy in children with chronic recurrent multifocal osteomyelitis. Cardiovasc Intervent Radiol 2012; 35(1): 146-53.

Frühling J, Verbist J, Balikdjian D. Which diphosphonate for routine bone scintigraphy (MDP, HDP or DPD)? Nucl Med Commun 1986; 7(6): 415-25.

Gallagher BM, Fowler JS, Gutterson NI, MacGregor RR, Wan CN, Wolf AP. Metabolic trapping as a principle of radiopharmaceutical design: some factors responsible for biodistribution of [^{18}F]2-deoxy-2-fluoro-d-glucose. J Nucl Med 1978; 19: 1154-61.

Garcia Del Pozo E, Collazos J, Carton JA, Camporro D, Asensi V. Factors predictive of relapse in adult bacterial osteomyelitis. BMC Infect Dis 2018; 18 635-45.

Gatewood MO, Grubish L, Busey JM, Shuman WP, Strote J. The use of model-based iterative reconstruction to decrease ED radiation exposure. Am J Emerg Med 2015; 33(4): 559-62.

Gatidis S, Schmidt H, la Fougère C, Nikolaou K, Schwenzer NF, Schäfer JF. Defining optimal tracer activities in pediatric oncologic whole-body ^{18}F-FDG-PET/MRI. Eur J Nucl Med Mol Imaging 2016; 43(13): 2283-9.

Gelfand MJ, Parisi MT, Treves ST. Pediatric radiopharmaceutical administered doses: 2010 North American consensus guidelines. J Nucl Med 2011; 52(2): 318-22.

Gelrud LG, Arseneau JC, Johnston GS. Gallium-67 Localization in Experimental and Clinical Abscesses (Abstr). Clin Res 1972; 20: 881.

Gent YYJ, Weijers K, Molthoff CFM, Windhorst AD, Huisman MC, Kassiou M, Jansen G, Lammertsma AA, van der Laken CJ. Promising potential of new generation translocator protein tracers providing

enhanced contrast of arthritis imaging by positron emission tomography in a rat model of arthritis. Arthritis Res Ther 2014; 16: R70-8.

Gjerløff T, Jakobsen S, Nahimi A, Munk OL, Bender D, Alstrup AKO, Vase KH, Hansen SB, Brooks DJ, Borghammer P. In Vivo Imaging of Human Acetylcholinesterase Density in Peripheral Organs Using ^{11}C-Donepezil: Dosimetry, Biodistribution, and Kinetic Analyses. J Nucl Med 2014; 55(11):1818-24.

Glaudemans AWJM, Galli F, Pacilio M, Signore A. Leukocyte and bacteria imaging in prosthetic joint infection. Eur Cell Mater 2013; 25: 61-77.

Goergens ED, McEnvoy A, Watson M, Barrett IR. Acute osteomyelitis and septic arthritis in children. J Paediatr Child Health 2005; 41(1): 59-62.

Gold RH, Hawkins RA, Katz RD. Bacterial osteomyelitis: findings on plain radiography, CT, MR, and scintigraphy. AJR Am J Roentgenol 1991; 157(2): 365-70.

Goodman RB, Forström JW, Osborn SG, Chi EY, Martin TR. Identification of two neutrophil chemotactic peptides produced by porcine alveolar macrophages. J Biol Chem 1991; 266(13): 8455-63.

Govaert GA, IJpma FF, McNally M, McNally E, Reininga IH, Glaudemans AW. Accuracy of diagnostic imaging modalities for peripheral post-traumatic osteomyelitis -a systemic review of the recent literature. Eur J Nucl Med Mol Imaging 2017; 44(8): 1393-1407.

Grammatico-Guillon L, Vermesse MZ, Baron S, Gettner S, Rusch E, Bernard L. Paediatric bone and joint infections are more common in boys and toddlers: a national epidemiology study. Acta Paediatr 2013; 102(3): e120-25.

Gratz S, Rennen HJ, Boerman OC, Oyen WJ, Burma P, Corstens FH. ^{99m}Tc-Interleukin-8 for imaging acute osteomyelitis. J Nucl Med 2001; 42(8): 1257-64.

Gross MD, Shapiro B, Fig LM, Steventon R, Skinner RWS, and Hay RV. Imaging of Human Infection with ^{131}I-Labeled Recombinant Human Interleukin-8. J Nucl Med 2001; 42(11): 1656-59.

Gutierrez K: Bone and joint infections in children. Pediatr Clin North Am 2005; 52: 779(3)-94.

Harada A, Sekido N, Akahosi T, Wada T, Mukaida N, Marsushima K. Essential involvement of interleukine-8 (IL-8) in acute inflammation. J Leukoc Biol 1994; 56(5): 559-64.

Harris SM, Davis JC, Snyder SE, Butch ER, Vävere AL, Kocak M, Shulkin BL. Evaluation of the Biodistribution of [^{11}C]Methionine in Children and Young Adults. J Nucl Med 2013; 54(11): 1902-8.

Hasman H, Moodley A, Guardabassi L, Stegger M, Skov RL and Aarestrup FM. *Spa* type distribution in *Staphylococcus aureus* originating from pigs, cattle and poultry. Vet Microbiol 2010; 141(3-4): 326-31.

Hirata K, Shiga T, Fujima N, Manabe O, Usui R, Kuge Y, Tamaki N. ^{11}c-Methionine Positron Emission Tomography May Monitor the Activity of Encephalitis. Acta Radiol 2012; 53: 1155-7.

Hirvonen J, Roivainen A, Virta J, Helin S, Någren K, Rinne JO. Human biodistribution and radiation dosimetry of ^{11}C-(R)-PK11195: the prototypic PET ligand to image inflammation. Eur J Nucl Med Mol Imaging 2010; 37: 606-12.

Hoffer P. Gallium: mechanisms. J Nucl Med 1980; 21(3): 282-5.

Hoiby N, Bjarnsholt T, Givskov M, Molin S, Ciofu O. Antibiotic resistance of bacterial biofilms. Int J Antimicrob Agents 2010; 35(4): 322-32.

Holmes WE, Lee J, Kuang WJ, Rice GC, Wood WI. Structure and functional expression of a human interleukin-8 receptor. Science 1991; 253(5025): 1278-80.

Ido T, Wan CN, Casella V, Fowler JS, Wolf AP, Reivich M, Kuhl DE. Labeled 2-deoxy-D-glucose analogs: ^{18}F-labeled 2-deoxy-2-fluoro-D-glucose, 2-deoxy-2-fluoro-D-mannose and ^{14}C-2-deoxy-2-fluoro-D-glucose". J Labeled Compounds Radiopharm. 178; 24(2): 174-183.

Ikpeme IA, Ngim NE, Ikpeme AA. Diagnosis and treatment of pyogenic bone infections. Afr Health Sci 2010; 10(1): 82-8.

Iliadis AD, Ramachandran M. Paediatric bone and joint infection. EFORT Open Rev 2017; 2(1): 7-12.

Jaakkola K, Knuuti J, Söderlund K, Saraste A, Jalkanen S, Voipio-Pulkki LM. Labelling lymphocytes with technetium^{99m}-hexamethyl propyleneamine oxime for scintigraphy: an improved labelling procedure. J Immunol Methods 1998; 214(1-2): 187-97.

Jaakkola K, Nikula T, Holopainen R, Vahasilta T, Matikainen MT, Laukkanen ML, Huupponen R, Halkola L, Nieminen L, Hiltunen J, Parviainen S, Clark MR, Knuuti J, Savunen T, Kääpä P, Voipio-Pulkki LM, Jalkanen S. In vivo detection of vascular adhesion protein-1 in experimental inflammation. Am J Pathol 2000; 157: 463-71.

Jagodzinski NA, Kanwar R, Graham K, Bache CE. Prospective evaluation of a shortened regimen of treatment for acute osteomyelitis and septic arthritis in children. J Pediatr Orthop 2009; 29: 518-25.

Jalkanen S, Salmi M. VAP-1 and CD73, Endothelial Cell Surface Enzymes in Leukocyte Extravasation. Arterioscler Thromb Vasc Biol 2008; 28(1): 18-26.

James ML, Gambhir SS. A molecular imaging primer: modalities, imaging agents, and applications. Physiol Rev 2012; 92(2): 897-965

Jaramillo D, Treves ST, Kasser JR, Harper M, Sundel R, Laor T. Osteomyelitis and septic arthritis in children: appropriate use of imaging to guide treatment. Am J Roentgenol 1995; 165(2): 399-403.

Jaramillo D. Infection: musculoskeletal. Pediatr Radiol 2011; 41 Suppl 1: S127-34.

Jensen HE, Nielsen OL, Agerholm JS, Iburg T, Johansen LK, Johansson E, Møller M, Jahn L, Munk L, Aalbæk B, Leifsson PS. A Non-traumatic *Staphylococcus aureus* Osteomyelitis Model in Pigs. In Vivo 2010; 24 (3): 257-264.

Jensen SB, Nielsen KM, Mewis Dennis, Kaufmann J. Fast and simple one-step preparation of ^{68}Ga citrate for routine clinical PET. Nuclear Med Commun 2013; 34(8); 806-12.

Johansen LK, Svalastoga EL, Frees D, Aalbæk B, Koch J, Iburg TM, Nielsen OL Leifsson PS, Jensen HE. A New Technique for Modeling of Hematogenous Osteomyelitis in Pigs: Inoculation into Femoral Artery J Investig Surg 2012; 26: 149-153.

Johansen LK, Koch J, Kirketerp-Møller K, Wamsler OJ, Nielsen OL, Leifsson PS, Frees D, Aalbæk B, Jensen HB. Therapy of haematogenous osteomyelitis-a comparative study in a porcine model and Angolan children. In Vivo 2013; 27: 305-12. (a).

Johansen LK, Jensen HE. Animal models of hematogenous *Staphylococcus aureus* osteomyelitis in long bones: a review. Orthop Res Rev 2013; 5: 51-64. (b).

Jones HW, Beckles VLL, Akinola B, Stevenson AJ, Harrison WJ. Chronic hematogenous osteomyelitis in children: an unsolved problem. Bone and Joint Surg Br 2011; 93(8): 1005-10.

Jødal L, Afzelius P, Jensen SB. Influence of Positron Emitters on Standard γ-Camera Imaging. J Nucl Med Technol 2014; 42(1): 42-50.

Jødal L, Hansen SB, Jensen SB. Impact of contamination with long-lived radionuclides on PET kinetics modelling in multitracer studies. Nucl Med Commun 2016; 37(8): 818-24.

Jødal L, Nielsen OL, **Afzelius P**, Alstrup AKO, Hansen SB. Blood perfusion in osteomyelitis studied with [^{15}O]water PET in a juvenile porcine model. EJNMMI Res 2017; 7(1); 4-14. (a)

Jødal L, Jensen SB, Nielsen OL, **Afzelius P**, Borghammer P, Alstrup AKO, Hansen SB. Kinetic Modelling of Infection Tracers [^{18}F]FDG, [^{68}Ga]Ga-Citrate, [^{11}C]Methionine, and [^{11}C]Donepezil in a Porcine Osteomyelitis Model. Contrast Media Mol Imaging. 2017; 1-18. (b).

Jødal L, Roivainen A, Oikonen V, Jalkanen S, Hansen SB, **Afzelius P**, Alstrup AKO, Nielsen OL, Jensen SB. Kinetic Modelling of [^{68}Ga]Ga-DOTA-Siglec-9 in a Porcine Infection Model. Physica Medica, 2018; 58, Suppl. 1: 124-125.

Jødal L, Roivainen A, Oikonen V, Jalkanen S, Hansen SB, **Afzelius P**, Alstrup AKO, Nielsen OL, Jensen SB. Kinetic modelling of [^{68}Ga]Ga-DOTA-Siglec-9 in Porcine Osteomyelitis and Soft Tissue Infections. Molecules 2019; 24(22): 4094-4114.

Jødal L, **Afzelius P**, Alstrup AKO, Jensen SB. Radiotracers for Bone Marrow Infection Imaging. Molecules 2021; 26; 3159-70.

Jørgensen NP, Alstrup AKO, Mortensen FV, Knudsen K, Jakobsen S, Madsen LB, Bender D, Breining P, Petersen MS, Schleimann MH, Dagnæs-Hansen F, Gormsen LC, Borghammer P. Cholinergic PET Imaging in Infections and Inflammation Using ^{11}C-Donepezil and ^{18}F-FEOBV. Eur J Nucl Med Mol Imaging 2017: 44(3); 449-58.

Kao H-C, Huang Y-C, Chiu C-H, Chang L-Y, Lee Z-L, Chung P-W, Kao F-C, Lin T-Y. Acute hematogenous osteomyelitis and septic arthritis in children. J Microbiol Immunol Infect 2003; 36(4): 260-5.

Kavanagh N, Ryan E, Widaa A. Staphylococcal osteomyelitis: disease progression, treatment, challenges and future directions. Clin Microbiol Rev 2018; 31(2): e00084-17

Kawashima K, Fujii T, Moriwaki Y, Misawa H. Critical roles of acetylcholine and the muscarinic and nicotinic acetylcholine receptors in the regulation of immune function. Life Sci 2012; 91(21-22): 1027-32.

Kim HO, Na SJ, Oh SJ, Jung BS, Lee S-H, Chang JS, Bin S-I, Ryu J-S. Usefulness of Adding SPECT/CT to ^{99m}Tc-Hexamethylpropylene Amine Oxime (HMPAO)-labeled Leukocyte Imaging for Diagnosing Prosthetic Joint Infections. J Comput Assist Tomogr 2014; 38(2): 313-9.

Klink T, Obmann V, Heverhagen J, Stork A, Adam G, Begemann P. Reducing CT radiation dose with iterative reconstruction algorithms: The influence of scan and reconstruction parameters on image quality and $CTDI_{vol}$. Eur J Radiol 2014; 83(9): 1645-54.

Kopesky P, Tiedemann K, Alkekhia D, Zechner C, Millard B, Schoeberl B, Komarova SV. Autocrine signaling is a key regulatory element during osteoclastogenesis. Biol Open 2014: 3: 767-76.

Koskinen K, Vainio PJ, Smith DJ, Pihlavisto M, Ylä-Herttuala S, Jalkanen S, Salmi M. Granulocyte transmigration through the endothelium is regulated by the oxidase activity of vascular adhesion protein-1 (VAP-1). Blood 2004; 103(9): 3388-95.

Kremers HM, Nwojo ME, Ransom JE, Wood-Wentz CM, Melton LJ, Huddleston PM. Trends in the epidemiology of osteomyelitis. J Bone Joint Surg 2015; 97: 837-45.

Kumar A, Muzik O, Chugani D, Chakraborty P, Chugani HT. PET-Derived Biodistribution and Dosimetry of the Benzodiazepine Receptorbinding Radioligand ^{11}C-(*R*)-PK11195 in children and adults. J Nucl Med 2010; 51: 139-44.

Kumar V, Boddeti DK, Evans SG, Roesch F, Howman-Giles R. Potential use of ^{68}Ga-*apo*-transferrin as a PET imaging agent for detecting *Staphylococcus aureus* infection. Nucl Med Bioly 2011; 38(3): 393-8.

Kumar V, Boddeti DK, Evans SG, Angelides S. ^{68}Ga-Citrate-PET for Diagnostic Imaging of Infection in Rats and for Intra-Abdominal Infection in a Patient. Curr Radiopharm 2012; 5(1): 71-5.

Kunkel SL, Standiford T, Kasahara K, Strieter RM. Interleukin-8 (IL-8): The Major Neutrophil Chemotactic Factor in the Lung. Exp Lung Res 1991; 17(1): 17-23.

Landersdorfer CB, Bulitta JB, Kinzig M, Holzgrabe U, Sörgel F. Penetration of Antibacterials into Bone: Pharmacokinetic, Pharmacodynamic and Bioanalytical Considerations. Clin Pharmacokinet 2009; 48: 89-124.

Laursen H, Jensen HE, Leifsson PS, Jensen LK, Christiansen JG, Trebbien R, Nielsen OL. Immunohistochemical detection of interleukin-8 in inflamed porcine tissues. Vet Immunol Immunopathol 2014; 159(1-2): 97-102.

Lauschke FH, Frey CT. Hematogenous osteomyelitis in infants and children in the northwestern region of Namibia. Management and two-year results. J Bone Joint surg Am 1994; 76(4): 502-10

Lazzarini L, Mader JT, Calhoun JH. Osteomyelitis in long bones. J Bone Joint Surg Am 2004; 86(10): 2305-18.

Lee J, Horuk R, Rice GC, Bennett GL, Camerato T, Wood WI. Characterization of Two High Affinity Human Interleukin-8 Receptors. J Biol Chem 1992; 267(23): 16283-7.

Leifsson PS, Iburg T, Jensen HE, Agerholm JS, Kjelgaard-Hansen M, Wiinberg B, Heegaard PM, Astrup LB, Olsson AE, Skov MG, Aalbaek B and Nielsen OL. Intravenous inoculation of *Staphylococcus aureus* in pigs induces severe sepsis as indicated by increased hypercoagulability and hepatic dysfunction. FEMS Microbiol Lett 2010; 309: 208-216.

Leipsic JL, Heilbron BG, Hague C. Iterative reconstruction for coronary CT angiography: finding its way. Int J Cardiovasc Imaging 2012; 28: 613-20.

Lew DP, Waldvogel FA. Osteomyelitis. N Engl J Med 1997; 336(14): 999-1007

Lew DP, Waldvogel FA. Osteomyelitis. Lancet 2004; 364(9431): 369-79.

Littenberg RL, Taketa RM, Alazraki NP, Halpern SE, Ashburn WL. Gallium-67 for Localization of Septic Lesions. Ann Intern Med 1973; 79(3): 403-6.

Liu L. Model-based Iterative Reconstruction: A Promising Algorithm for Today's Computed Tomography Imaging. J Med Imaging and Rad Sci 2014; 45(2): 131-6.

Love C, Marwin SE, Tomas MB, Krauss ES, Tronco GG, Bhargava KK, Nichols KJ, Palestro CJ. Diagnosing Infection in the Failed Joint Replacement: A Comparison of Coincidence Detection ^{18}F-FDG and ^{111}In-Labeled Leukocyte/^{99m}Tc-Sulfur Colloid Marrow Imaging. J Nucl Med 2004; 45(11): 1864-71.

Luna CM, Sibila O, Agusti C, Torres A. Animal models of ventilator-associated pneumonia. Eur Respir J 2009; 33: 182-8.

Luster AD. Chemokines-Chemotactic Cytokines That Mediate Inflammation. N Engl J Med 1998; 338: 436-45.

Lüthje FL, Jensen LK, Jensen HE, Skovgaard K. The inflammatory response to bone infection -A review based on animal models and human patients. APMIS 2020; 128: 275-286.

Mantero E, Carbone M, Calevo MG, Boero S. Diagnosis and treatment of pediatric chronic osteomyelitis in developing countries: prospective study of 96 patients treated in Kenya. Musculoskelet Surg 2011; 95(1): 13-8.

McCarthy JJ, Dormans JP, Kozin SH, Pizzutillo PD. Musculoskeletal infections in children. Basic treatment principles and recent advancements. J Bone Joint Surg 2005; 54: 515:28.

Madsen LW, Jensen HE. Necropsy of the Pig. In: Jensen HE, editor. *Necropsy A Handbook and Atlas.* Frederiksberg: Biofolia; 2011. pp. 83-106.

Mathews JD, Forsythe AV, Brady Z, Butler MW, Goergen SK, Byrnes GB, Giles GG, Wallace AB, Anderson PR, Guiver TA, McGale P, Cain TM, Dowty JG, Bickerstaffe AC, Darby SC. Cancer risk in 680,000 people exposed to computed tomography scans in childhood or adolescence: data linkage study of 11 million Australians. BMJ 2013; 346: 1-18.

Mattsson S, Johansson L, Svegborn LS, Liniecki J, Noßke D, Riklund KÅ, Stabin M, Taylor D, Bolch W, Carlsson S, Eckerman K, Giussani A, Söderberg L, Valind S. ICRP Publication 128. Radiation Dose to Patients from Radiopharmaceuticals: A Compendium of Current Information Related to Frequently Used Substances. Ann ICRP 2015; 44(2 Suppl): 7-321.

McAfee JG and Thaku ML. Survey of Radioactive Agents for in vitro Labelling of Phagocytic Leukocytes I. Soluble agents. J Nucl Med 1976: 17(6); 480-87. (a).

McAfee JG and Thaku ML. Survey of Radioactive Agents for in Vitro Labelling of Phagocytic Leukocytes II. Particles. J Nucl Med 1976: 17(6); 488-490. (b).

McILwain, Timpa JG, Kurundkar AR, Holt DW, Kelly DR, Hartman YE, Neel ML, Karnatak RK, Schelonka RL, Anantharamaiah GM, Killingsworth CR, Maheshwari A. Plasma Concentrations of Inflammatory Cytokines Rise Rapidly during ECMO-related SIRS due to the Release of Preformed Stores in the Intestine. Lab Invest 2010; 90(1): 128-39.

Mettler F, Guiberteau M. Chapter 8: Skeletal System. In: Mettler F, Guiberteau M, editors. Essentials of Nuclear Medicine Imaging, 6th ed. Philadelphia, PA: Saunders Elsevier, 2012: 296-300.

Meurens F, Summerfield A, Nauwynck H, Saif L, Gerdts V. The pig: a model for human infectious diseases. Trends Microbiol 2012; 20: 50-7

Murphy PM, Tiffany HL. Cloning of Complementary DNA Encoding a Functional Human Interleukin-8 Receptor. Science 1991; 253(5025): 1280-3.

Museru LM, Mcharo CN. Chronic osteomyelitis: a continuing orthopaedic challenge in developing countries. Internat Orthopaed 2001; 25: 127-31.

Mäkinen TJ, Lankinen P, Pöyhönen T, Jalava J, Aro HT, Roivainen A. Comparison of ^{18}F-FDG and ^{68}Ga PET imaging in the assessment of experimental osteomyelitis due to *Staphylococcus aureus*. Eur J Nucl Med Mol Imaging 2005; 32(11): 1259-68.

Nanni C, Errani C, Boriani L, Fantini L, Ambrosini V, Boschi S, Rubello D, Pettinato C, Mercuri M, Gasbarrini A, Fanti S. ^{68}Ga-Citrate PET/CT for Evaluating Patients with Infections of the Bone: Preliminary Results. J Nucl Med 2010; 51(12): 1932-6.

Neumann KD, Villanueva-Meyer JE, Mutch CA, Flavell RR, Blecha JE, Kwak T, Sriram R, VanBrocklin HF, Rosenberg OS, Ohliger MA, Wilson DM. Imaging Active Infection *in vivo* Using D-Amino Acid Derived PET Radiotracers. Sci Rep 2017: 7(1): 7903-10.

Nguyen JC, Markhardt BK, Merrow AC, Dwek JR. Imaging of Pediatric Growth Plate Disturbances. Radiographics 2017; 37(6): 1791-1812.

Nickerson EK, Hongsuwan M, Limmathurotsakul D, Wuthiekanun V, Shah KR, Srisomang P, Mahavanakul W, Wacharaprechasgul T, Fowler VG, West TE, Teerawatanasuk N, Becher H, White NJ, Chierakul W, Day NP, Peacock SJ. *Staphylococcus aureus* Bacteraemia in a Tropical Setting: Patient Outcome and Impact of Antibiotic Resistance. PLOS One 2009; 4: e4308-14.

Nielsen KM, Kyneb KH, Alstrup AKO, Jensen JJ, Bender D, **Afzelius P**, Nielsen OL, Jensen SB. ^{68}Ga-labelled phage-display selected peptides as tracers for positron emission tomography imaging of Staphylococcus aureus biofilm forming infections: Selection, radiolabelling and preliminary biological
evaluation. Nucl Med Biol 2016; 4: 593-605.

Nielsen KM, Jørgensen NP, Kyneb MH, Borghammer P, Meyer RL, Thomsen TR, Bender D, Jensen SB, Nielsen OL, Alstrup AKO. Preclinical evaluation of potential infection-imaging probe [^{68}Ga]Ga-DOTA-K-A9 in sterile and infectious inflammation. J Label Compd 2018; 61: 780-95.

Nielsen OL, Iburg T, Aalbaek B, Leifsson PS, Agerholm JS, Heegaard P, Boye M, Simon S, Jensen KB, Cristensen S, Melsen K, Bak AK, Backman ER, Jørgensen MH, Groegler DK, Jensen AL, Kjelgaard-Hansen M. Jensen HE. A pig model of acute *Staphylococcus aureus* induced pyemia. Acta Vet Scand 2009; 51(14): 1-8.

Nielsen OL, **Afzelius P**, Bender D, Schønheyder HC, Leifsson PS, Nielsen KM, Larsen JO, Jensen SB, Alstrup AK. Comparison of autologous ^{111}In-leukocytes, ^{18}F-FDG, ^{11}C-methionine, ^{11}C-PK11195 and ^{68}Ga-citrate for diagnostic nuclear imaging in a juvenile porcine haematogenous *Staphylococcus aureus* osteomyelitis model. Am J Nucl Med Mol Imaging. 2015; 5(2): 169-82.

Nielsen OL, Mellergaard M, Fres D, Larsen MN, Skov S, Olsen, LH, Reinmann MJ. A porcine model of subcutaneous *Staphylococcus aureus* infection: a pilot study. APMIS 2021: 130(7): 359-70.

Nijhof MW, Oyen WJG, van Kampen A, Classens RAMJ, van der Meer JWM, Costens FHM. Evaluation of Infections of Locomotor System with Indium-111-Labeled Human IgG Scintigraphy. J Nucl Med 1997: 38: 1300-5.

Niven E, Nahmias C. Absorbed dose to very low birthweight infants from ^{18}F-fluorodeoxyglucose. Health Phys 2003; 84(3): 307-16.

Okamura N, Funaki Y, Tashiro M, Kato M, Ishikawa Y, Maruyama M, Ishikawa H, Meguro K, Iwata R, Yanai K. *In vivo* visualization of donepezil binding in the brain of patients with Alzheimer's disease. Br J Clin Pharmacol 2008; 65(4): 472-9.

Onche II, Obiano SK. Chronic osteomyelitis of long bones: reasons for delay in presentation. Niger J Med. 2004;13(4): 355-8.

Pacák J, Točík Z, Černý M. Synthesis of 2-Deoxy-2-fluoro-D-glucose. J Chemical Soc D: Chemical Commun. 1969; 2: 77.

Padole A, Khawaja RDA, Kalra MK, Singh S. CT Radiation Dose and Iterative Reconstruction Techniques. AJR. 2015; 204(4): W384-92.

Palestro CJ, Brown ML, Forstrom LA, Greenspan BS, McAfee JG, Royal HD, Schauwecker DS, Seabold JE and Signore A. Society of Nuclear Medicine Procedure Guideline for Gallium Scintigraphy in Inflammation Version 3.0. Rome University La Sapienza 2004. pp. 1-5. (a).

Palestro, CJ, Brown ML, Forstrom LA, McAfee JG, Royal HD, Schauwecker DS, Seabold JE, Signore A. Society of Nuclear Medicine Procedure Guideline for ^{111}In-Leukocyte Scintigraphy for Suspected Infection/Inflammation, version 3.0 2004. pp 1-6. (b).
Palestro CJ. Molecular imaging of infection: the first 50 years. Semin Nucl Med 2020; 50: 23-34.

Patel L, Charlton SJ, JChambers JK, Macphee CH.Expression and functional analysis of chemokine receptors in human peripheral blood leukocyte populations. Cytokine. 2001; 14(1): 27-36.

Peltola H, Pääkkonen M. Acute osteomyelitis in children. N Engl J Med 014; 370: 352-60.

Peters AM, Osman S, Henderson Bl, Kelly JD, Danpure HD, Hawker RJ, Hodgson HJ, Neirinekx RD, Lavender JP. Clinical experience with 99mTc-hexamethylpropyleneamineoxime for labelling leukocytes and imaging inflammation. Lancet 1986; II: 946-9.

Piert M, Zittel TT, Machulla H-J, Becker GA, Jahn M, Maier G, Bares R, Becker HD. Blood Flow Measurements with [^{15}O]H_2O and [^{18}F]Fluoride Ion PET in Porcine Vertebrae. J Bone Miner Res 1998; 13(8): 1328-36.

Article I. Pineda C, Espinosa R, Pena A. Radiographic Imaging in Osteomyelitis: The Role of Plain Radiography, Computed Tomography, Ultrasonography, Magnetic Resonance Imaging,, and Scintigraphy. Semin Plast Surg 2009; 23(2): 80-9.

Potter M, Newport E, Morten KJ. The Warburg effect: 80 years on. Biochem Soc Trans 2016; 15: 44(5): 1499-505.

Pugliese F, Gaemperli O, Kinderlerer AR, Lamare F, Shalhoub J, Davies AH, Rimoldi OE, Mason JC, Camici PG. Imaging of Vascular Inflammation With [^{11}C]-PK11195 and Positron Emission Tomography/Computed Tomography Angiography. J Amer Coll Cardiol 2010; 56(8): 653-61.

Pääkkönen M, Kallio PE, Kallio MJT, Peltola H. Management of Osteoarticular Infections Caused by *Staphylococcus aureus* is Similar to That of Other Etiologies. Pediatr Infect Dis J 2012; 31(5): 436-8.

Ren W, Muzik O, Jackson N, Khoury B, Shi T, Flynn JC, Chakraborty P, Markel DC. Differentiation of septic and aseptic loosening by PET with both ^{11}C-PK11195 and ^{18}F-FDG in rat models. Nucl Med Commun 2012; 33(7): 747-56.

Rennen HJJM, van Eerd JE, Oyen WJG, Corstens FHM, Edwards DS, Boerman OC. Effects of Coligand Variation on the in Vivo Characteristics of Tc-99m-Labeled Interleukin-8 in Detection of Infection. Bioconjug Chem 2002; 13(2): 370-7. (a).

Rennen HJJM, Boerman OC, Oyen WJG, Corstens FHM. Labeling Method Largely Affects the Imaging Potential of Interleukin-8 [letter]. J Nucl Med 2002; 43: 1128. (b).

Rennen HJJM, Boerman OC, Oyen WJG, Corstens FHM. Kinetics of ^{99m}Tc-labeled Interleukin-8 in Experimental Inflammation and Infection. J Nucl Med 2003; 44(9): 1502-9.

Resnick D. Osteomyelitis, Septic Arthritis, and Soft Tissue Infection: Mechanisms and Situations. In: Resnick, D. (ed.). Diagnosis of Bone and Joint Disorders. 4th ed. W.B. Saunders Company. 2002; 2377-480.

Retamal J Sörensen J, Lubberink M, Suarez-Sipmann F, Borges JB, Feinstein R, Jalkanen S, Antoni G, Hedenstierna G, Roivainen A, Larsson A, Velikyan I. Feasibility of ^{68}Ga-labeled Siglec-9 peptide for the imaging of acute lung inflammation: a pilot study in a porcine model of acute respiratory distress syndrome. Am J Nucl Med Mol Imaging 2016; 6(1): 18-31.

Riise ØR, Kirkhus E, Handeland KS, Flatø B, Reiseter T, Cvancarova M, Nakstad B, Wathne K-O. Childhood osteomyelitis-incidence and differentiation from other acute onset musculoskeletal features in a population-based study. BMC Pediatr 2008; 8: 45-54.

Roddie ME, Peters AM, Danpure HJ, Osman S, Henderson BL, Lavender JP, Carroll MJ, Neirinckx RD, Kelly JD. Inflammation: imaging with Tc-99m-HMPAO-labeled leukocytes. Radiology 1988; 166: 767-72.

Roivainen A, Någren K, Hirvonen J, Oikonen V, Virsu P, Tolvanen T, Rinne JO. Whole-body distribution and metabolism of [N-methyl-^{11}C](R)-1-(2-chlorophenyl)-N-(1-methylpropyl)-3-isoquinoline carboxamide in man: an imaging agent for in vivo assessment of peripheral benzodiazepine receptor activity with positron emission tomography. Eur J Nucl Med Mol Imaging 2009; 36: 671-82.

Rosenbaum DM and Blumhagen JD. Acute epiphyseal osteomyelitis in children. Radiol 1985; 156(1): 89-92.

Rothe L, Collin-Osdoby P, Chen Y, Sunyer T, Chaudhary L, Tsay A, Goldring S, Avioli L, Osdoby P. Human osteoclasts and osteoclast-like cells synthesize and release high basal and inflammatory stimulated levels of the potent chemokine interleukin-8. Endocrinol 1998; 139(10): 4353-63.

Roux KM, Cobb LH, Seitz MA, Priddy LB. Innovations in osteomyelitis research: A review of animal models. Anim Models Exp Med 2021; 4: 59-70.

Rusckowski M, Gupta S, Liu G, Dou S, Hnatowich DJ. Investigations of a ^{99m}Tc-labeled Bacteriophage as a Potential Infection-Specific Imaging Agent. J Nucl Med 2004; 45(7): 1201-8.

Saavedra-Lozano J, Falup-Pecurariu O, Faust SN, Girschick H, Hartwig N, Kaplan S, Lorrot M, Mantadakis E, Peltola H, Rojo P, Zaoutis, LeMair, A. Bone and Joint Infections.The Pediatric Infectious Disease Journal 2017; 36(8): 788-799.

Sadik CD, Kim ND, Luster AD. Neutrophils cascading their way to inflammation. Trends Immunol 2011; 32(10): 452-60.

Salomäki SP, Kemppainen , Hohenthal U, Luoto P, Eskola O, Nuutila P, Seppänen M, Pirilä L, Oksi J, Roivainen A. Head-to-Head Comparison of ^{68} Ga-Citrate and ^{18} F-FDG PET/CT for Detection of Infectious Foci in Patients with *Staphylococcus aureus* Bacteraemia. Contrast Media Mol Imaging 2017;2017: 3179607-12.

Salvo N, Christakis M, Rubinstein J, de Sa E, Napolskikh J, Sinclair E, Ford M, Goh P, Chow E. The Role of Plain Radiographs in Management of Bone Metastases. J Palliat Med 2009: 12(2): 195-8.

Sarli G, Mandrioli L, Laurenti M, Sidoli L, Cerati C, Rolla G, Marcato PS. Immunohistochemical characterisation of the lymph node reaction in pig post-weaning multisystemic wasting syndrome (PMWS). Vet Immunol Immunopathol 2001; 83 (1-2): 53-67.

Saavedra-Lozano J, Falup-Pecurariu O, Faust SN, Girschick H, Hartwig N, Kaplan S, Lorrot M, Mantadakis E, Peltola H, Rojo P, Zaoutis T, LeMair A.Pediatr Infect Dis J 2017; 36(8): 788-99.

Scapini P, Lapinet-Vera JA, Gasperini S, Calzetti F, Bazzoni F, Cassatella MA. The neutrophil as a cellular source of chemokines. Immunol Rev 2000; 177(1): 195-203.

Schirrmeister H, Guhlmann A, Kotzerke J, Santjohanser C, Kühn T, Kreienberg R, Messer P, Nüssle K, Elsner K, Glatting G, Träger H, Neumaier B, Diederichs C, Reske SN. Early Detection and Accurate Description of Extent of Metastatic Bone Disease in Breast Cancer with Fluoride Ion and Positron Emission Tomography. J Clin Oncol 1999; 17(8): 2381-9.

Schmall JP, Surti S, Otero HJ, Serveas S, Karp JS, States LJ. Investigating Low-Dose Image Quality in Whole-Body Pediatric ^{18}F-FDG Scans Using Time-of-Flight PET/MRI. J Nucl Med 2021; 62(1):123-30.

Signore A, Beales P, Sensi M, Zuccarini O, Pozzilli P. Labelling of lymphocytes with Indium 111 oxine: effect on cell surface phenotype and antibody-dependent cellular cytotoxicity. Immunol Letters 1983;
6(3): 151-4.

Signore A and Glaudemans AWJM. The molecular imaging approach to image infections and inflammation by nuclear medicine techniques. Ann Nucl Med 2011; 25: 681-700.

Signore A, Glaudemans AWJM, Gheysens O, Lauri C, Catalano OA. Nuclear Medicine Imaging in Pediatric Infection or Chronic Inflammatory Diseases. Semin Nucl Med 2017; 47(3): 286-303.

Soerensen KE, Skovgaard K, Heegaard PMH, Jensen HE, Nielsen OL, Leifsson PS, Olsen HG, Aalbaek B, Kristensen AT, Kjelgaard-Hansen M, Wiinberg B, Iburg TM. The Impact of

Staphylococcus Aureus Concentration on the Development of Pulmonary Lesions and Cytokine Expression After Intravenous Inoculation of Pigs.Vet Pathol 2012; 49(6): 950-62.

Sokoloff L, Reivich M, Kennedy C, Des Rosiers MH, Patlak CS, Pettigrew KD, Sakurada O, Shinohara M. The [^{14}C]deoxyglycose method for measurement of local cerebral glucose utilization: theory, procedure, and normal values in conscious and anesthetized albino rats. J Neurochem 1977; 28(5): 897-916.

Salomäki SP, Kemppainen J, Hohenthal U, et al. Head-to-head comparison of ^{68}Ga-citrate and ^{18}F-FDG PET/CT for detection of infectious foci in patients with Staphylococcus aureus Bacteraemia. Contrast Media Mol Imaging. 2017; 2017: 3179607-14.

Stabin M, Siegel JA. RADAR Dose Estimate Report: A Compendium of Radiopharmaceutical Dose Estimates Based on OLINDA/EXM Version 2.0. J Nucl Med 2018; 59(1): 154-60.

Steer AC, Carapetis JR. Acute hematogenous osteomyelitis in children: recognition and management. Paediatr Drugs 2004; 6(6): 333-46.

Stewart MN, Parker MFL, Jivan S, Luu JM, Huynh TL, Schulte B, Seo Y, Blecha JE, Villanueva-Meyer JE, Flavell RR, VanBocklin HF, Ohliger MA, Rosenberg O, Wilson DM. A high enantiomeric excess in-loop synthesis of D-[methyl-^{11}C]Methionine for use as a diagnostic PET radiotracer in bacterial infection. ACS Infect Dis 2020; 6(1): 43-9.

Street M, Puna R, Huang M, Crawford H. Pediatric acute hematogenous osteomyelitis. J Pediatr Orthopae 2015; 35(6): 634-9.

Strieter RM, Kasahar K, Allen RM, Standiford TJ, Rolfe MW, Becker FS, Chensue SW, Kunkel SL. Cytokine-induced Neutrophil-derived Interleukin-8. Am J Pathol 1992: 141(2): 397-407.

Stöber B. Tanase U, Herz M, Seidl C, Schwaiger M, Senekowitsch-Schmidtke R. Differentiation of tumour and inflammation: characterisation of [methyl-^{3}H]methionine (MET) and O-(2-[^{18}F]fluoroethyl)-L-tyrosine (FET) uptake in human tumour and inflammatory cells. Eur J Nucl Med Mol Imaging 2006; 33(8): 932-9.

Summers WC. Bacteriophage therapy. Ann Rev Microbiol 2001: 51(1); 437-51.

Sundheds- og Ældreministeriet. National handlingsplan for antibiotika til mennesker. Tre målbare mål for en reduktion af antibiotikaforbruget frem mod 2020. (2017).

Svedman P, Ljungh A, Rausing A, Banck G, Sandén G, Miedzobrodzki J, Wadström T. Staphylococcal wound infection in the pig: Part I. Course. Ann Plast Surg 1989; 23(3): 212-8.

Tecchio C, Micheletti A, Cassatella MA. Neutrophil-derived cytokines: facts beyond expression. Front Immunol 2014; 5: 1-7.

Thakur ML, Lavender JP, Arnot RN, Silvester DJ, Segal AW. Indium-111-labelled Autologous Leukocytes in Man. J Nucl Med 1977; 18(10): 1014-21. (a).

Thakur ML, Segal AW, Louis L, Welch MJ, Hopkins J, Peters TJ. Indium-111-Labeled Cellular Blood Components: Mechanisms of Labeling and Intracellular Localization in Human Neutrophils. J Nucl Med 1977; 18(10): 1022-6. (b).

Thakur ML, McAfee JG. The Significance of Chromosomal Aberrations in Indium-111-Labelled Lymphocytes. J Nucl Med 1984; 25: 922-7.

Tohyama S, Kobayashi E. Age-Appropriateness of Porcine Models Used for Cell Transplantation. Cell Transplant. 2019; 28(2): 224-228.

Trampuz A, Zimmerli W. Prosthetic joint infections: update in diagnosis and treatment. Swiss Med Wkly 2005; 135(17-18): 243-51.

Trowell OA. The sensitivity of lymphocytes to ionising radiation. J Pathol and Bacteriol 1952: 64(4); 687-704.

Tsan M-F. Mechanism of Gallium-67 Accumulation in Inflammatory Lesions. J Nucl Med 1985; 26(1): 88-92.

Tuson CE, Hoffman EB, Mann MD. Isotope bone scanning for acute osteomyelitis and septic arthritis in children. J Bone Joint Surg 1994; 76(2)B: 306-10.

Turner MR, Cagnin A, Turkheimer FE, Miller CCJ, Shaw CE, Brooks DJ, Leigh PN and Banati RB. Evidence of widespread cerebral microglial activation in amyotrophic lateral sclerosis: an [^{11}C](*R*)-PK11195 positron emission tomography study. Neurobiol Dis 2004; 15(3): 601-9.

Tøttrup M, Bue M, Koch J, Jensen LK, Hanberg P, Aalbæk B, Fuursted K, Jensen HE, Søballe K. Effects of Implant-Associated Osteomyelitis on Cefuroxime Bone Pharmacokinetics. J Bone Joint Surg Am 2016; 98(5); 363-9.

Valentin J. Radiation dose to patients from radiopharmaceuticals: (Addendum 2 to ICRP Publication 53) ICRP Publication 80. 1998.

van den Wyngaert T, Strobel K, Kampen WU, Kuwert T, van der Bruggen W, Mohan HK, Gnanasegaran G, Delgado-Bolton R, Weber WA, Beheshti M, Langsteger W, Giammarile F, Mottaghy FM, Paycha F. On behalf of the EANM Bone & Joint Committee and the Oncology Committee. The EANM practice guidelines for bone scintigraphy. Eur J Nucl Med Mol Imaging 2016; 43, 1723-38.

van der Laken CJ, Elzinga EH, Kropholler MA, Molthoff CFM, Van der Heijden JW, Maruyama K, Boellaard R, Dijkmans BAC, Lammertsma AA, Voskuyl AE. Noninvasive Imaging of Macrophages in Rheumatoid Synovitis Using ^{11}C-(*R*)-PK11195 and Positron Emission Tomography. Arthritis Rheum 2008; 58(11): 3350-5.

van Malenstein H, Wauters J., Mesotten D, Langouche L, De Vos R, Wilmer A, van Pelt J. Molecular analysis of sepsis-induced changes in the liver: microarray study in a porcine model of acute fecal peritonitis with fluid resuscitation. Shock 2010; 34(4): 427-36.

van Schuppen J, van Doom MMAC, van Rijn RR: Childhood osteomyelitis: imaging characteristics. Insights Imaging 2012; 3(5): 519-33.

Vanquickenborne B, Maes A, Nuyts J, Van Acker F, Stuyck J, Mulier M, Verbruggen A, Mortelmans L. The value of ^{18}FDG-PET for the detection of infected hip prosthesis. Eur J Nucl Med Mol Imaging. 2003; 30(5): 705-15.

Virtanen H, Silvola JMU, Autio A, Li X-G, Liljenbäck H, Hellberg S, Siitonen R, Ståhle M, Käkelä M, Airaksinen AJ, Helariutta K, Tolvanen T, Veres TZ, Saraste A, Knuuti J, Jalkanen S, Roivainen A. Comparison of ^{68}Ga-DOTA-Siglec-9 and ^{18}F-Fluorodeoxyribose-Siglec-9: Inflammation Imaging and Radiation Dosimetry. Contrast Media Mol Imaging 2017; 2017: 7645070.

Vorster M, Maes A, Jacobs A, Malefahlo S, Pottel H, van de Wiele C, Sathekge, MM. Evaluating the possible role of 68Ga-citrate PET/CT in the characterization of indeterminate lung lesions," Annal Nuclear Med 2014; 28(6): 523-30.

Waldvogel FA, Medoff G, Swartz MN. Osteomyelitis: A Review of Clinical Features, Therapeutic Considerations and Unusual Aspects. N Engl J Med 1970; 282(4): 198-206

Wall BF. Radiation protection dosimetry for diagnostic radiology patients. Radiat Prot Dosimetry 2004; 109(4): 409-19.

Welling MM, Lupetti A, Balter HS, Lanzzeri S, Souto B, Rey AM, Savio EO, Paulusma-Annema A, Pauwels EKJ, Nibbering PH. ^{99m}Tc-Labeled Antimicrobial Peptides for Detection of Bacterial and *Candida albicans* Infections. J Nucl Med 2001; 42(5): 788-94.

Welling MM, Hensbergen AW, Bunshoten A, Velders AH, Rosenberg M, van Leeuwen FWB. An update on radiotracer development for molecular imaging of bacterial infections. Clin Transl Imaging 2019; 1-20.

Willner P. The validity of animal models of depression. Psychopharmacology 1984; 83: 1-16.

Yeo A, Ramachandran M. Acute haematogenous osteomyelitis in children. BMJ 2014; 348: g66.

Zeilhofer HU, Schorr W. Role of interleukin-8 in neutrophil signalling. Curr Opin Hematol 2000; 7(3): 178-82.

Zhang YE, Vibranovski MD, Landback P, Marais GAB, Long M. Chromosomal Redistribution of Male-Biased Genes in Mammalian Evolution with Two Bursts of Gene Gain on the X Chromosome. PLoS Biol 2010; 8(10); 1-13.

Zhao S, Kuge Y, Tsukamoto E, Mochizuki T, Kato T, Hikosaka K, Nakada K, Hosokawa M, Kohanawa M, Tamaki N. Fluorodeoxyglucose uptake and glucose transporter expression in experimental inflammatory lesions and malignant tumours: effects of insulin and glucose loading. Nucl Med Commun. 2002; 23(6): 545-50.

Zhao S, Kuge Y, Kohanawa M, Takahashi T, Zhao Y, Yi M, Kanegae K, Seki K-I, Tamaki N. Usefulness of ^{11}C-Methionine for Differentiating Tumors from Granulomas in Experimental Rat Models: A Comparison with ^{18}F-FDG and ^{18}F-FLT. J Nucl Med 2008; 49(1): 135-141.

Zurek OW, Pallister KB, Voyich JM. *Staphylococcus aureus* Inhibits Neutrophil-derived IL-8 to Promote Cell Death. J Infect Dis 2015; 212(6): 934-8.